UNIVERSITY of CALIFORNIA
Santa Barbara

Microstructure and Modeling of Granular Materials

A dissertation submitted in partial satisfaction
of the requirements for the degree of

Doctor of Philosophy

in

Physics

by

Gregg Lois

Committee in Charge:

Professor Jean M. Carlson, Chair
Professor Guenter Ahlers
Professor Jacob N. Israelachvili
Professor James S. Langer

September 2006

The dissertation of Gregg Lois is approved:

Professor Guenter Ahlers

Professor Jacob N. Israelachvili

Professor James S. Langer

Professor Jean M. Carlson, Committee Chairperson

June 2006

Microstructure and Modeling of Granular Materials

Gregg Lois

For Emilia:

Onward! to distant shores, there's so much life to experience together.

This is just the beginning of the beginning.

Acknowledgements

The completion of this thesis is only possible through an extraordinary confluence of events that has brought me together with a talented collection of scientists and a close group of friends. Lots of the credit should go to Jean Carlson, who has formed a stellar network of graduate students, postdocs and professors who think about a wide range of ideas and offer a perfect setting to grow as a scientist. Jean has always been quick with new ideas and inspirations, and is one of the most supportive advisors I've come in contact with. I also learned a great deal by working with Anael Lemaitre, who introduced me to granular materials, and the graduate students associated with Jean's group, who always kept me thinking.

Of course none of this would have worked out if not for the friends and family who kept me balanced. First and foremost I would like to thank my wife, who has the inimitable talent of making me happy and hopeful in pretty much any situation imaginable. I can't fathom having gone through the last five years in Santa Barbara without her. I'd also like to thank my family, who always support my curiosity and eccentricity. I was lucky enough to meet a wonderful group of friends during my time here, and to them: it was a great run, thank you for the fun, the memories, and good luck in the future!

Curriculum Vitæ

Gregg Lois

Education

2006	Ph.D. in physics, *magna cum laude*, University of California, Santa Barbara
2001	B. S. with honors in Math, B. S. with honors in Physics, *magna cum laude*, University of Puget Sound, Tacoma, Washington

Selected Publications

- "Long range correlation in granular shear flow", Gregg Lois, Anaël Lemaître and Jean M. Carlson, in preparation.
- "Momentum transport in granular flow", Gregg Lois, Anaël Lemaître and Jean M. Carlson, cond-mat/0602277.
- "The breakdown of kinetic theory in granular shear flows", Gregg Lois, Anaël Lemaître and Jean M. Carlson, cond-mat/0507286.
- "Numerical tests of constitutive laws for dense granular flows", Gregg Lois, Anaël Lemaître and Jean M. Carlson, Phys. Rev. E **72**, 051303 (2005); cond-mat/0501535.

Honors and Awards

2004	Mitsubishi Chemical Distinguished Graduate Award, Santa Barbara, California
2002	John Cardy Award, Physics Department, University of California, Santa Barbara
2001	Goman Award, Math Department, University of Puget Sound
2001	Seward Memorial Award, Physics Department, University of Puget Sound
2000	Murdoch Research Fellow, Physics Department, University of Puget Sound
1999	NSF REU Fellow, The Ohio State University
1998	NSF REU Fellow, Indiana University

Abstract

Microstructure and Modeling of Granular Materials

Gregg Lois

Granular materials are ubiquitous in natural and technological settings, but a predictive theory linking the microscopic grain-interactions with observed behavior remains elusive. Of particular interest are theories of constitutive relations, which challenge conventional models of statistical physics due to the athermal and amorphous nature of granular media. Here we explore properties of granular materials undergoing shear deformation, emphasizing how macroscopic properties arise from the microscopic interactions between grains. This is carried out using numerical simulations, which confirm that there is indeed a bulk rheology, independent of boundary conditions, that can be modeled using only the characteristics of the granular packing. In these simulations we measure spatial force correlations to demonstrate that long-range correlation exists and arises from clusters of simultaneously contacting grains in dense regimes. The size of the clusters defines an important microscopic length-scale ξ that diverges at the jamming transition, where the material first acquires a yield stress, and reveals the nature of grain-interactions. For small ξ grains interact solely through binary collisions whereas

for large ξ we observe that clusters of simultaneous contacts, along with complex force-chain networks, spontaneously emerge. This network transition occurs at a well-defined value of ξ and is accompanied by a dramatic transformation in the distribution of contact forces between grains that has been observed in previous simulations and experiments.

These basic results regarding the microscopic grain-interactions are generic to granular media and have important consequences for constitutive modeling. In particular we show that kinetic theories, which assume binary collisions, only apply below the network transition. In this regime we show that Enskog kinetic theory agrees with data from the simulations. We then proceed to introduce two analytical theories that use the observed microscopic grain-interactions to make predictions. First we propose a new constitutive model– the Force-Network model– that quantitatively predicts constitutive relations using properties of the force-networks for all values of ξ. Second we demonstrate that STZ theory, which predicts constitutive relations by assuming certain dynamical correlations in amorphous materials, is in agreement with both the microscopic motion of grains and measured constitutive relations for large ξ.

Preface

A great deal of progress has been made in statistical physics since Boltzmann first considered the properties of non-interacting gases over a century ago. Boltzmann's methods have been refined to include interactions between molecules in dense systems, and generic procedures have been developed to calculate the likelihood of microscopic configurations. These methods allow for a multitude of predictions that have been tested extensively and hold to a high degree of precision.

Equally impressive are more recent advances in understanding the nature of phase transitions. For a large class of materials that undergo a phase transition, *e.g.* when water changes from a liquid to a solid, a global symmetry is spontaneously formed and the amorphously arranged liquid phase is transformed into a solid phase with long-range order. A deep understanding of this process has been obtained using the renormalization group, where it is established that magnified copies of the material become interchangeable at the transition point. This approach predicts that many seemingly disparate phenomena have universal properties near their respective transition points, as has been observed.

Despite these extraordinary triumphs, many discoveries remain to be made. This can be appreciated by anyone who has ever walked along the beach on a

sunny day. When you take a step on the dry sand, there is the sensation that the grains of sand move slightly, and eventually come to rest. Because the grains ultimately support your weight, the sandpile is behaving like a solid, albeit without long-range order. But if you make a sudden run for the water, the sand under your feet gives way and begins to flow! This phenomenology– easily transforming between solid-like and liquid-like behaviors without any ordering of the constituent molecules– does not fit nicely into renormalization group theories of phase transitions.

Moreover, because the grains of sand on the beach are large (compared to typical molecules), their behavior is not affected by how hot it is outside. This invalidates the assumptions used to formulate Boltzmann-like theories of statistical physics, which rely heavily on certain properties provided by temperature. In the limit when temperature is turned off, the microscopic assumptions in these theories must be revisited and new conceptions of statistical physics must be formulated.

While the behavior of sand challenges current methods used to statistically describe physical systems, it is not a singular example. Sand is one element in a large class of systems called granular materials, which are very common and play an important role in our everyday lives. For example, think of the last time you were on the freeway and noticed, to your great dismay, that the density of cars

was increasing. Soon enough the traffic slowed and, as cars kept streaming in, you were stuck in a traffic jam. In this case the liquid-like phase of traffic flow was replaced by the solid-like phase of traffic jam, all without any sudden ordering in the positions of cars– only an increase in density. Also, because the motion of any individual car is controlled by an independent driver, the homogenizing concept of temperature does not apply. This results in a heterogeneous system that can be described, at a fundamental level, using theories established for granular media.

Granular materials are also important in many natural and technological settings. One example particularly relevant to life in Southern California is the behavior of earthquake faults. Earthquakes occur when faults are forced to move due to the steady continental drift. Although the forcing is steady, the motion of the faults is not. The faults are stationary for long times (when there are no earthquakes) and dynamic for short times (during an earthquake). This is a prime example of a granular system where external forcing causes a transition between solid-like behavior and liquid-like behavior. Upon careful examination of the fault surfaces, it is observed that they are rough and separated by a layer of ground rock. This has led to the hypothesis that a better understanding of granular media could aid in predicting, or even controlling, earthquakes.

In addition to earthquakes, the study of granular materials can be used to gain insight into other natural phenomena such as avalanches, the formation of galax-

ies, and asteroid impacts. Also, techniques and ideas from research on granular media have been applied to a variety of materials, such as glasses, foams, and emulsions. From a technological vantage point, a better understanding of how granular materials behave has a large impact in the pharmaceutical and chemical industries where the handling of granular materials is commonplace. In fact, it has been estimated that in the chemical industry, approximately one-half of the products and at least three-quarters of the raw materials are in granular form. Moreover, in 1994, the chemical industry in the United States alone invested over $61 billion to transport, process, and handle granular media.

Current research into the properties of granular materials can be roughly divided into three categories: the solid-like behavior, the liquid-like behavior, and the transition between the two. Investigations into the solid-like behavior began in 1773 when Coulomb used granular piles to formulate his famous friction law. Modern day research focuses on the heterogeneous nature of force transmission and its connection to macroscopic theories of elasticity. Unlike other solids that react to an external load by partitioning it homogeneously over all of the constituent molecules, with any molecule experiencing only Gaussian fluctuations about the mean, granular systems have heterogeneous force networks with grain forces distributed exponentially. This means that a significant number of grains experience forces much larger than the average. Microscopically, this is due

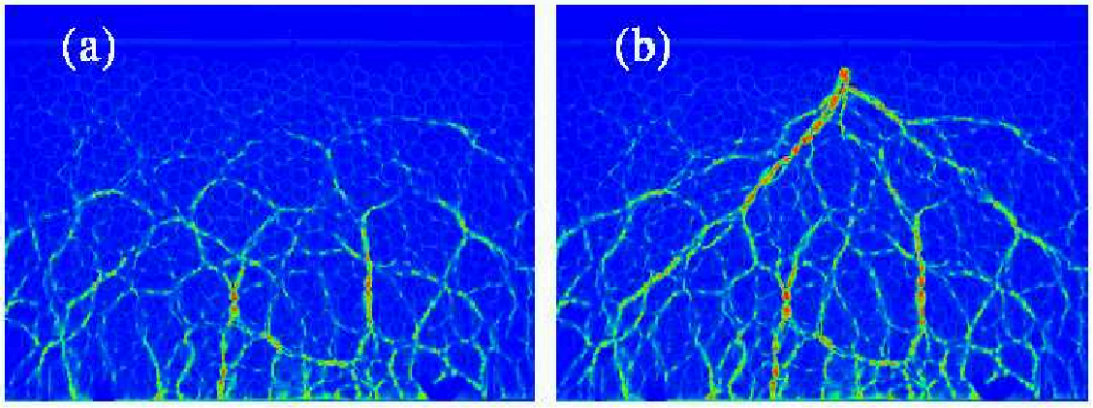

Figure I: Force chains in a static granular pile, from Ref. [39]. Photoelastic grains in the pile emit light depending on the magnitude of the force. Large forces create thick red lines, while smaller forces create thin green lines. The granular material, which is a collection of spheres, can also be seen in the pictures. (a) is a configuration under gravity and (b) is a configuration under gravity with a point force applied on the surface.

to force chains, which are linear excitations carrying larger than average forces. These force chains can be visualized using photoelastic grains, as was originally demonstrated by Dantu in 1957. A picture of the force chains in a static granular pile are shown in Figure I.

Investigations of the fluid-like properties of granular media were pioneered by Reynolds in 1885 with the observation that granular piles must first dilate in order to shear. More recent studies concentrate on either very dilute or very dense flows. In dilute regimes, researchers are interested in testing Boltzmann-like kinetic theory approaches. This is complicated by dissipation that occurs whenever grains interact. Because the dissipation occurs locally, grains that have

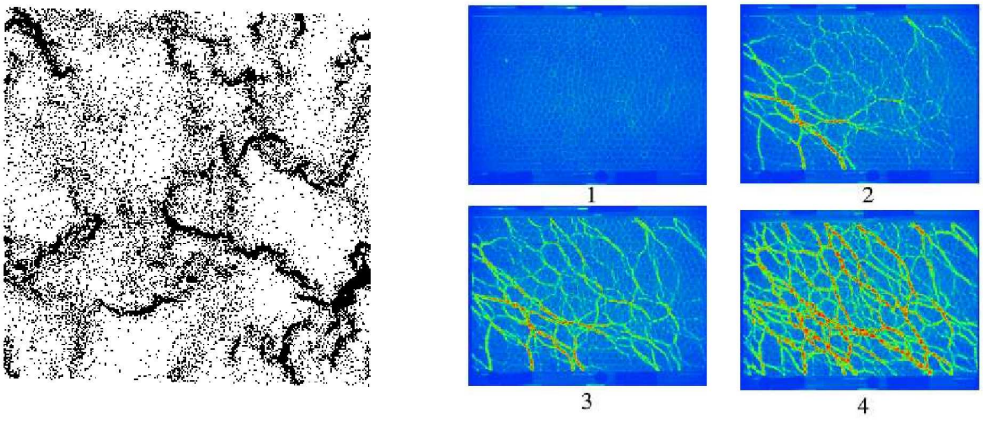

Figure II: Left: The clustering instability due to inelastic collapse in a dilute granular flow, from Ref. [66]. Each dot represents a particle, which tend to cluster. **Right:** Force chains in a dense granular flow, from Ref. [40]. The system is undergoing shear flow, with the top plane is forced to the right and the bottom plane held stationary. Force chains emerge and intensify as shearing proceeds from 1-4.

contacted have a higher probability to contact again. This leads to clustering and eventually inelastic collapse, where an infinite number of collisions occur in a finite amount of time. The presence of inelastic collapse has led many to suggest that conventional hydrodynamics might not be applicable to granular materials. In the dense flowing regime, force chains reemerge and there is a yield stress below which flow ceases. A great deal of research is focused on understanding how these properties affect the dynamics of the flow. Pictures of flowing granular materials, which illustrate the clustering due to inelastic collapse in dilute flows and the appearance of force chains in dense flows, are shown in Figure II.

Finally, there is much interest in understanding the transition between solid-like and liquid-like properties. Most of the research in this area is focused on regimes very close to the transition, and borrows ideas from critical phenomena. The "jamming" (or "rigidity") transition has been shown to be accompanied by power-law scalings and diverging length scales, as expected from a renormalization group analysis. However, the absence of an order parameter makes the transition novel. Theoretical investigations have focused on lattice models such as rigidity percolation, k-core percolation, and kinetically constrained models in attempts to explain the integral properties of the transition. These models fail to incorporate the amorphous structure of granular materials, but do mimic features of the actual transition.

In this thesis, the fluid-like properties of granular materials are investigated in detail. Our analysis focuses on bridging the gap between the very dilute and/or very dense systems that are generically studied. Some questions that we ask are: (1) Does a hydrodynamic description hold for multiple flowing geometries? (2) How and when does the emergence of force chains affect dynamics? (3) When is kinetic theory viable? (4) If kinetic theory breaks down, what other theories can we use to understand granular flows? (5) Can properties of flowing systems help us understand jamming?

Answers to these questions are pursued in this thesis, and the results bring us closer to a statistical description of granular materials.

Contents

List of Figures

Chapter 1

Introduction

Granular materials are collections of particles (grains) that only interact upon contact and are too large to be affected by external temperature. This is a simple system, devoid of long-range potentials or thermal fluctuations, that exhibits rich behaviors [1, 2, 3, 4, 5, 6, 7]. The prototypical granular material is sand, and initial interest in the field was primarily motivated by the need to predict the creep motion of soils and their stability properties for geophysical and engineering applications [8, 9, 10, 11, 12]. Recent research has focused on the more fundamental properties of granular media and how they are related to basic ideas of non-equilibrium statistical physics [13, 14, 15, 16].

Two important features exhibited by all granular media are that ordinary temperature is not relevant and interactions between grains dissipate energy. These features serve as a definition of "granular media" and are motivated by the example of sand. In this case the relevant energy scale associated with thermal

fluctuations is $k_B T$, which should be compared with the energy needed to raise a grain of sand one diameter in the Earth's gravitational field. For typical values of the parameters, the grain energy scale is of order 10^{12} times that of the temperature scale [3]. This means that, as a consequence of the size of the grains (of order 1μm or larger) it is always a good approximation to set $T = 0$. Also, because grains are large, each grain contains many atoms or molecules and energy will necessarily be lost due to heating or other effects in each interaction. Thus the *size* of typical grains, combined with the large number of grains, necessitates a statistical description in the limit of zero temperature. This statistical description is further complicated by the energy dissipation mechanism, which is dependent on interactions between grains and therefore heterogeneous.

The first difficulty that must be overcome to arrive at a statistical description is the lack of thermal fluctuations. A central property enforced by thermal fluctuations is that a statistical system will explore all of its possible configurations, of the same energy, with equal probability. This ergodicity forms the foundation of equilibrium statistical mechanics. For a granular material devoid of external perturbation, the "equilibrium" state is one at which each grain is at rest and there is no motion. This is obviously not an ergodic system and a particular grain packing will not necessarily have properties consistent with an ensemble of grain packings. Even in the case that external forcing is applied and the dynamics reach

a steady state where the dissipation at contacts is balanced by the energy injected by external forcing, it is not obvious that ergodicity holds and it may even be dependent on the type of forcing applied. These simple considerations call into question the fundamental building block of equilibrium statistical mechanics and suggest a re-evaluation of the non-equilibrium dynamical processes underlying the macroscopic state of the material.

When considering non-equilibrium processes in granular media, it is necessary to properly incorporate interactions between grains. These interactions arise at contacts between grains, and are due to the visco-elastic response of the grains to deformation [17]. The fundamental feature of grain interactions is that the interaction energy increases rapidly with increasing deformation, producing a repulsive, short-ranged, and non-conservative contact force. Nevertheless, the specifics of the interactions are generally quite complicated and depend on many factors. A central hypothesis is that much of the dynamical response can be understood through generic contact-force models that produce a purely repulsive force upon contact and provide a mechanism to dissipate energy [18]. The adjustable parameters are the dissipation per contact and the stiffness of the repulsion. The properties of granular shear flows have been studied extensively using these models and it is found that the packing fraction and the grain stiffness play very important roles [19].

If no external stress is applied to a granular material in the absence of gravity, it quickly loses all of its kinetic energy in dissipative collisions, and each grain comes to rest. If this occurs for a dilute system there will be no residual contacts between any grains and the total energy of the system will be zero. However, if the system is very dense, there will be contacts between grains in the relaxed state and a non-zero residual energy will remain due to grain deformation.

If an external stress is then applied to the relaxed system, motion will only occur if the shear stress is large enough to overcome the energy stored in the contacts. The minimum stress needed to initiate motion is called the yield stress, which is zero below a critical packing fraction ν_c and is an increasing function of packing fraction above ν_c [20, 21, 22].

For granular materials with $\nu > \nu_c$, previous research has demonstrated that the stiffness of the grains plays an important role at all values of the shear rate [19]. This is because grains can not rearrange to a configuration with no contacts and the system moves between different configurations with non-zero grain deformation. Shear flows with $\nu > \nu_c$ are characterized by slowly moving quasi-static flows [23, 24], where force balance is upheld at all times, and jamming [20, 21, 22], where there is no motion for stresses below the the yield stress.

Conversely, for granular media with $\nu < \nu_c$, it has been demonstrated that the stiffness of the grains can always be taken large enough so that it plays no role

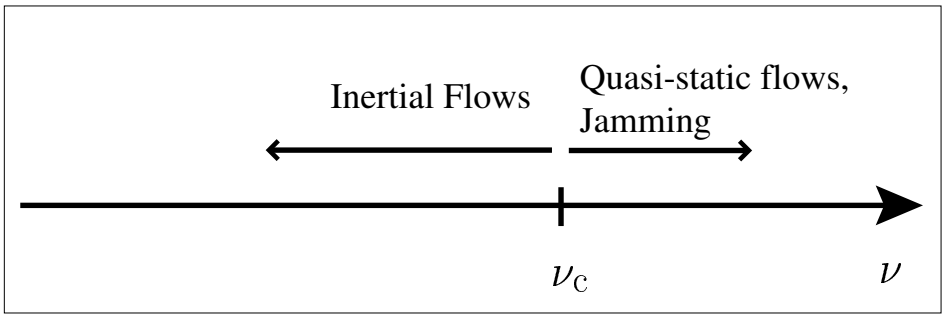

Figure 1.1: Schematic of the phase diagram of granular shear flow as a function of the packing fraction ν. For inertial flows with $\nu < \nu_c$ there is a well defined hard-sphere limit for infinitely stiff grains. For quasi-static flows with $\nu > \nu_c$ the stiffness always plays an important role. We will focus on inertial flows with $\nu < \nu_c$.

in the dynamics [19, 25, 26]. This is because grains can always rearrange to find free volume and the system moves between different configurations with very little grain deformation. In this regime inertial terms are dominant and an invariance in Newton's equations [27] demonstrates that the dynamics are controlled exclusively by the shear rate $\dot{\gamma}$.

This phenomenology, pictured in Figure 1.1, serves as a starting point for the ideas introduced here. A very intriguing aspect of the phase diagram is that, for $\nu < \nu_c$, there is a well-defined rheology in the limit of infinite stiffness. This is the limit where the grains are non-deformable and interact with a perfectly hard-core repulsion. In this regime the non-equilibrium properties should depend only on geometrical factors related to grain packing and the nature of energy dissipation. Therefore, the inertial regime of granular flow will have generic properties that

can be understood using simple simulations and theoretical arguments. This is the regime we focus on in this dissertation, which encompasses a wide range of flows with packing fractions from zero to ν_c.

Previous modeling in the inertial regime has focused on kinetic theory approaches, generalized to include the dissipative interactions between perfectly rigid grains [28, 29]. These approaches assume that the only relevant interactions are binary collisions between grains. However, many have suggested that this assumption should eventually break down as the density increases and long-lasting contacts arise [30, 31, 32, 33]. Indeed, in the quasi-static and jammed regimes it is observed that multi-grain contacts always occur [34, 35, 36] and contact forces are transmitted through "force chain networks" formed by the topology of the contact network [37, 18, 38, 39, 40, 41]. These force chains imply that multi-particle interactions are taking place and, although the forces between contacting grains still arise from grain deformation, the extent of the interactions is no longer localized and depends on the properties of the force chains.

The nature of grain-grain interactions is a central question that we investigate at length in this dissertation. In particular, we explore whether the microscopic picture of binary collisions holds for all $\nu < \nu_c$, or whether force chain networks begin to grow earlier. We find that force chains emerge spontaneously at a pack-

ing fraction $\nu_{\rm bc} < \nu_{\rm c}$ and this has important consequences that greatly affect macroscopic observables.

The organization of the thesis is as follows. We begin in Chapter 2 by formulating the basic equations of non-equilibrium transport, analogous to those from hydrodynamics. The new feature in granular materials is that the equation for the second moment of velocity has an additional term arising from energy dissipation. In Chapter 3 we proceed to derive simple properties of granular flows in the limit of perfectly rigid grains. These properties are a result of an invariance in Newton's equations and are related to the fact that interactions between perfectly rigid grains do not introduce an independent time-scale.

We then proceed in Chapter 4 to introduce the numerical algorithm used to simulate shear flows of perfectly rigid granular materials. This algorithm is used to simulate simple shear flow and incline flow and we present some basic results in each geometry. These results agree with previous simulations and experiments. The central finding is that the macroscopic rheology in each of these shear flows, far from the boundaries, is identical and only depends on grain properties.

In Chapter 5, we proceed to investigate the microscopic properties of the simulated shear flows. In particular we are interested in whether a theory based on binary collisions between grains is microscopically justifiable. To carry out this investigation we measure spatial force-force correlations between grains and find

long range correlation that decays exponentially. This defines a length-scale ξ, which is equal to the size of transient force chain networks that emerge as the density increases. We also show that contact forces are sensitive to the value of ξ. This demonstrates that theories based on binary collisions are not applicable beyond a certain packing fraction $\nu_{\rm bc}$. Associated with the network transition between binary collisions and force networks at $\nu_{\rm bc}$ is a signature in the contact force distribution function that has been observed previously in both simulations and experiments of granular flow. We end this chapter by presenting a phase diagram of inertial granular flow in Figure 5.10, which quantitatively determines when binary collisions occur and when transient networks emerge.

In Chapter 6 we explore the consequences of long range correlation on models of granular shear flow. We begin by showing that kinetic theory is only applicable for $\nu < \nu_{\rm bc}$. In this range of packing fraction we test the predictions of kinetic theory, without any fitting parameters, and find excellent agreement. Above $\nu_{\rm bc}$ new theories must be utilized to predict constitutive relations. We introduce a new theory, the force-network model, which is able to predict constitutive relations for the stress tensor. These prediction, which contain no adjustable fitting parameters, matches data from simulations over all values of $\nu < \nu_{\rm c}$. We end this chapter by testing the predictions of the Shear Transformation Zone (STZ) theory of amorphous solids. The STZ theory has found wide application in many

amorphous systems at low temperature and we find that both its microscopic assumptions and macroscopic predictions are upheld for $\nu > \nu_{\rm bc}$.

Finally, we end with a set of general conclusions and an outlook for the future of research into flows of granular media.

Chapter 2

Conservation Equations for Granular Media

A primary objective of non-equilibrium statistical mechanics is to provide molecular justifications for macroscopic equations. In granular media, the molecular or "microscopic" interactions between grains play a pivotal role, but there are fundamental relations that hold at the macroscopic level simply due to conservation relations for the mass, momentum, and energy. These do not require a detailed understanding of microscopic dynamics, although they do include unknown terms, such as the stress tensor, that must be determined from microscopic considerations. Here we review the conservation relations at the hydrodynamic level, where we are interested in the macroscopic evolution of densities of the extensive variables of mass, momentum and energy.

In granular media, mass and momentum are conserved, but energy is lost in each grain interaction. An equation of motion for energy can still be written and

involves a dissipative term. For conservation of mass and momentum, the classical forms hold [42]. Mass conservation reads:

$$\frac{\partial \rho}{\partial t} = -\frac{\partial}{\partial r_\alpha}\left(\rho V_\alpha\right), \tag{2.1}$$

where Greek superscripts represent components and repeated indices are summed. The mass density is denoted as $\rho(\mathbf{r}, t)$ and the fluid streaming velocity has components $V_\alpha(\mathbf{r}, t)$. These quantities are functions of the position $\mathbf{r}$ and time t. Similarly, conservation of momentum reads:

$$\frac{\partial}{\partial t}\left(\rho V_\alpha\right) = -\frac{\partial}{\partial r_\beta}\left[\rho V_\alpha V_\beta + \Sigma_{\alpha\beta}\right], \tag{2.2}$$

which defines the stress tensor $\Sigma_{\alpha\beta}(\mathbf{r}, t)$. If external forces exist, they must also be included on the right hand side of this equation.

Energy is not conserved in granular materials. Therefore, it is not possible to rely only on the conservation of energy to define a hydrodynamic equation. However, the equation for the energy can be written as a "conservative" part plus a dissipative part [43]. It takes the form:

$$\frac{\partial}{\partial t}\left(\rho\, e\right) = \frac{\partial}{\partial r_\alpha}\left[\rho\, e\, V_\alpha + J_\alpha + \Sigma_{\alpha\beta} V_\beta\right] + \zeta, \tag{2.3}$$

where e is the energy density, J_α denotes the heat flux, and ζ is the dissipative term. Oftentimes for granular materials, the energy density is written in terms of the "granular temperature" T, with $e = \rho T$. This relates T to the mean square of velocity in dilute regimes and we will adhere to this notation throughout. Equation (2.3) predicts a steady state in granular materials where the energy introduced from external perturbations exactly balances the energy lost through interactions between grains.

2.1 The Microscopic Connection

The conservations equations introduce unknown parameters, such as the stress tensor and the heat flux. Connecting these macroscopic fields to the microscopic motion of individual grains in a microcanonical formulation is non-trivial and has been the focus of recent studies [44, 45]. Ultimately, it is desirable to relate these fields to the density, the average velocity and the granular temperature. This is called constitutive modeling– if it is accomplished then Equations (2.1), (2.2), and (2.3) become a closed set that can be uniquely solved for any system under study. Here we will be interested in constitutive models of the stress tensor, and will focus on determining its value based on microscopic considerations.

In order to arrive at a microscopic equation for the stress tensor, it is necessary to derive the conservation equations from a microscopic point of view. A microcanonical form of conservation equations begins with the introduction of a coarse-graining function $\mathcal{G}$, which allows us to define a continuous density functional:

$$\rho(\mathbf{r}, t) = \sum_i m^i \mathcal{G}(\mathbf{r} - \mathbf{r^i}), \tag{2.4}$$

where m^i and $\mathbf{r^i}$ are the mass and position of grain i, and the sum is over all grains in the material. At the microscopic level, mass transport corresponds to the equation of motion for ρ. Taking a time derivative in Equation (2.4) and performing elementary algebra leads to

$$\frac{\partial \rho}{\partial t} = -\frac{\partial}{\partial r_\alpha} \sum_i m^i v_\alpha^i \mathcal{G}(\mathbf{r} - \mathbf{r^i}) \tag{2.5}$$

where v^i is the velocity of grain i. This equation, combined with Equation (2.1) defines the momentum density

$$\rho(\mathbf{r}, t) V_\alpha(\mathbf{r}, t) = \sum_{i=0}^{N} m^i v_\alpha^i \mathcal{G}(\mathbf{r} - \mathbf{r^i}). \tag{2.6}$$

In an analogous way, the hydrodynamic equation for momentum flux can be determined by taking the time derivative of the momentum density. The exact

microscopic expression for the stress tensor is then determined by rewriting the resulting expression in terms of a divergence. This process is strictly algebraic and does not require any assumptions regarding the inter-particle forces [44]. It yields:

$$\Sigma_{\alpha\beta}(\mathbf{r},t) = \sum_{i=0}^{N} \mathcal{G}(\mathbf{r}-\mathbf{r^i}) m^i (v_\alpha^i - V_\alpha)(v_\beta^i - V_\beta) + \frac{1}{2} \sum_{\{i,j\}=0}^{N_c} \sigma_\alpha^{ij} F_\beta^{ij} \int_0^1 \mathcal{G}(\mathbf{r}-\mathbf{r^i}+s\boldsymbol{\sigma}^{ij})\, ds, \tag{2.7}$$

where the sum is over all N_c contacts between grains, $\boldsymbol{\sigma}^{ij} = \mathbf{r}^i - \mathbf{r}^j$, and F_α^{ij} is the contact force between grains i and j.

Equation (2.7) is a formulation of the stress tensor from a microscopic point of view and it gives information on how the stress tensor is related to interactions between grains. The first term in Equation (2.7) represents how the velocity fluctuations of individual particles creates stress, and the second term gives the contribution from inter-grain forces. We will be most interested in the second term, which is often called the static contribution to the stress tensor and is denoted by

$$\Sigma_{\alpha\beta}^{\mathrm{s}}(\mathbf{r},t) = \frac{1}{2} \sum_{\{i,j\}=1}^{N_c} \sigma_\alpha^{ij} F_\beta^{ij} \int_0^1 \mathcal{G}(\mathbf{r} - \mathbf{r^i} + s\boldsymbol{\sigma}^{ij})\, ds. \tag{2.8}$$

The static stress is very sensitive to the value of inter-grain forces and is the dominant term of Equation (2.7) for dense granular flows where interactions between grains always occur [27]. In the remaining chapters we will explore theories that

predict the stress tensor in granular flows, using both numerical simulation and theoretical arguments. This requires a deeper understanding of the interactions between grains. To this end, we will focus on the properties of perfectly rigid grains, which we explore in the next chapter.

Chapter 3

Properties of Perfectly Rigid Grains

In the previous chapter we presented a derivation of the hydrodynamic equations from a microscopic point of view. The form of these equations is generic to granular media in the inertial regime, regardless of the external forcing or the interactions between grains. They do, however, contain unknown terms, such as the stress tensor, that depend on forces between interacting grains. In order to form a closed set of equations for the hydrodynamic variables of mass density, momentum density, and granular temperature, it is necessary to understand how forces arise between grains and how these forces can be determined from the hydrodynamic variables. In this chapter we discuss the relevant features of the grain-grain interaction for dry granular flows in the inertial regime. We present arguments that grain interactions are controlled exclusively by the hard-core repulsion. In this case, experimentally verified scaling properties of constitutive relations can

be derived using a fundamental invariance of Newton's equations. Therefore, the properties of perfectly rigid grains are of utmost importance for determining the dynamics of dry granular materials in the inertial regime.

When grains are dry–so that no water bridges induce attraction [46, 47]– and of size larger than the micrometer scale–so that no electrostatic interaction intervenes–their interaction is purely repulsive. It results from the elastic deformation of grains at contact and the dissipation of energy via friction and collisions. The complexity of this interaction motivates an important question: which properties of the grain-grain interaction contribute to any particular macroscopic observation? In some instances, details of the grain-grain interaction seem critical: for example, the Hertzian repulsion [48] is essential to understand the acoustic properties of granular materials in the quasi-static regime [49]. Numerical implementations of granular materials have thus relied on more or less elaborate models of the grain-grain interaction [18, 50, 51].

The arguments in a recent study by Campbell [19] assess the importance of the elastic (soft) part of the repulsive potential versus the limit where grains appear as perfectly hard and do not allow deformation. Campbell presented a detailed analysis of the different flow regimes obtained in a three dimensional simple shear simulation of granular flows while varying the stiffness k of the repulsion, the shear rate $\dot{\gamma}$, and the mass density ϕ. He found that the dimensionless parameter

$\Upsilon \equiv \frac{k}{\phi\sigma^3\dot{\gamma}^2}$, where σ is the grain diameter, dictates the character of the flow. This quantity is directly related to a Mach number which involves the ratio of the shear velocity $\sigma\,\dot{\gamma}$ over the sound speed c_s: $M = \sigma\,\dot{\gamma}/c_s = 1/\sqrt{\Upsilon}$. The hard grain limit corresponds to the regime where sound waves travel very fast compared to the rate at which contact networks are destroyed by the shear flow. This is the limit of very small Mach number, or small shear rates.

Campbell found that macroscopic properties do not depend on the Mach number for $M < 10^{-2}$. For these values of M, the stiffness of the grains is large enough so that it is effectively infinite. To compare this to a realistic granular material, we note that the sound speed is of order 100m/s. If we assume a grain size of order 1mm, the Mach number is expressible as $M = 10^{-5}\mathrm{s}\,\dot{\gamma}$. Therefore, in order to be in the limit where grains behave as if they are perfectly stiff, it suffices to restrict oneself to shear rates below $1000\mathrm{s}^{-1}$. Most experimental and natural situations occur at shear rates far below this limiting value and we can conclude that inertial flows of grains generally occur in the limit where the soft part of the repulsion is entirely masked by the steric exclusion. To study these flows it is sufficient to consider properties of perfectly hard grains. In the following sections we explore how the mathematical limit of perfectly hard grains gives insight into fundamental processes which are relevant to inertial flows.

3.1 Equations of motion under rigid grain conditions

The motion of N rigid grains in a D-dimensional granular material is determined by Newton's equations for the positions $\mathbf{r}^i$, angular orientations θ^i, momenta $\mathbf{p}^i$ and angular velocities ω^i:

$$\frac{d\mathbf{r}^i}{dt} = \frac{\mathbf{p}^i}{m^i}, \quad \frac{d\mathbf{p}^i}{dt} = \sum_j \mathbf{F}^{ij} + \mathbf{F}_{ext}, \tag{3.1}$$

$$\frac{d\theta^i}{dt} = \omega^i, \quad \frac{d\omega^i}{dt} = \frac{1}{I^i} \sum_j R^i \hat{\boldsymbol{\sigma}}^{ij} \times \mathbf{F}^{ij}, \tag{3.2}$$

where $\mathbf{F}_{ext}$ represents an external force such as gravity, $\mathbf{F}^{ij}$ represents a contact force on grain i by grain j, $\hat{\boldsymbol{\sigma}}^{ij}$ is the unit vector connecting the centers of grains i and j, R^i is the radius of grain i, and I^i is the moment of inertia.

These equations must be complemented with a prescription for the contact forces. In the hard grain limit these contact forces can be determined self-consistently by the conditions that (i) there is no penetration between grains–a force is instantaneously created upon contact to impede penetration and remains non-zero until the contact is broken–and (ii) by the friction law which couples to rotational degrees of freedom.

Important properties of granular materials arise directly from an invariance of the equations of motion (3.1, 3.2). We now spend some time studying these properties and assessing their consequences for macroscopic observations, in particular Bagnold's scaling.

3.2 Bagnold's Scaling

The success of kinetic theory came in a large part from its ability to account for the scaling between stress s and strain rate $\dot{\gamma}$ ($s \sim \dot{\gamma}^2$) first observed by Bagnold in dense granular materials [52]. Bagnold justified this behavior with a simple argument: the frequency of collisions and momentum change per collision are each proportional to the shear rate and therefore the stress is proportional to the square of the shear rate. Similar dimensional arguments are also a part of kinetic theory and are closely related to the concept of granular temperature (see [29] for a review). However, since these arguments are usually discussed in the framework of kinetic theory, it is unclear why Bagnold's scaling should hold in dense inertial systems where grains may not interact solely through binary collisions.

This has led to a great deal of interest in the origin and existence of Bagnold's scaling for *dense* granular flows. On the one hand, Bagnold's observations have been criticized: they may have arisen from a secondary instability of the granular

flow in his shear cell [53]. On the other hand, Bagnold's scaling has been directly observed by measuring shear stress and strain rate profiles in numerical simulations of granular flows down inclines [25, 54, 55], and is found to be consistent with experimental observations of the average flow rate in the same geometry [56]. The idea that dimensional invariance would hold for dense flows and enforce Bagnold's scaling has recently emerged [57, 58].

We wish to highlight the fact that, far from being reserved to "rapid" flows where kinetic theory applies, this dimensional invariance is a profound property of Newton's equations for hard sphere systems. It holds in both the dense and "rapid" flow regimes and does not require any of the assumptions of kinetic theory to hold. To clarify this issue, we find it useful to characterize the invariance in terms of phase space trajectories: this picture is well adapted to the case of dense flows where grains undergo multi-body interactions.

Important properties of granular shear flows in the rigid grain limit can be determined from a simple invariance in Newton's equations [27]. This invariance arises due to the absence of any fundamental time-scale in the interactions between perfectly rigid grains. Namely, for a granular material free from external forces with a constant shear rate, the time evolution will obey equations (3.1, 3.2) with $F_{ext} = 0$.

If we now rescale the contact forces by a scalar value $\mathbf{F}^{ij} \to \mathbf{F}^{ij}/A$ and simultaneously rescale the time $t \to t\sqrt{A}$, then Newton's equations are transformed to read:

$$\frac{d\mathbf{q}^i}{dt} = \frac{\mathbf{p}^i_{\text{new}}}{m^i}, \quad \frac{d\mathbf{p}^i_{\text{new}}}{dt} = \sum_j \mathbf{F}^{ij}, \tag{3.3}$$

$$\frac{d\theta^i}{dt} = \omega^i_{\text{new}}, \quad \frac{d\omega^i_{\text{new}}}{dt} = \frac{1}{I^i}\sum_j R^i \hat{\boldsymbol{\sigma}}^{ij} \times \mathbf{F}^{ij}, \tag{3.4}$$

where $\mathbf{p}^i_{\text{new}} = \mathbf{p}^i/\sqrt{A}$ and $\omega^i_{\text{new}} = \omega^i/\sqrt{A}$. This form for Newton's equations is identical to (3.1) and (3.2) with new values for the momenta and angular velocities.

After rescaling the contact forces and time we see that the positions and angular orientations remain unchanged, while the velocities are changed in accordance with the time rescaling. This implies that a movie of one granular flow where the grains have initial velocities $\{\mathbf{p}^i, \omega^i\}$ will look exactly the same as another movie where the initial velocities are doubled and the movie is played at half speed. The only difference in the dynamics is that the contact forces measured in the second movie would be four times larger than those in the first.

This invariance is a property of *perfectly hard grains* which must hold in the inertial regime, even infinitesimally close to jamming. In an experiment, this scaling breaks down only when it is no longer appropriate to model the experimental system by perfectly hard grains. Relying on the arguments of Campbell intro-

duced earlier [19], we can conclude that many experimental granular flows are in the regime where it is appropriate to model the system by hard grains.

Let us also note that this invariance is not limited to translationally invariant situations, like in the bulk of a granular flow or a biperiodic simulation cell. Indeed, suppose that we study the motion of perfectly hard-grains sheared between two confining walls taken themselves to be perfectly hard. Then again, a rescaling of force and time scales leave the phase-space trajectories invariant. In other words, changing the shear rate imposed via the walls leaves the velocity profile of the confined granular medium–including possible boundary layers–invariant after the appropriate rescaling. The forces in the whole system are rescaled accordingly.

The shear invariance in Newton's equations for perfectly hard grains immediately predicts a constitutive relation for the stress tensor. If, at any time, we multiply the velocity of all the grains in a shear flow by a factor A, then the shear rate $\dot{\gamma}$ will also increase by a factor A. In this case, based on the invariance in Newton's equations, the forces between grains will all be increased by a factor of A^2. This means that the forces between grains scale like $\dot{\gamma}^2$. Combining this with Equation (2.7) immediately predicts that any component of the stress tensor is proportional to $\dot{\gamma}^2$.

Additionally, because $\dot{\gamma}$ provides the only timescale in rigid granular shear flows, the granular temperature T should also scale with $\dot{\gamma}^2$. This implies that the

quantities $\Sigma_{\alpha\beta}\dot{\gamma}^{-2}$ and $T\dot{\gamma}^{-2}$ are independent of shear rate and, in steady state, should only depend on the packing fraction of the granular material.

3.3 What quasi-static limit?

For granular materials made of rigid grains, the invariance of Newton's equations predicts that Bagnold's scaling is the only possible constitutive relation. This is in stark contrast to other amorphous systems where a quasi-static regime is often observed and the stress tensor becomes independent of the shear rate.

In other amorphous systems such as low-temperature molecular glasses, dense suspensions, and foams, quasi-static behavior comes about because energy dissipation has a characteristic timescale. As the strain rate is lowered at constant density, the strain rate eventually becomes low compared to the dissipation rate and the flow reaches a state where kinetic energy becomes negligible compared to other forms of energy. In this case, the material flow properties become independent of strain rate and the dynamics enter the quasi-static regime.

The situation is quite different for granular materials, so long as they can be modeled as perfectly hard grains, because the invariance in Newton's equations always guarantees that the rate of energy dissipation will scale with the strain

rate. Therefore the terms entering Newton's equations always remain in the same ratio, which is a function of density only.

The quasi-static limit is thus pathological for perfectly hard grains: when the strain rate is scaled down, the system is always exploring the same trajectories in phase space, but at a slower speed. Nevertheless, as we pointed out earlier, quasi-static flow has been observed in granular media (see Figure 1.1). This implies that the grain stiffness must play an important role above a critical density, as has been verified in previous simulations [19].

The arguments presented above show that Bagnold's scaling is a direct consequence of interactions between perfectly rigid grains. Therefore the inertial regime of granular flow, where Bagnold's scaling is observed, can be studied by assuming that grains are perfectly rigid. In the next chapter we introduce a numerical algorithm that models granular flow of perfectly rigid grains and measure the dependence of the stress tensor and granular temperature on various material parameters.

Chapter 4

Numerical Simulations of Granular Shear Flow

In the previous chapter we investigated simple properties of perfectly rigid grains and showed how Bagnold's scaling is a direct result of the microscopic dynamics in these systems. Although Bagnold's scaling reveals the dynamical dependence of the stress tensor and granular temperature, these quantities are also sensitive to other properties of the granular material, such as the packing fraction. In this chapter we introduce an algorithm that we use to simulate flows of perfectly rigid grains and present many different macroscopic measurements of the rheological properties of granular flow.

We do indeed observe that Bagnold's scaling holds in all of the simulations that we perform. We also observe strong dependence on the density of the material, which is not explained by Bagnold's scaling. As a prelude to the introduction of theories to describe this dependence, we demonstrate in this chapter that the

macroscopic observables we measure are independent of shearing geometry and are fundamental properties of bulk granular flow.

In order to address these issues, we implement numerical simulations of granular materials in two different geometries:

- We implement simple shear flow in a cell with Lees-Edwards (LE) boundary conditions. In this configuration, the density and the shear rate is prescribed and the simulation cell is, by construction, translationally invariant. This grants direct access to averaged quantities of the granular temperature and stress tensor. Using this configuration we can characterize the steady state relation between stresses, granular temperature and shear-rate and extract numerically the parameters of a constitutive law for granular materials. A screenshot of this shearing geometry is shown in Figure 4.1.

- We implement granular flow down an inclined plane made of stationary grains. The simulation cell is periodic in the direction (x) parallel to the plane and the flow is inhomogeneous in the perpendicular (y) direction. In this configuration, the stresses are prescribed by the angle of the incline. We perform x-averaged, y-dependent measurements of granular temperature, velocity profiles, stress tensor, and shear-rate. Large heights of the granular layer grant access to the bulk rheology of the flow. This permits us to check

the existence of a well-define bulk rheology in the large height limit, and to compare it with the measurements in simple shear. A picture of this shearing geometry is shown in Figure 4.7.

In order to make a quantitative comparison in the two geometries, we use the same material throughout: a two-dimensional polydisperse collection of constant density grains with diameters chosen randomly from a flat distribution with minimum and maximum diameters given by $\sigma \pm \Delta$, where $\sigma = 1.4$ and $\Delta = 0.26\sigma$. The polydispersity restricts the material from crystallizing and imitates natural granular flows where a small amount of polydispersity is always present.

The main conclusion of this chapter is that there is a unique bulk rheology, far from boundaries, that can be modeled using only the properties of the granular packing (see Figure 4.10).

4.1 The Contact Dynamics Algorithm

To simulate granular flow, we use the Contact Dynamics algorithm [59, 60, 61, 62, 63, 64]. This is a completely athermal and dynamical algorithm, where the position and velocity of each grain is recorded and updated using Newton's equations.

The Contact Dynamics algorithm was devised to treat the dynamics of collections of perfectly rigid grains and can include the effects of friction between grains. The position and velocity of each grain is calculated by numerically integrating Newton's equations using a constant time step dt in a Verlet time stepping algorithm. In order to carry out this process, the Contact Dynamics algorithm provides a method for determining the forces between interacting grains at each time step. Whereas other simulation methods used for granular materials [63, 18] determine contact forces based on assumed physical properties of the grains, the Contact Dynamics algorithm determines the forces based on physical constraints in the rigid grain limit.

For dry granular materials, contact forces arise due to deformation of the grains upon contact and friction between grains. If we use $\hat{\boldsymbol{\sigma}}^{ij}$ to denote the unit vector connecting the centers of two contacting grains labeled i and j, then the deformation produces a normal force in the direction of $\hat{\boldsymbol{\sigma}}^{ij}$ and the interplay of friction and deformation produces a tangential for ce perpendicular to $\hat{\boldsymbol{\sigma}}^{ij}$. These contact forces are dissipative and depend sensitively on the velocities of the colliding grains [65]. In the case of perfectly rigid grains, these physical mechanisms can be simulated by simply providing constraints on the relative velocities of contacting grains.

The CD algorithm determines the forces arising from grain deformation by assuming that grains are infinitely rigid and setting constraints on the total energy dissipated in each contact. If two grains are in contact and have a relative velocity denoted by $\mathbf{v}'^{ij}$, then the algorithm determines a contact force such that the relative velocity in the next time step $\mathbf{v}^{ij}$ is given by

$$\mathbf{v}^{ij} \cdot \hat{\boldsymbol{\sigma}}^{ij} = -e\mathbf{v}'^{ij} \cdot \hat{\boldsymbol{\sigma}}^{ij} \quad ; \quad \mathbf{v}^{ij} \times \hat{\boldsymbol{\sigma}}^{ij} = e_t \mathbf{v}'^{ij} \times \hat{\boldsymbol{\sigma}}^{ij}. \tag{4.1}$$

In this way, the relative velocities are altered by restitution coefficients in the normal direction (e) and tangential direction (e_t). Friction is included by allowing the grains to have a coefficient of friction μ. If the ratio of the tangential to the normal force exceeds μ, then the grains are allowed to slip with a tangential force equal to μ times the normal force. Using these dynamical constraints arising from energy dissipation and friction, contact forces can be determined at each time step.

It is important to point out one important characteristic of the Contact Dynamics algorithm: since a constant time step dt is employed to integrate Newton's equations, more than one contact can occur in each time step. In this case, it is assumed that all of the contacts occur simultaneously and the dynamical rules in Equation (4.1), along with the frictional constraint, are applied to each contact.

This produces a set of algebraic equations that might be coupled since a single grain could have more than one contact. Therefore, the value of a specific contact force depends not only on properties of the pair of contacting grains, but also on the properties of other grains in the connected cluster. Physically, this corresponds to the effects of contact forces propagating through a network of grains much faster than contacts are created and/or destroyed. The CD algorithm explores the limit of infinitely rigid grains by assuming that this propagation occurs instantaneously.

This property of multiple collisions is a very important aspect of granular flow in the rigid grain limit. In the absence of such an interaction, when only binary collisions are admitted, an inelastic collapse is observed where an infinite number of collisions occurs in a finite amount of time [66, 67, 68]. This severely restricts the regime of rigid grain flows attainable through simulation unless multi-grain interactions are allowed, as they are in the Contact Dynamics algorithm.

4.2 Simple Shear Flow

We implement simple shear flow using Lees-Edwards (LE) boundary conditions along with the SLLOD equations of motion. In this configuration, density and shear rate are prescribed and other observables are measured. By virtue of the

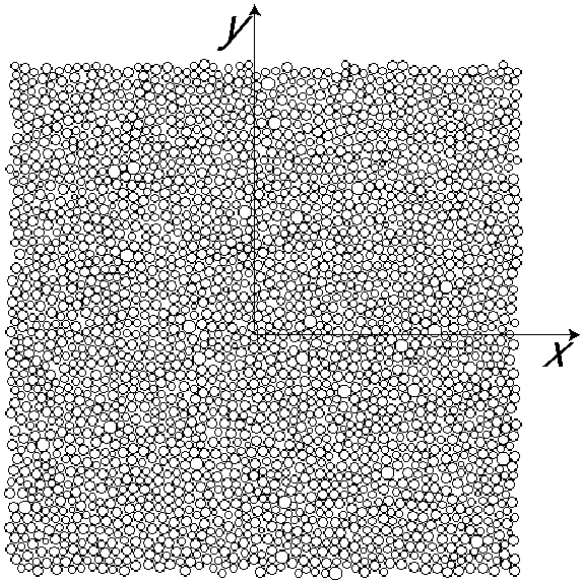

Figure 4.1: Screenshot of a simulation in the simple shear configuration. Each grain has an average velocity in the x-direction given by $\dot{\gamma}y$, where $\dot{\gamma}$ is the strain rate. The center of the cell is defined as $x = y = 0$.

LE boundary conditions, the simulation cell is translationally invariant. Using this configuration we can characterize the steady state relation between stresses, granular temperature and strain-rate and extract numerically the parameters of a constitutive law for granular materials. A screenshot of this shearing geometry is shown in Figure 4.1.

4.2.1 Algorithmic Details

The simple shear simulations are performed using Lees-Edwards (LE) boundary conditions, which allow for the shear deformation of a system by controlling

the positions of the image cells [69]. In all of the simple shear simulations we perform, we impose a constant strain rate $\dot{\gamma}$ so that a grain at position y is given an average velocity of $\dot{\gamma}y$ in the x-direction. This requires that the image cells be moving at a velocity $\dot{\gamma}Y$, where Y is the center vertical component of the cell position. Due to this constraint, a grain that exits the top (bottom) of the computation cell re-enters at the bottom (top) with a different velocity and position in the x-direction; a grain that exits the computation cell in the x-direction simply re-enters with the same velocity and position, on the opposite side.

It was demonstrated in early implementations of LE boundary conditions that when deformation is applied through the image cells, the information needs time to propagate from the cell boundaries to its center. In order to ensure fast propagation of this information and prevent the cell boundaries from making unphysical contributions to the motion, it is necessary to modify Newton's equations by introducing so-called SLLOD terms. These terms can be understood as a "shear bath", with all particles in the cell being directly coupled to the overall deformation [70]. In practice, the SLLOD terms introduce a perturbation to the equations of motion that gives each grain an average velocity consistent with simple shear flow. If we separate the momentum $\mathbf{p}^i$ of each grain i into the average part $m^i\dot{\gamma}y^i\hat{\boldsymbol{x}}$ and fluctuating part $\tilde{\mathbf{p}}^i$, so that $\mathbf{p}^i = m^i\dot{\gamma}y^i\hat{\boldsymbol{x}} + \tilde{\mathbf{p}}^i$, then the SLLOD equations

read:

$$\frac{d\mathbf{r}^i}{dt} = \frac{\tilde{\mathbf{p}}^i}{m^i} + \hat{\boldsymbol{x}}\dot{\gamma}(\mathbf{r}^i \cdot \hat{\boldsymbol{y}}), \quad \frac{d\tilde{\mathbf{p}}^i}{dt} = \sum_j F^{ij} - \hat{\boldsymbol{x}}\dot{\gamma}(\tilde{\mathbf{p}}^i \cdot \hat{\boldsymbol{y}}). \tag{4.2}$$

The equation for the position $\mathbf{r}^i$ results from writing the momentum in terms of an average and fluctuating part. The equation for $\tilde{\mathbf{p}}^i$ contains a new term $\hat{\boldsymbol{x}}\dot{\gamma}(\tilde{\mathbf{p}}^i \cdot \hat{\boldsymbol{y}})$ which forces the shear flow. Since every grain in the computation cell is acted upon by this mechanical force, the constant strain rate is imposed on all of the grains simultaneously at the beginning of the simulation. This can be easily appreciated by writing the equations of motion (4.2) in terms of just the position. This yields

$$\frac{d^2\mathbf{r}^i}{dt^2} = \frac{1}{m^i}\sum_j F^{ij} + \hat{\boldsymbol{x}}\frac{d\dot{\gamma}}{dt}(\mathbf{r}^i \cdot \hat{\boldsymbol{y}}). \tag{4.3}$$

We see that Newton's equation of motion is only altered by including a term with the time derivative of the shear rate. Because we will only consider simple shear flow simulations with a constant shear rate, the new term will be non-zero just at the beginning of the simulation. At this time it will serve to set the initial velocities of the grains such that $\mathbf{p}^i = m^i\dot{\gamma}y^i\hat{\boldsymbol{x}}$. After this initial intrusion, the new term will always be zero and the shear flow will be upheld by the LE boundary conditions. Furthermore it can be proven that, in the LE geometry, the SLLOD equations give an exact representation of simple shear flow arbitrarily far from equilibrium [42, 70].

For a granular material with non-zero friction coefficient μ, the equations of motions must also incorporate rotations of the grains (for $\mu = 0$ the tangential contact force is always zero and there is no rotation). It is expected that a SLLOD term should arise in the equations of motion for the angular velocity since, in the linear velocity profile indicative of simple shear flow, the top and bottom of every grain should move with slightly different velocities. This will give each grain an average rotation of $\dot{\gamma}/2$ which must be incorporated in Equation (3.2) just as the average velocity $\hat{\boldsymbol{x}}\dot{\gamma}(\mathbf{r}^i \cdot \hat{\boldsymbol{y}})$ was incorporated in Equation (4.2). This leads to the following equations in two dimensions:

$$\frac{d\theta^i}{dt} = \tilde{\omega}^i + \frac{\dot{\gamma}}{2}, \quad \frac{d\tilde{\omega}^i}{dt} = \frac{1}{I^i}\sum_j R^i \hat{\boldsymbol{\sigma}}^{ij} \times F^{ij}, \tag{4.4}$$

where $\tilde{\omega}^i$ denotes the fluctuating part of the angular velocity. Equations (4.2) and (4.4) now give an exact representation of simple shear flow for a frictional granular material arbitrarily far from equilibrium.

The primary interest of this procedure is that it permits us to simulate a sheared granular material with a homogeneous shear rate. Experimental procedures, *e.g.* in a Couette cell, do not guarantee that the strain rate is homogeneous: the existence of walls induce a non-uniformity of the flow and possibly localization of the deformation. This protocol grants direct access to the rheology of the

granular material in a self-averaging situation. This is a starting point to the understanding of more complicated flows.

4.2.2 Bulk Measurements

Here we are interested in bulk macroscopic properties of granular flows. In particular we will concentrate on the stress tensor and granular temperature, which depend sensitively on both the dynamics of individual grains and the contact forces between interacting grains.

The granular temperature T is measured as an average over all grains of the fluctuating part of the velocity. More precisely we have

$$TN = \sum_i (\mathbf{v}^i - \mathbf{V})^2 + \frac{1}{2} \sum_i (R^i \omega^i - R^i \Omega)^2, \tag{4.5}$$

where N is the total number of grains, $\mathbf{V}$ is the average velocity and Ω is the average angular velocity. This definition takes into account both the rotational and translational parts of the granular temperature.

Because we are only interested in bulk properties, the stress tensor from Equation (2.7) can be simplified using $\mathcal{G} = A^{-1}$, where A is the total area of the

two-dimensional computation cell. This yields

$$\Sigma_{\alpha\beta} A = \sum_{i=0}^{N} m^i (v_\alpha^i - V_\alpha)(v_\beta^i - V_\beta) + \frac{1}{2} \sum_{\{i,j\}=0}^{N_c} \sigma_\alpha^{ij} F_\beta^{ij}, \tag{4.6}$$

with $\mathbf{F}^{ij}$ representing the contact forces, and $\boldsymbol{\sigma}^{ij} = \mathbf{r}^i - \mathbf{r}^j$. The first sum runs over all grains i and the second sum runs over all contacts between grains.

The symmetric stress tensor has three independent scalar values in two dimensions. We will always express the stress tensor in terms of the pressure $p = (\Sigma_{xx} + \Sigma_{yy})/2$, the shear stress $s = \Sigma_{xy} = \Sigma_{yx}$, and the first normal stress difference $N_1 = (\Sigma_{xx} - \Sigma_{yy})/2p$. Previous research [71, 27] has shown that $N_1 \sim 10^{-2}$. We will therefore ignore this component of the stress tensor and concentrate on the pressure and shear stress, which give the largest contribution.

We begin by demonstrating that Bagnold's scaling, which we have argued should hold exactly for perfectly hard grain flows, is upheld in our simple shear simulations. In Figure 4.2 we show raw data of the normalized pressure $p\dot{\gamma}^{-2}$ as function of shear strain (strain rate multiplied by time), at a packing fraction of 0.8 with no friction and at two different values of the shear rate.

According to the invariance in Newton's equations, which predicts Bagnold's scaling, $p\dot{\gamma}^{-2}$ should be independent of $\dot{\gamma}$, and this behavior is confirmed by the measurements in Figure 4.2. Although the shear rates in the plots differ by a

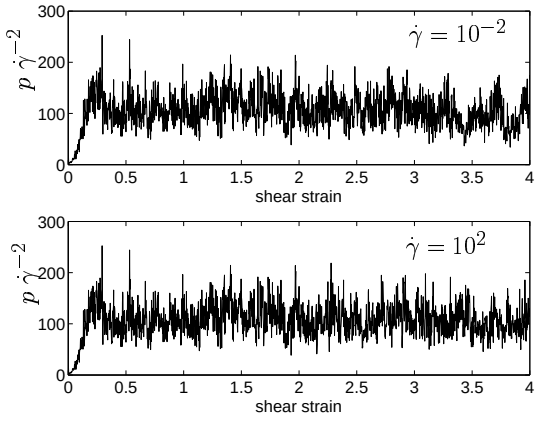

Figure 4.2: Raw data of the pressure p (in arbitrary units) as a function of total shear for two frictionless granular materials with packing fraction 0.8. Data from simulations with different shear rates $\dot{\gamma}$ are shown. The top plot corresponds to $\dot{\gamma} = 10^{-2}$ and the bottom to $\dot{\gamma} = 10^{2}$. The pressure is normalized by $\dot{\gamma}^2$ which collapses the two data sets on to one master curve (i.e. with this rescaling the top and bottom traces appear essentially identical, up to numerical noise), as predicted by the invariance for hard grain systems.

factor of 10^4, the normalized pressure is virtually identical for both systems. Interestingly, not only do the steady state values show no shear rate dependence, but the initial transient is virtually identical for both values of $\dot{\gamma}$.

The invariance in Newton's equations also predicts that $s\dot{\gamma}^{-2}$ and $T\dot{\gamma}^{-2}$ are independent of $\dot{\gamma}$. For all of the simulations we have carried out these predictions from the invariance are upheld: although numerical noise often disrupts the perfect invariance for large values of shear strain, we see no change in the steady state values of normalized pressure, shear stress, or granular temperature as the shear rate is varied at constant density. These results are not surprising– the Contact Dynamics algorithm is a method to simulate perfectly hard grains and the invari-

ance in Newton's equations only holds for perfectly hard grains– but they offer assurance that the simulations are accurate.

The data in Figure 4.2 also ensures us that the time step we use is small enough. From an algorithmic standpoint, scaling the strain rate amounts to a change is the time step. The good scaling of this data ensures that our algorithm solves the equations of hard-grains in a limit where the time step becomes irrelevant. It indicates that the number of contacts per grain in our simulation is not simply an artifact of the finite resolution of the Contact Dynamics methods.

For a granular simple shear flow characterized by its pressure p, shear stress s, temperature T, and strain rate $\dot{\gamma}$, we can construct three independent invariant and unitless quantities: s/p, $\dot{\gamma}\langle R\rangle/\sqrt{T}$, and $mT/p\langle R\rangle^2$, where $\langle R\rangle$ and m are the average grain radius and mass. In Figure 4.3 we show values of these three independent invariant quantities as a function of shear strain for a frictionless granular material at packing fraction of 0.8. For all quantities, steady flow is reached by a shear of approximately 0.5, and we will subsequently provide stationary data by time-averaging our measurements in the steady flow regime. We note from Figure 4.3 that the values of s/p and $mT/p\langle R\rangle^2$ fluctuate much more than $\dot{\gamma}\langle R\rangle/\sqrt{T}$. This is due to the fact that s and p depend on the forces between grains, which are highly fluctuating in the hard grain limit.

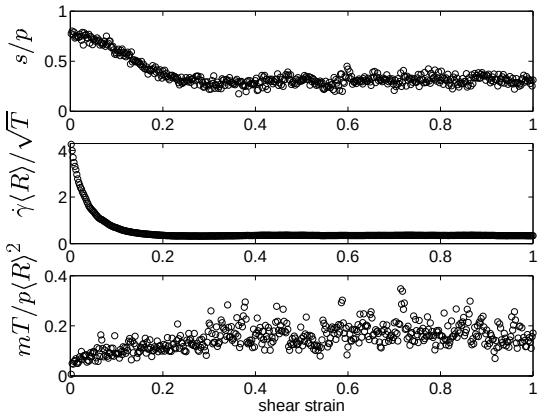

Figure 4.3: Invariant and dimensionless quantities s/p (top), $\dot{\gamma}\langle R\rangle/\sqrt{T}$ (middle), and $mT/p\langle R\rangle^2$ (bottom), where $\langle R\rangle$ is the average grain radius and m the average grain mass, as a function of shear strain for a frictionless granular material at packing fraction 0.8.

The transients in Figure 4.3 are highly dependent on the initial configuration of grains and we will not focus on their development here. Rather we will focus on the steady state values of macroscopic variables. In Figure 4.4 we present the steady state values of $p\dot{\gamma}^{-2}/m$, $s\dot{\gamma}^{-2}/m$, $T\dot{\gamma}^{-2}/\langle R\rangle^2$, and s/p in simple shear for a range of high packing fraction systems that we have studied, at zero friction. Although there is relatively little change in these quantities for small packing fraction, for packing fractions larger that 0.75 there is a large increase in the values of the stresses and granular temperature.

Both the shear stress and pressure are seen to diverge at a finite packing fraction in Figure 4.4. This is because the free volume diminishes as the grain packing increases and the geometry of the packing requires larger stresses in order

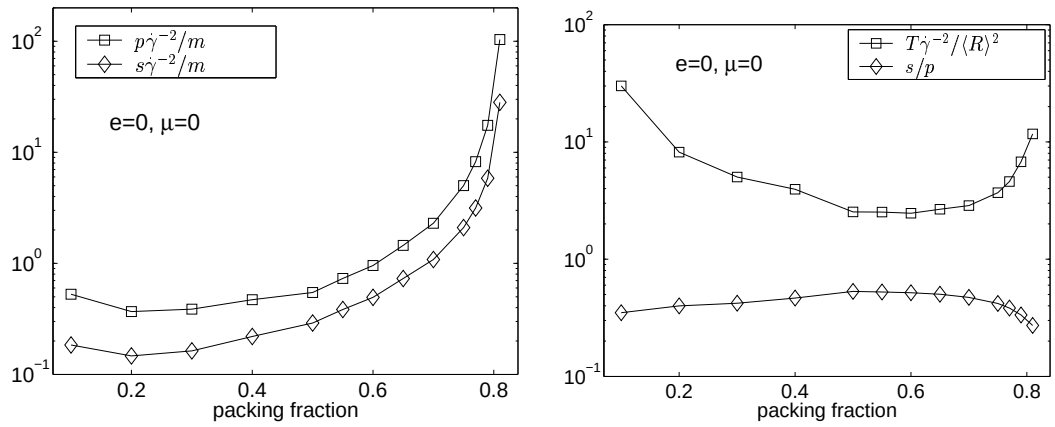

Figure 4.4: Left: Steady state values of $p\dot{\gamma}^{-2}/m$ and $s\dot{\gamma}^{-2}/m$ where m is the average grain mass; **Right** Steady state values of $T\dot{\gamma}^{-2}/\langle R\rangle^2$ and s/p where $\langle R\rangle$ is the average grain radius. Both plots are for granular flows with $\mu = 0$ and $e = 0$ as a function of packing fraction.

to maintain a constant shear rate. Since the granular temperature also begins to diverge at large packing, a central question is whether the divergence in the stress tensor is due to the granular temperature or the forces between grains.

The stress tensor is composed of two parts, a kinetic (or streaming) contribution that arises from the granular temperature and a static contribution that arises from forces between grains. Each of these components can be seen in Equation (4.5)– the first term in this equation is the streaming contribution and the second is the static contribution.

As a simple test of whether kinetic effects on the stress tensor are large, we compare the kinetic part of the pressure to the static part of the pressure. Both the kinetic and static pressures are computed as one-half the trace of the stress

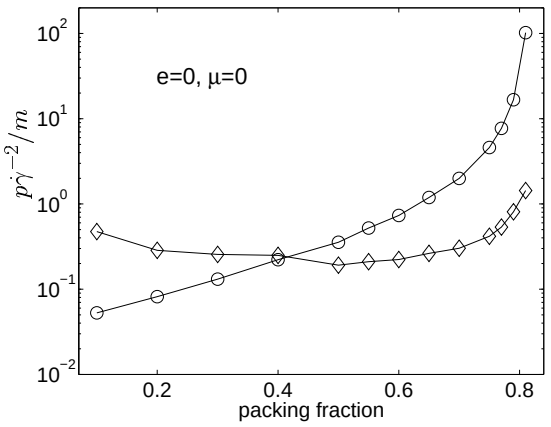

Figure 4.5: The static pressure p^s (circles) and the kinetic pressure p^k (diamonds) as a function of packing fraction for $e = 0$ and $\mu = 0$. The static pressure becomes the dominant contribution to the pressure for large values of packing fraction.

tensor, but the kinetic pressure p^k is determined by the first term in Equation (4.6) whereas the static pressure p^s is determined by the second term. In Figure 4.5 we plot both the static and kinetic part of the pressure for a granular flow with $e = 0$ and $\mu = 0$. We see that the static part of the pressure becomes larger than the kinetic part for $\nu > 0.4$. This means that at large packing fraction, momentum transfer via the stress tensor is dominated by contributions arising from inter-grain forces. Although the exact crossover value of ν depends on both e and μ, Figure 4.5 demonstrates that an understanding of inter-grain forces is necessary to predict the stress tensor in dense granular flows and to reveal the origin of the divergence at finite packing.

To this point, all the data we have presented has been for frictionless systems with restitution $e = 0$. For other values of e and μ, the data and conclusions are

qualitatively the same, although there are some quantitative differences. This can be appreciated easily by observing how the pressure depends on the restitution coefficient. In Figure 4.6 we plot the static part of the pressure (one-half the trace of the static stress tensor from Equation 2.8) as a function of packing fraction, for many different values of e with $\mu = 0$. For large packing fractions the pressures become independent of e. This is due to the fact that, at high packing fraction, the dynamics is solely determined by geometric constraints and the exact amount of energy dissipated in each collision is no longer important. At low values of packing fraction the dynamics becomes less linked to geometric constraints and there is a large variance with e. Although we do not show it here, as μ is increased from zero the large packing fraction limit curve moves slightly, but the same behavior is observed for different values of e.

4.3 Incline Flow

In addition to simple shear flow, we implement granular flow down an inclined plane made of stationary grains. This geometry is more realistic than the simple shear case and has been the focus of many recent experiments [56, 72, 73, 74, 30, 75] and simulations [54, 25, 55]. Following previous simulation studies, our simulation cell is periodic in the direction (x) parallel to the plane and the flow

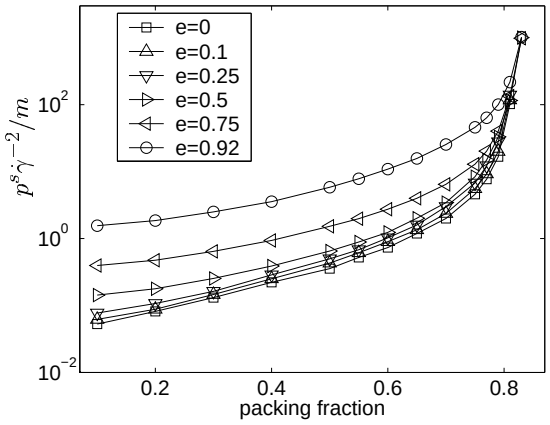

Figure 4.6: Static pressure, arising from forces between grains, as a function of packing fraction for many different restitution coefficients e. We see that as the packing fraction increases, the value of p^s becomes independent of e. This data is for $\mu = 0$, but similar behavior is seen for different values of μ.

is inhomogeneous in the perpendicular (y) direction. In this configuration the stresses are prescribed by the angle of the incline and we perform x-averaged, y-dependent measurements of granular temperature, velocity profiles and strain-rate. Large heights of the granular layer grant access to the bulk rheology of the flow, which permits us to check the existence of a well-defined bulk rheology in the large height limit, and to compare it with the measurements in simple shear. A picture of this shearing geometry is shown in Figure 4.7.

4.3.1 Algorithmic Details

In this geometry, the Contact Dynamics algorithm is used in conjunction with a set of static grains. The static grains make up the one dimensional incline wall

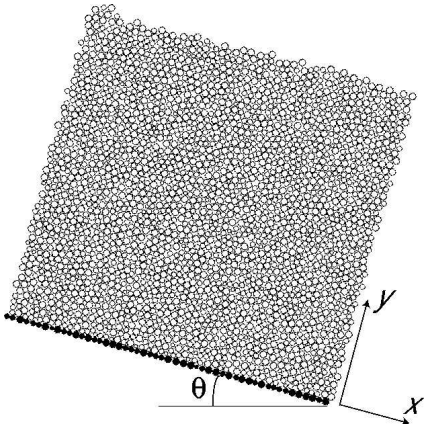

Figure 4.7: Snapshot of a granular material simulation in the incline flow configuration. Fixed grains (indicated by filled circles) create a stationary incline at angle θ on which the flowing grains are accumulated and allowed to flow. Gravity drives the motion and is directed vertically downward.

that all of the two dimensional dynamic grains rest on and, while they do transmit forces, they are required to be stationary at all times. The diameters of the static grains are randomly chosen from the same distribution as the dynamic grains. This is a flat distribution with minimum and maximum grain diameter $\sigma \pm \Delta$ where $\sigma = 1.4$ and $\Delta = 0.26\sigma$.

Flow is initiated by tilting the plane of static grains by an angle θ. In agreement with previous simulations [25] and experiments [56], we do not observe steady flow unless $\theta > \theta_c$, where the value of θ_c depends on the grain distribution and the amount of friction. In contrast to earlier studies, however, there is motion for $\theta < \theta_c$. This is because the Contact Dynamics algorithm can only simulate grains that are flowing and it is therefore impossible to create a perfectly jammed steady

state. We identify the critical angle θ_c by the angle below which the average velocity fluctuates around zero.

Here we will concentrate on the flowing characteristics of perfectly rigid grains down a perfectly rigid incline plane. Therefore we restrict our attention to the steady state characteristics of flows with $\theta > \theta_c$ and measure how the granular temperature, packing fraction, and stress tensor depend on the height above the plane (y) and the inclination angle (θ). To determine these profiles, we average the quantities over all of the x-direction and over a height in the y-direction of 3 grains. We have conducted simulations with heights and widths ranging between 25 and 300 grain diameters and have used different averaging techniques to ensure that our results do not depend on the size of the system or the averaging height.

4.3.2 Bulk Measurements

In Figure 4.8 we plot the packing fraction, average flow velocity down the incline, granular temperature, shear stress, and pressure as a function of height for the steady flow of a non-frictional granular material with $\theta = 12°$. The pressure and shear stress are normalized by $mg\langle R\rangle^{-1}$, where m is the average mass, g is the acceleration of gravity and $\langle R\rangle$ is the average grain radius. Similarly, the average flow velocity is normalized by $\sqrt{g\langle R\rangle}$. These profiles are all in agreement with previous simulations conducted using a different method [25] and including

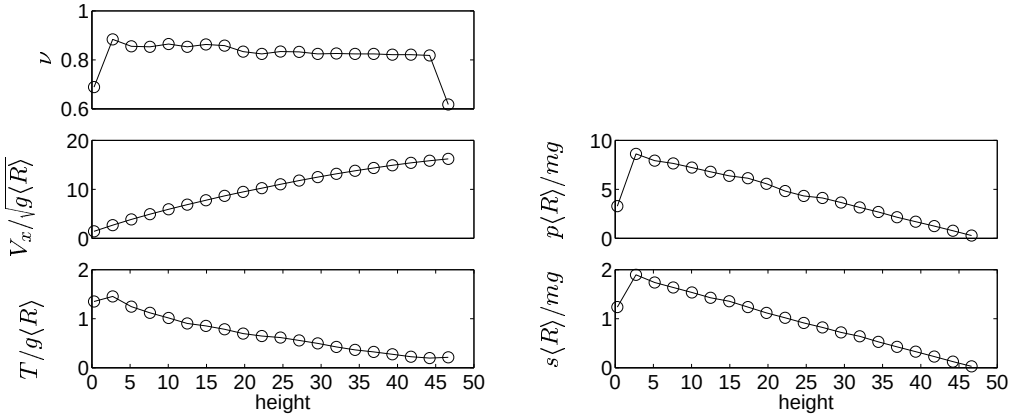

Figure 4.8: Profiles of packing fraction ν, average velocity $V_x/\sqrt{g\langle R\rangle}$, granular temperature $T/g\langle R\rangle$, pressure $p\langle R\rangle^2/mg$, and shear stress $s\langle R\rangle^2/mg$ as a function of the height (y) in the pile, measured in grain diameters, for a non-frictional granular material at a 12° incline. The acceleration from gravity is denoted g and the average grain radius is $\langle R\rangle$.

friction. Indeed, when we include friction in the Contact Dynamics simulations, the functional form of the profiles is the same, while only the coefficients change.

In the bulk of the flow, where the boundaries do not play a role, the packing fraction is constant and the granular temperature is linear. The y-dependence of the average flow velocity is very close to $y^{3/2}$, consistent with previous studies [25]. Both the shear stress and pressure have a linear profile in steady state which can be understood from momentum conservation. Because it is observed that there is no average velocity in the y-direction, Equation 2.2 simplifies to read

$$0 = -\frac{\partial}{\partial r_\beta}\left[\Sigma_{\alpha\beta}\right] + \rho g_\alpha, \tag{4.7}$$

where we have included the effects from gravity. Since the packing fraction is observed to be relatively constant, ρ does not depend on the position in the incline and therefore this equation can be integrated to yield

$$\Sigma_{yy}(y) = g\rho(h-y)\cos\theta \tag{4.8}$$

$$\Sigma_{xy}(y) = g\rho(h-y)\sin\theta, \tag{4.9}$$

where h is the total height of the incline layer. This argument shows concretely that the shear stress must depend linearly on y, but because it does not determine Σ_{xx} it does not prove that the pressure also must depend linearly on y. The fact that the pressure does depend linearly on y shows that Σ_{xx} must also depend linearly on y.

Given the quantities T, p, s, and $\dot{\gamma}$, Bagnold's scaling requires that T, p and s all be proportional to $\dot{\gamma}^2$. This implies that these four quantities produce three invariant quantities, which can be written as $\dot{\gamma}\langle R\rangle/\sqrt{T}$, s/p, and $mT/p\langle R\rangle^2$. These three invariant quantities should only depend on the packing fraction and *not* on y. In Figure 4.9 we plot the three invariant quantities for the frictionless flow with $\theta = 12^\circ$ and do indeed observe that the ratios are constant in the bulk of the flow. This is surprising since the arguments regarding an invariance in Newton's equations only strictly applied to flows in the absence of gravity. For

incline flow, gravity drives the motion, therefore we might expect Bagnold's scaling to break down.

However, the data in Figure 4.9 demonstrates that, in the bulk of the flow down an incline, it is possible to view different layers of granular material as an effective simple shear cell. Such a layer of granular material at height y responds essentially as if it was confined in a simple shear cell, in the absence of body forces, with sustained external stresses $s(y)$ and $p(y)$. Of course the invariance in Newton's equations, which holds exactly for the simple shear cell, is slightly broken by the gravitational force field. However, deep in the bulk of the flow, large confining stresses eventually dominate over the gravitational field. This approximate invariance suffices to predict that Bagnold's scaling must hold for the bulk regions of incline flows and explains the numerical data of Silbert and coworkers [25, 55].

Close to the bumpy grain boundary, the invariant quantities are not constant and Bagnold's scaling breaks down since the requirement that the stationary grains do not move introduces fictitious forces that disrupt the invariance. Additionally, close to the free boundary Bagnold's scaling breaks down because the external force of gravity is dictating the character of the flow and the forces from gravity are not small compared to the internal stresses.

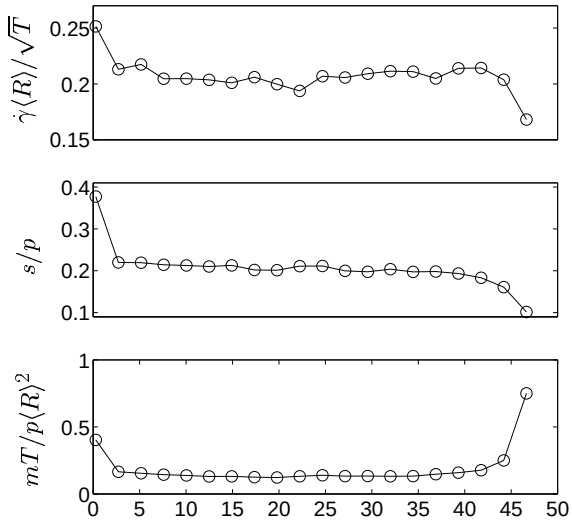

Figure 4.9: Profiles of three invariant ratios as a function of y for a frictionless granular material at $\theta = 12°$. The invariance in Newton's equations for hard grains predicts that these ratios should be independent of y in the bulk of the flow, as observed.

Given that the invariant ratios are constant in the bulk of the flow and only depend on the packing fraction, it is now possible to compare the bulk rheology of incline flow to the bulk rheology of simple shear flow. We explore this connection in the following section.

4.4 A Consistent Bulk Rheology

There are four quantities of interest for shear flows– p, s, $\dot{\gamma}$, and T– and these lead to three independent invariant quantities $\dot{\gamma}\langle R\rangle/\sqrt{T}$, s/p, and $mT/p\langle R\rangle^2$. We observe in our simulations that all of these invariants are constant in the bulk

of the incline flow. Therefore it is legitimate to compare these constant values with the constant values obtained from simple shear simulations. In Figure 4.10 we plot the constant values of s/p, $\dot{\gamma}\langle R\rangle/\sqrt{T}$, and $mT/p\langle R\rangle^2$ from bulk incline flow and simple shear flow, as a function of packing fraction, for both a frictionless system and a frictional system with $\mu = 0.4$. To draw attention to the comparison between incline and simple shear flows, we have only included the large packing fraction data from the simple shear flow simulations. The fact that data from different shear flows fall on the same curves is remarkable and suggests that one theory should be able to describe the rheology of both simple shear and bulk incline granular flow. It also suggests that the packing fraction is the only variable determining the bulk rheology of steady state shear flow in the limit of perfectly rigid grains.

The excellent agreement between the two sets of data challenges the belief that boundary effects are always relevant in dense granular flow of rigid grains [76, 77, 58]. The data in Figure 4.10 supports a very conservative opinion that the motion of the grains decorrelates beyond a finite length scale.

Because the the rheology of incline flows can be matched to the rheology of simple shear flows, we will concentrate on simple shear flows from now on. This is advantageous because the simple shear flow simulations are fast and the algorithm we have developed ensures translational invariance.

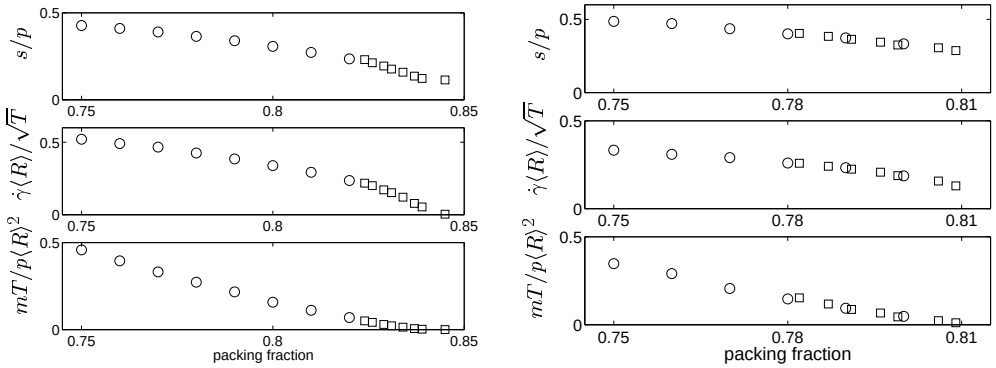

Figure 4.10: The values of s/p (top), $\dot{\gamma}\langle R\rangle/\sqrt{T}$ (middle), and $mT/p\langle R\rangle^2$ (bottom), where $\langle R\rangle$ is the average grain radius and m is the average grain mass, plotted as a function of packing fraction. The left plots correspond to frictionless grains and the right ones to grains with a friction coefficient $\mu = 0.4$. Data from simple shear flow (circles) and flow down an incline (squares) match on the same curves for both cases. This suggests that there is a bulk rheology that is independent of the particular shearing geometry.

Chapter 5

Microstructure of Granular Shear Flow

In the previous chapter we introduced the algorithm used to simulate granular shear flow and presented data for the stress tensor and granular temperature. These are macroscopic measurements that do not depend on the shearing geometry, as long as the measurement is made far from boundaries in the bulk of the flow. The numerically derived constitutive relations in Figure 4.10 are related to the microscopic motion of grains and the contact forces between pairs of grains.

The observation of a unique bulk rheology fosters hope for a general theory of granular flow that will hold in many different geometries. Such a theory should provide constitutive relations, formulated from microscopic considerations and based on a thorough examination of how forces arise on the length scale of individual grains. This, combined with a proper handling of boundary conditions, will allow predictions to be made for an arbitrary flowing geometry. A necessary first

step in constructing these models is to understand the nature of contact forces in granular materials.

At very low packing fraction it can safely be assumed that only binary collisions occur. This is because interactions are rare and it is very improbable to have simultaneous interactions between more than two grains. In this case, contact forces can be determined from velocity distributions, and the constructs of kinetic theory are particularly useful [28, 29]. However, as the packing fraction is increased, theories based on binary collisions become problematic due to inelastic collapse [66, 67, 68], where the energy loss that occurs in each collision causes grains to cluster and eventually reach a state where an infinite number of binary collisions occur in a finite amount of time. This leads to a dense regime [78, 79] at large packing fractions where multi-grain contacts always occur [34, 35, 36] and contact forces are observed to emanate through "force chains" formed by the topology of the contact network [18, 37, 38, 39, 40, 41]. For these large packing fractions the material forms finite sized clusters of simultaneously interacting grains and an analysis based on binary collisions is not useful.

Although the limits of dense and dilute systems are well understood, there has only been limited attention given to how the grain-grain interactions in a flowing granular material make the transition from being dominated by binary collisions to forming coherent force chain networks [79]. In this chapter we will

quantitatively measure the extent of the force chain networks to determine how and when force chains emerge.

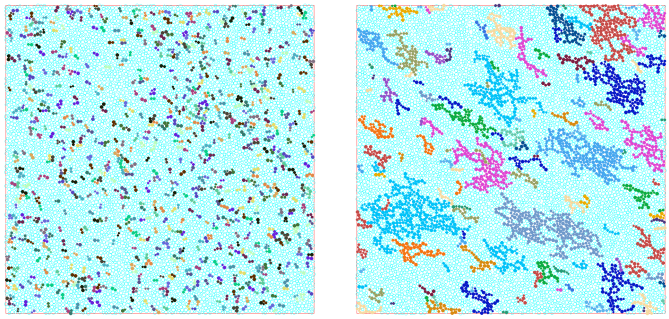

Figure 5.1: Steady state screenshots of sheared granular materials at the same packing fraction of 0.79, but two different restitution coefficients: $e = 0.92$ (left) and $e = 0$ (right). Grains involved in a collision during a small time period are colored, with different colors denoting different contact networks. Interactions tend to be binary for $e = 0.92$, whereas clusters clearly form for $e = 0$.

One of the most basic observations is that both the packing fraction and the restitution coefficient affect the size of force chain networks in the material. In Fig. 5.1 we display two representative screenshots from our simulations, in steady state, for identical shear rate and packing fraction of $\nu = 0.79$, but different restitution coefficients, $e = 0.92$ and $e = 0$. A small time interval is chosen and grains that collide during this time interval are colored. Different colors corresponding to separate contact networks. For $e = 0.92$ the interacting grains are well spaced and tend to occur in pairs, whereas for $e = 0$ the interacting grains tend to form large clusters. These clusters qualitatively indicate the emergence

of persistent contacts for decreasing e. Similar behavior is seen when increasing ν for constant e.

The groups of simultaneously contacting grains that we observe are transient objects, resulting from competition between shear-induced accumulation of new grains and contact break-up due to ambient noise. If the snapshot in Figure 5.1 were taken at a later time, the characteristic size of the clusters would remain the same, but the locations would change.

5.1 Quantifying Microstructure through Correlation

Although the screenshots in Figure 5.1 offer easy visualization of the microstructure in granular flow, they are not quantitatively useful. In order to gain a quantitative measure of the microstructure it is not enough to simply observe which grains are in the same connected cluster, but it is also necessary to demonstrate that any two grains in the connected cluster are correlated and affect one another. Because the clusters form force chain networks, it is natural to define the size of a cluster through correlation between the forces on the grains.

In this spirit, we define the correlation function

$$C(\boldsymbol{\ell}) = \frac{\sum_{i=1}^{N} \sum_{j=1}^{i-1} \mathbf{F}^i \cdot \mathbf{F}^j \delta(\mathbf{r}^i - \mathbf{r}^j - \boldsymbol{\ell})}{\sum_{i=1}^{N} \mathbf{F}^i \cdot \mathbf{F}^i}. \tag{5.1}$$

In this equation, $\mathbf{F}^i$ is the total vector force (sum of contact forces) experienced by a grain i at position $\mathbf{r}^i$ and the sums are taken over all grains that have at least one contact. The distance $\boldsymbol{\ell}$ ranges over the entire system size and is not limited to grains in direct contact. We take the average value of $C(\boldsymbol{\ell})$ over at least 5000 time steps in steady state shear flow. A non-zero value of $C(\boldsymbol{\ell})$ reveals that, on the average, two grains separated by a distance $\boldsymbol{\ell}$ have forces that are correlated.

For perfectly rigid granular materials, where there is only a repulsive interaction between grains *at contact*, $C(\boldsymbol{\ell})$ gives a quantitative measurement of the average affect of force chains of length $\boldsymbol{\ell}$ in the material. A non-zero value of the correlation indicates that two grains a distance $\boldsymbol{\ell}$ are connected through a cluster of simultaneously contacting grains and the force from one grain is being transmitted through the network to the other grain. It thereby establishes that simultaneous contacts exist and that forces propagate through networks. Positive values of the correlation correspond to situations where the total forces on each grain tend to be aligned.

Because we make the measurement of $C(\boldsymbol{\ell})$ while the material is in steady state shear flow, the correlation does not reveal the presence of static structure. Instead, because contacts between grains are being created and destroyed by the overall flow, the correlation function gives information on the average size of dynamic structures that are fluctuating in both space and time.

We will demonstrate that the correlation function depends on the vector distance $\boldsymbol{\ell} = \ell\hat{\boldsymbol{\ell}}$ between pairs of grains, and that it decays exponentially with ℓ. In the following sections, we first investigate the dependence of $C(\boldsymbol{\ell})$ on the magnitude of $\boldsymbol{\ell}$, thereby defining an isotropic correlation length ξ. Then we investigate the full dependence of $C(\boldsymbol{\ell})$ and obtain the full functional form of $\xi(\theta)$, which depends on the angle θ between pairs of grains.

5.1.1 Isotropic Correlation and the length-scale ξ

We begin by measuring the isotropic part of the correlation $C(\ell)$ in our two dimensional simulations by averaging $C(\boldsymbol{\ell})$ over all $\hat{\boldsymbol{\ell}}$. In Figure 5.2 we display measurements of this isotropic correlation function $C(\ell)$ for a frictionless material with $e = 0.25$.

The logarithm of the magnitude of the correlations $\log|C(\ell)|$ is also plotted in Figure 5.2. We observe that the magnitude of the correlations decreases exponentially. This decay is complicated by a oscillating function that accounts for the

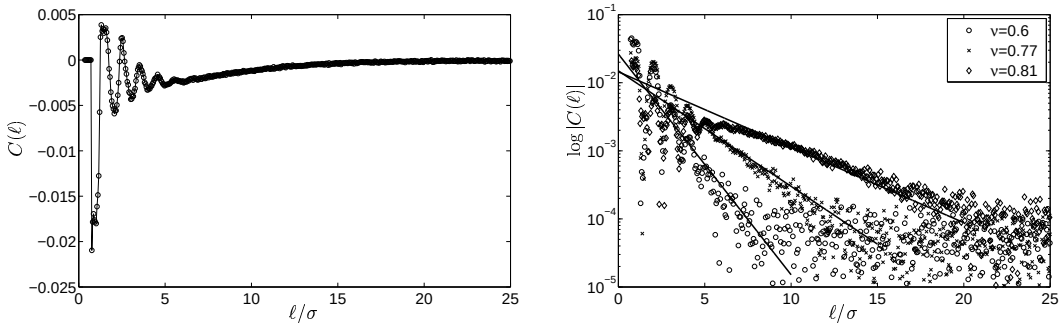

Figure 5.2: Left: The force correlation function $C(\ell)$ for $e = 0.25$ and $\nu = 0.81$, where ℓ is the distance between grains and σ is the average grain diameter. **Right:** The logarithm of the magnitude $\log|C(\ell)|$, for packing fractions of $\nu = 0.6$, 0.77, and 0.81, which displays the exponential decay of the correlations. The lines correspond to the function $e^{-\ell/\xi}$, where ξ is determined from Equation (5.2) and plotted in Figure 5.3.

sign of $C(\ell)$. The form of this oscillating function is not universal and depends on the exact value of density and restitution. Nevertheless, as a first approximation, we can express the correlation function as $C(\ell) \sim \exp(-\ell/\xi)$, which introduces an important length scale ξ. From the data in Figure 5.2 we also see that this length scale increases with packing fraction.

We have determined that the value of ξ is well approximated by the equation

$$\xi = \frac{\int_0^\infty d\ell\, \ell\, C(\ell)}{\int_0^\infty d\ell\, C(\ell)}. \tag{5.2}$$

In Figure 5.2 we plot $\exp(-\ell/\xi)$, where ξ is determined for each density from Equation (5.2) and we observe excellent agreement with the measured exponential decays of $C(\ell)$.

In Figure 5.3 we display measurements of ξ, determined from Equation (5.2), for all of the frictionless granular flows we have simulated. The value of ξ quantifies the average extent of force chains in the system. We notice that ξ is an increasing function of density for each value of restitution. We also notice, in agreement with Figure 5.1, that ξ increases as e decreases. The inset of Figure 5.3 shows a close-up of the large packing fraction data. The maximum packing fraction we are able to simulate is $\nu_{\max} = 0.84$, but we were not able to determine the value of ξ at $\nu_{\max}$ for all values of restitution. This is because the extent of the correlations becomes larger than the maximum system size of 10000 grains that we can simulate. For the high values of packing fraction shown in the inset, we conducted simulations for packing fractions in increments of 0.01. For $e \leq 0.5$ we reach a packing fraction where, if we increase the packing fraction by 0.01, ξ is too large to be measured. The fast growth of the correlations at high packing fraction suggests that ξ diverges at a finite density.

For small values of packing fraction, Figure 5.3 shows the value of ξ approaching a limiting value of 0.785σ. This corresponds to the smallest correlation possible, which arises when the only interactions are binary collisions between grains.

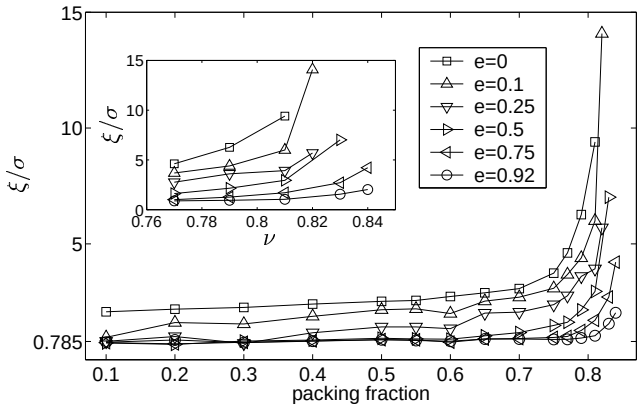

Figure 5.3: Main Figure: The mesoscopic length scale ξ for frictionless granular shear flows, normalized by the average radius σ, plotted for a wide range of packing fraction and restitution e. **Inset:** Closeup of the large packing fraction data.

For these small packing fractions, the sign of $C(\ell)$ is exclusively negative and the exponential decay is not observed. Indeed, in the case of a mono-disperse collection of grains where only binary collisions occur, we observe that $C(\ell)$ is zero for all values of ℓ except $\ell = \sigma$. In the case of a poly-disperse collection of grains, the form of $C(\ell)$ for dilute flows depends on the relative probabilities to have binary interactions between grains of different sizes and exponential decay is not observed since the correlation function equals zero for all values of ℓ larger than the maximum grain diameter. Even though exponential decay is not observed in the limiting case of binary collisions between grains, Equation (5.2) still provides a useful measure of correlation length that matches the exponential decay at higher densities.

The limiting value of 0.785 is related to the probability to have a binary collision between grains of different diameters and is equal to the correlation length that would be expected in a perfectly elastic system. Therefore we will denote the limiting value as $\xi_{\rm el}$ and we find that its numerical value is related to the distribution of grain sizes [79].

Exponential correlations and diverging ξ are also observed for systems with friction between grains. Adding friction introduces a non-zero tangential force at contact that tends to increase geometrical frustration and make it more difficult for grains to find free volume. Therefore, we would expect that the addition of friction would actually increase ξ. As in Figure 5.2, we observe that $C(\ell)$ decays exponentially in frictional systems and measurements of ξ are displayed in Figure 5.4 for $e = 0$ and three friction coefficients μ. We indeed see that the value of ξ diverges faster for systems with friction. However, the correlation length is not changed for small values of packing fraction. This is because clusters of grains must first exist before friction can make an effect. Therefore the initial emergence of the clusters is only related to the properties of normal forces.

The data in Figures 5.3 and 5.4 demonstrates that ξ diverges at a finite packing fraction $\nu_{\rm c}$ that depends on the friction coefficient μ, but not on the restitution coefficient e. This divergence is related to the jamming transition [80] in granular materials, where the shear modulus becomes non-zero and the system is able to

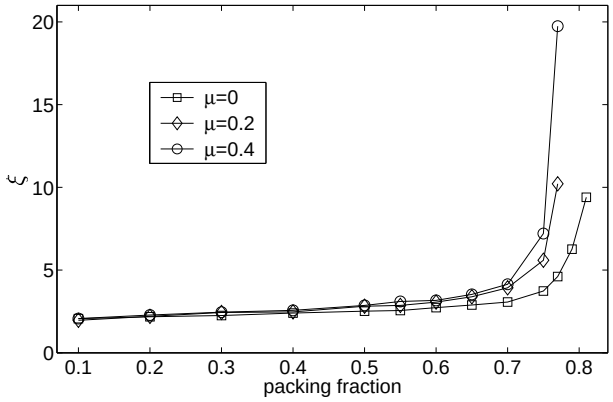

Figure 5.4: The length scale ξ for granular shear flows with friction coefficient μ and $e = 0$. Larger values of μ correspond to larger ξ.

sustain a shear stress without yielding. In order to make the transition from a flowing shear state to a jammed state, it is necessary that a correlation length approach the size of the system, and diverge in the thermodynamic limit. This is because force chains must percolate from the upper to lower shearing wall in order to counteract the applied shearing force. The correlation length ξ quantifies the notion of force chains and we expect that the observed divergence of ξ is a necessary condition for jamming.

However, there is no guarantee that the divergence of ξ is also a sufficient condition for jamming, since it is possible that force chains percolate long before the system jams. However, both theories [81, 82] and simulations [20, 21, 22] have found that percolation and jamming occur simultaneously, which suggests that a granular system jams if, and only if, ξ diverges. In this case, Figure 5.4

implies that the jamming transition occurs at lower packing fraction as the friction between grains increases, as has been observed elsewhere [22].

While the divergence of ξ is related to the jamming transition, the initial deviation of ξ from its elastic value $\xi_{\rm el}$ is related to inelastic collapse [66, 67, 68]. Our results indicate that inelastic collapse is not an unphysical result of the hard-grain model, but rather the precursor to multi-grain contacts in the dense regime [78, 83, 79]. Because an infinite number of binary collisions occur as the material begins its collapse, this allows for non-binary interactions to develop since both the time between binary collisions and the time needed for a single binary collision to occur are both equal to zero.

5.1.2 Anisotropic Correlation and the Angular Dependence of ξ

We have also conducted measurements of the full vectorial dependence of $C(\boldsymbol{\ell})$. In this case, we observe that the decay of the correlations can still be described by an exponential, but the value of the correlation length depends on the orientation $\hat{\boldsymbol{\ell}}$. In two dimensions this orientation can be quantified by the angle θ between $\boldsymbol{\ell}$ and the x-axis. In Figure 5.5 we display the angular dependence of ξ for frictionless flows with $e = 0$ and three different packing fractions. As expected, the average value of ξ increases with packing fraction.

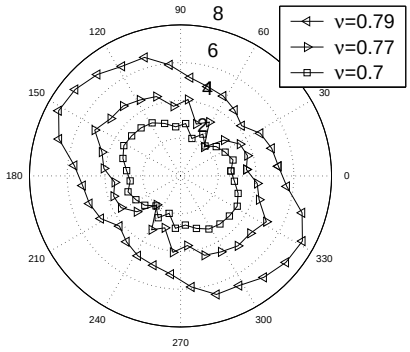

Figure 5.5: The angular dependence of the length scale $\xi(\theta)$ for a frictionless shear flow with $e = 0$ and three different packing fractions ν. The orientation is greatest along the compression axis of the shear flow.

The maximum value of the correlation length occurs at approximately the same angle for each packing fraction in Figure 5.5. This trend is followed for other packing fractions and restitution coefficients as well. In Figure 5.6 we plot the angular dependence of the length scale divided by its average value, $\xi(\theta)/\xi$. We notice that this collapses the data for a large range of packing fractions and restitution coefficients on to one curve. The collapse is not perfect, especially along the dilational axis of the shear flow where the correlations are small. This is due to the small number of collisions that occur on this axis, which makes gathering statistics difficult.

The common collapsed curve for all of the data in Figure 5.6 shows that ξ is anisotropic, which has also been observed in experiments [41]. The angular dependence of ξ can be written as a Fourier series, only including terms that

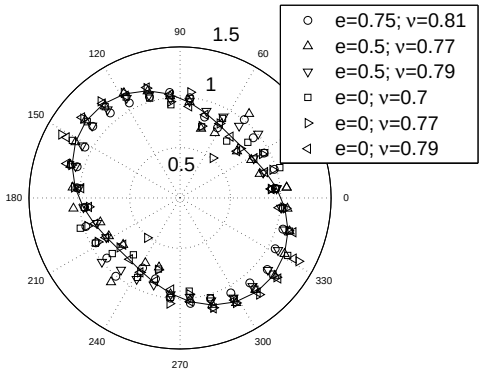

Figure 5.6: The normalized angular dependence of the length scale, $\xi(\theta)/\xi$ for frictionless shear flows with different restitution coefficients and packing fractions. The data is well characterized by Equation (5.3), plotted as a line.

are π-periodic. We find that, as is the case for other anisotropies in granular flow [84, 85, 86, 87, 88], the functional form of $\xi(\theta)$ is well characterized by the first two terms in the Fourier series

$$\xi(\theta) = \frac{\xi}{2\pi}\left(1 - a_0 \sin 2[\theta - \theta_0]\right), \tag{5.3}$$

where ξ is the average value of the correlation length. The solid curve in Figure 5.6 is a fit to this equation, which sets the parameters as $a_0 = 0.21$ and $\theta_0 = 0.013$. The value of θ_0 is consistent with the axis of maximum compression for the data we have gathered. This suggests that larger values of ξ occur near $\theta = 3\pi/4$ because compression causes more grains to come into contact. Near $\theta = \pi/4$,

where ξ is a minimum, dilation reduces the size of the length scale. However, we have found no simple explanation for the value of a_0.

5.2 The Effect of Microstructure on Contact Forces

In the previous section we presented measurements of a correlation length ξ that diverges at the jamming transition and asymptotes to an elastic value $\xi_{\rm el}$ for small packing. This length scale captures the decay of force correlations and is related to the emergence of clusters of simultaneously contacting grains. In very dilute systems only binary collisions are relevant, $\xi = \xi_{\rm el}$, and contact forces can be determined only from the properties of the two colliding grains. However, as the packing fraction is increased, ξ also increases and the contact force between any two grains will depend on properties of the other grains in the cluster. This is because, in the rigid grain limit, forces propagate through the network. Because the growth of ξ is closely related to the nature of the force propagation– binary collisions or force networks– we expect the contact forces to depend on the value of ξ. A useful way to explore properties of contact forces is to measure the contact force distribution function $P(F)$. This function encodes the statistics of the contact forces: $P(F)dF$ is proportional to the number of contact forces in the range F to $F + dF$

5.2.1 The Contribution of Binary Collisions

To make the connection between contact forces and long range spatial force correlations explicit, we begin by demonstrating that the contact forces between contacting pairs of grains can not be determined simply by assuming binary collisions when ξ is large. To illustrate this point, we compare the statistics of the actual contact forces to the forces we would calculate if we assumed that only binary collisions occurred. If we make the binary collision assumption, then the dynamical rule in Equation (4.1), along with momentum conservation, determines the normal impulse in each collision. Dividing this impulse by the algorithm time step yields the average force that would arise over the time step dt. We label this force $F_{\rm bc}^{ij}$, where i and j represent the colliding grains and the label "bc" reminds us that this force only applies to purely binary collisions. It is simple to show that the value of the binary force is given by

$$F_{\rm bc}^{ij} = (1+e)\mu^{ij}\left[(\mathbf{v}'^{j} - \mathbf{v}'^{i})\cdot\hat{\boldsymbol{\sigma}}^{ij}\right]/dt, \tag{5.4}$$

where e is the normal restitution coefficient, $\mu = m^i m^j/(m^i+m^j)$ is the reduced mass, $\mathbf{v}'^{i}$ the pre-collisional velocity of grain i, and $\hat{\boldsymbol{\sigma}}^{ij}$ is the unit vector connecting the centers of grains i and j. All of these terms can be measured directly from simulations.

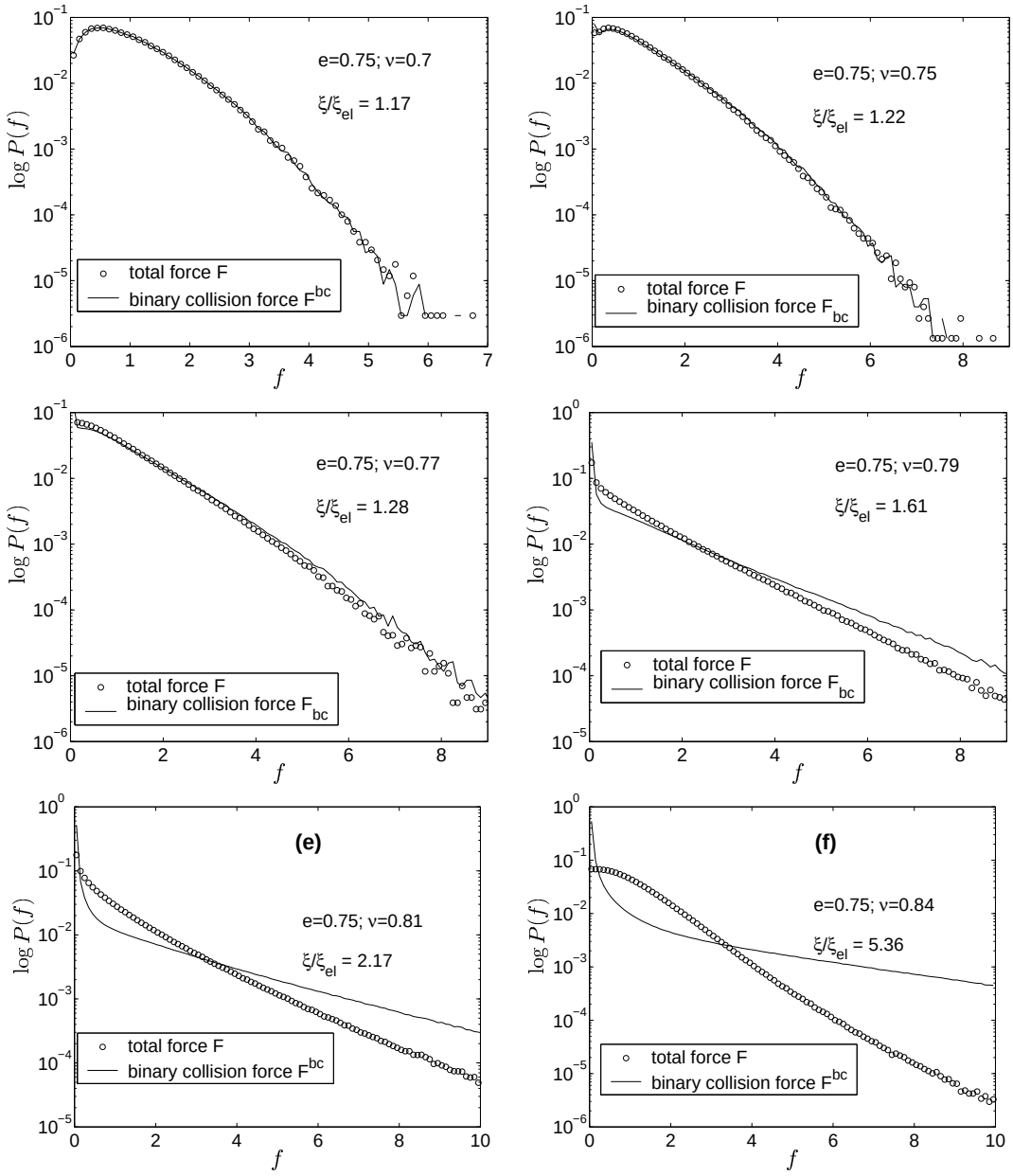

Figure 5.7: The data points are $P(f)$ for systems with $e = 0.75$ and growing values of $\xi/\xi_{\rm el}$, where f is the contact force F divided by the average value $\langle F \rangle$. This data is compared with the line, where the force is determined from Equation (5.4) which assumes that only binary collisions occur. We have normalized both the total forces and binary collision forces in each plot by their average values. There is excellent agreement for $\xi/\xi_{\rm el} < 1.25$. For larger values of the correlation, clusters of interacting grains form and assuming binary collisions does not fit the data.

In Figure 5.7 we plot measurements of the contact force distribution function $P(F)$ for six different values of restitution and packing fraction. In each figure we compare $P(F)$ with the statistics of the binary forces $P(F_{\rm bc})$. If these two functions are the same then contact forces are well approximated by only considering binary collisions; if the functions differ then we know that clusters of contacting grains affect contact forces. We also indicate the value of $\xi/\xi_{\rm el}$ for each plot and immediately see that for small values of $\xi/\xi_{\rm el}$ the data for $P(F)$ is well fit by the line, which is a measurement of $P(F_{\rm bc})$. However, as ξ increases, the presence of force networks changes the nature of the contact forces and we can no longer make accurate predictions by assuming that only binary collisions occur. The value $\xi/\xi_{\rm el} \approx 1.25$ serves as an upper bound for the regime where the binary collision assumption is reasonable. This behavior is not unique to flows with $e = 0.75$, but occurs for all of the restitution coefficients and packing fractions we have investigated, with and without friction.

This is not surprising since $\xi/\xi_{\rm el} > 1.25$ comprises a region where force networks have formed and simultaneous contacts occur. In this regime, in order to calculate the force between two grains, it is not sufficient to only consider the properties of the two contacting grains. Rather, all of the grains connected in the force network play an important role. This is because the two contacting grains are being pushed together by the other grains in the cluster and the contact force is

equal to the binary collision contribution from Equation (5.4) *plus* a contribution from the cluster.

We conclude from Figure 5.7 that $\xi/\xi_{\rm el} = 1.25$ separates the region where only binary collisions occur from the region where force networks begin to form and affect contact forces. The techniques we used to determine this crossover can only be used in simulations where the position, velocity, and force on every grain is always known. However, we have also found a signature of the transition that can (and has been) observed in experiments of granular flows. This signature relates to the small force behavior of the contact force distribution function.

5.2.2 The Contact Force Probability Function P(F)

Comparing $P(F)$ to $P(F_{\rm bc})$ gave a simple criteria to view the transition from the dilute regime, where all interactions between grains are binary, to the dense regime, where force networks become prevalent. In this section we show that this transition can be further appreciated by simply measuring $P(F)$.

In Figure 5.8 we present data for the contact force distribution function $P(F)$. In particular, we plot $\log P(f)$ for many different values of the restitution coefficient and packing fraction, where f is equal to the normal contact force F divided by the average normal force $\langle F \rangle$. All of these curves correspond to frictionless materials, but we have observed that the statistics of the normal forces display

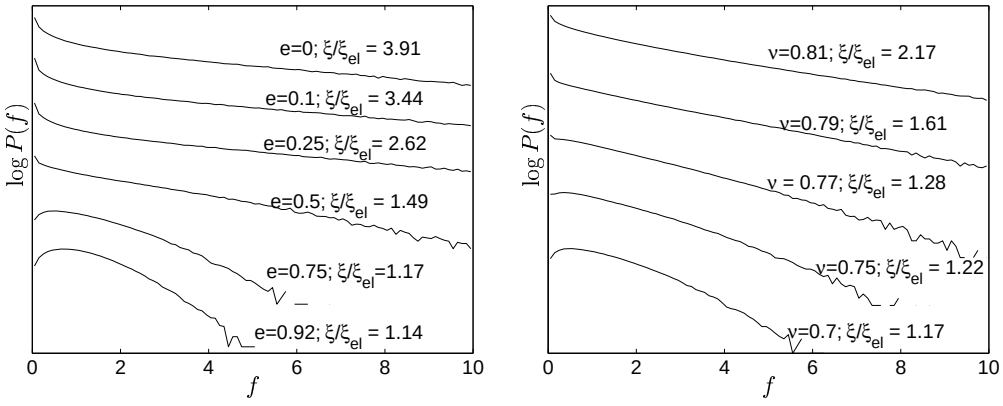

Figure 5.8: Measurements of the contact force probability distribution function $P(f)$, where f is the value of the contact force divided by the average contact force. The different curves have been offset so each curve is easy to see. **Left** Data for $\nu = 0.7$ and different values of the restitution coefficient e. **Right** Data for $e = 0.75$ and increasing values of packing fraction ν. The curves in each plot are also labeled by their associated value of $\xi/\xi_{\rm el}$, and we observe that the peak is present in $P(f)$ only if $\xi/\xi_{\rm el} < 1.22$.

the same behavior for frictional systems. Our measurements of $P(f)$ have been averaged over 5000 time steps in steady state shear flow, and the different curves are vertically displaced in the figure so each can be clearly seen. Each curve is labeled by the value of $\xi/\xi_{\rm el}$ and we immediately see that the behavior at small f depends on the value of ξ. For $\xi/\xi_{\rm el} \leq 1.25$ there is a clear peak, whereas for $\xi/\xi_{\rm el} \geq 1.25$, the peak disappears and the maximum occurs at $f = 0$.

This measurement once again defines a crossover at $\xi/\xi_{\rm el} = 1.25$. This is the transition where the microscopic interactions change from being dominated by binary collisions between grains to being dominated by clusters of grains, forming force networks of size $\xi/\xi_{\rm el}$. When this network transition occurs, the peak dis-

appears and the most likely force is no longer equal to the average force. This is because grains have spontaneously formed into transient clusters and the greatest number of contacts are simply rolling over each other which produces a very small normal force. This moves the peak to $f = 0$ once the transition has fully developed and the average force is not representative of most of the forces. Additionally, as force-networks become long-ranged, the data shows that there is a greater probability of large forces, which arise from a large number of grains in a cluster compressing two contacting grains.

The signature of the transition evident in our measurements of $P(f)$ has been observed in other simulations and experiments, but has never been connected to the formation of large scale structure. Simulations of granular hopper flow [90, 91, 92], conducted using Event Driven simulations where only binary collisions are allowed to occur, have reported that as the hopper aperture is reduced and the density of the packing increases, $P(f)$ begins to lose its peak. This is consistent with our results from Figure (5.8) and suggests that the correlation length ξ is relevant in more than just shear flows of granular media. Additionally, experiments on hopper flow [93] have observed the same behavior in $P(f)$, which lends credibility to the result and suggests that it is not an artifact of the simulation methods used here and in Refs. [90, 91], but rather a real effect in granular flows.

The results we have cited from hopper flow, and others [92], have been used to challenge the belief that the formation of a peak in $P(f)$ is a signature of the jamming transition [94, 95]. In a wide variety of contexts, including incline flow [95], quasi-static flow [38, 96], and jammed granular materials [97, 98, 99, 100] it has been observed that $P(f)$ exhibits a maximum at $f = 0$ (no peak) if the system is flowing, while a peak at non-zero f forms as the systems jams. These observations, coupled with similar results in Lennard-Jones glasses and foams [94], have been used to bolster the claim that the formation of a peak in $P(f)$ is a generic characteristic of the jamming transition, and a necessary condition for the appearance of a yield stress.

Our observations reveal that, in fact, there are two important transitions encoded in the small f behavior of $P(f)$. First, at a low packing fraction, there is the interaction transition where the interactions between grains change from binary collisions to force networks. This occurs in the inertial flow regime and is accompanied by a change in $P(f)$ where the peak that was present for small densities disappears and the maximum value of $P(f)$ occurs at $f = 0$. Then, as shown elsewhere, there is another transition at higher packing fraction where the system develops a yield stress and the peak reappears in $P(f)$.

In summary, we have measured contact force distribution in this section to determine the effects of long-range correlation. We find that $\xi/\xi_{\text{el}} = 1.25$ separates

the regime where only binary collisions occur from the regime where force networks form. This observation allows us to split the inertial regime where hard-sphere granular flows exist into two distinct regions. At low packing fraction there is a "dilute regime" where binary collisions are the dominant microscopic interaction and $\xi/\xi_{\mathrm{el}} < 1.25$. At high packing fraction there is a "dense regime" where force networks exist but do not percolate through the system. This dense regime is characterized by clusters of interacting grains with an average extent ξ/ξ_{el} in the range of $1.25 < \xi/\xi_{\mathrm{el}} < \infty$. For dilute flows where only binary collisions occur, a peak is visible in $P(f)$; as force networks begin to appear in the dense regime, the peak disappears.

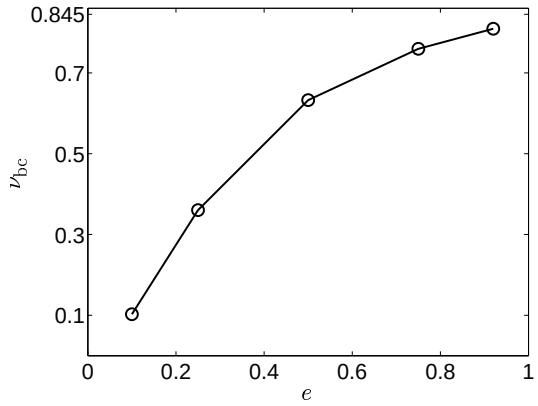

Figure 5.9: The value of ν_{bc} as a function of restitution coefficient e. Below $\nu_{\mathrm{bc}}(e)$ only binary collisions are relevant and above ν_{bc} force networks emerge. We have included the approximate value of $\nu_{\mathrm{c}} \approx 0.845$.

The crossover at $\xi/\xi_{\mathrm{el}} = 1.25$ defines the transition between interactions dominated by binary collisions and interactions dominated by force networks. There-

fore, we use this value to defined $\nu_{\rm bc}(e)$, which is the value of the packing fraction below which only binary collisions are relevant. This function is plotted in Figure 5.9 using the data for ξ from Figure 5.3. This plot is for frictionless materials $\mu = 0$, but increasing the value of μ does not change the curve. This is because, as we saw in Figure 5.4, the effects of friction to not take hold until ξ is much larger than $1.25\xi_{\rm bc}$. Thus $\nu_{\rm bc}$ is an important packing fraction for all values of friction and we see that it is an increasing function of e. This is because larger e produces less energy dissipation and restricts grain clustering. The data in Figure 5.9 implies that as $e \to 1$ then $\nu_{\rm bc} \to \nu_{\rm c}$, which is the packing fraction at which the system jams. This means that as grains become perfectly elastic and no energy is dissipated at contacts, then binary collisions describe the interactions for all values of packing fraction in the inertial regime.

5.3 Phase Diagram of Granular Flow

In this chapter we have measured correlation between grain-forces in inertial shear flows. This correlation is long ranged, decaying with a characteristic length scale ξ that diverges at the jamming transition and asymptotes to an elastic value $\xi_{\rm el}$ in the dilute limit. By investigating the statistics of contact forces between grains, we have shown that $\xi/\xi_{\rm el} = 1.25$ splits the inertial regime into dilute flows,

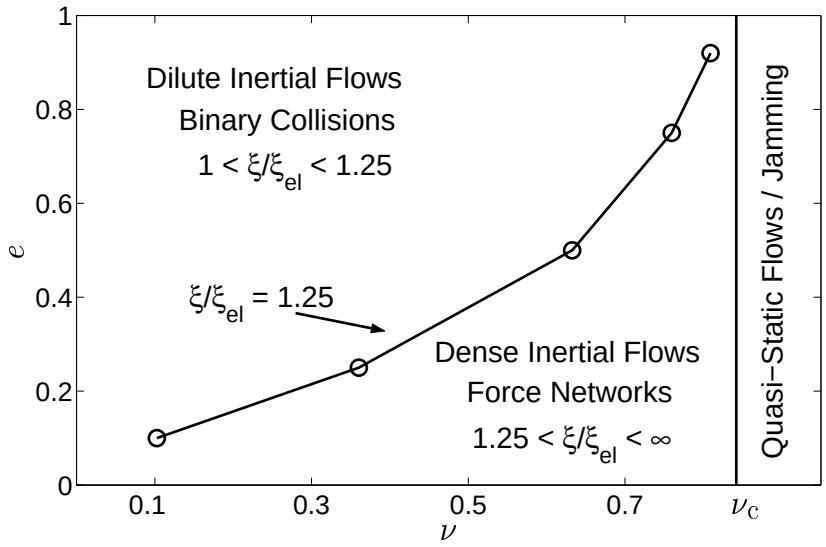

Figure 5.10: Phase diagram of granular shear flow, plotted as a function of the packing fraction ν and the restitution coefficient e. For our system, we estimate that $\nu_c \approx 0.845$, which is represented by the vertical line on the plot. The value of ν_c separates the inertial regime from the quasi-static regime and has been studied elsewhere [19]. Here we focus on the inertial regime and have shown that there is an important packing fraction ν_{bc}, where $\xi/\xi_{el} = 1.25$. Our measured values of ν_{bc} depend on the restitution coefficient and are plotted on the phase diagram. For $\nu < \nu_{bc}$ the flow is in the Dilute Inertial regime where microscopic interactions consist of binary collisions; for $\nu > \nu_{bc}$ the flow is in the Dense Inertial regime where long ranged force networks begin to form.

where all forces arise from binary collisions between grains, and dense flows, where force chains begin to form. We denote ν_{bc} as the packing fraction at which $\xi/\xi_{el} = 1.25$ and we find that ν_{bc} depends on the restitution coefficient, but is always less than the packing fraction ν_c at which the system jams. This phenomenology is illustrated in the phase diagram of Figure 5.10.

The crossover from the dilute to dense regime is accompanied by a qualitative change in the nature of contact forces between grains, measured using the contact

force distribution function $P(f)$. For shear flows in the dilute regime $P(f)$ has a peak at non-zero f, whereas for shear flows in the dense regime there is no peak. This distinctive feature of $P(f)$ has been observed in experiments [93] and accompanies the emergence of force chain networks.

Chapter 6

Modeling of Granular Shear Flow

The nature of the microscopic interaction between grains has important implications for how modeling should be carried out. In the following sections we explore different theories of granular flow. We begin with Kinetic Theory, which rests on the assumption that only binary collisions are relevant, and we see how this assumption limits its applicability. Next we present the Force-Network Model, which makes predictions by using the observed length scale ξ and other properties of the force networks that arise in the dense regime. We find that the force network model makes accurate predictions in both the dilute and dense regimes. Finally, we end with STZ theory, which models the dense regime by assuming certain properties of the non-affine deformation that occurs in correlated clusters of grains.

6.1 Kinetic Theory

Kinetic theory has found tremendous success in describing the non-equilibrium properties of thermal gases and liquids [101, 102]. Over the past twenty-five years, a great deal of research has been devoted towards generalizing the constructs of kinetic theory to incorporate granular flows, where energy is dissipated during interactions between grains [28, 29]. In this section we will explore the predictions of kinetic theory for granular flows.

The kinetic theory description of granular shear flows consisting of perfectly rigid grains is based on the Boltzmann-Enskog kinetic equation for hard-sphere interactions [103, 104, 105, 106, 107]. This is a non-linear equation for the one-particle distribution function, which gives the probability to find a particle with a certain position and velocity. Derivations of this equation require two hypotheses: the binary collision assumption and the molecular chaos assumption.

The *binary collision assumption* stipulates that the only relevant interactions are collisions between pairs of grains. It must be made at a very early stage in the derivation of the pseudo-Liouville formalism, which forms the basis for kinetic theory of hard spheres [108]. The binary collision assumption implies that momentum transport is entirely carried out by collisions between pairs of grains:

it therefore sets a microscopic expression for the collisional stress that can be directly computed in numerical simulations, without any further assumption.

The *molecular chaos assumption* stipulates that the velocity dependence of the two particle distribution function is determined simply by two factors of the one particle distribution function. This is equivalent to the statement that there are no pre-collisional velocity correlations in binary collisions between perfectly rigid grains. This assumption is made after the binary collision assumption and offers a means to approximate the collisional transport of momentum.

We begin by presenting an overview of the derivation of the momentum balance equation using kinetic theory, which sets the form of the collisional stress tensor and can be carried out by with only the binary collision assumption. The relevance of the binary collision assumption can be tested using measures of the stress tensor and, not surprisingly, breaks down when ξ becomes large. We then explore the kinetic theory prediction for the collisional stress tensor and how it depends on the assumption of molecular chaos.

6.1.1 Derivation of the Collisional Stress Tensor via the Binary Collision Assumption

Kinetic theory aims to describe macroscopic properties based on the interactions between pairs of grains. This requires a specification of the interaction

potentials and, most importantly, the mechanism for energy dissipation. The dissipation mechanism that has been most thoroughly studied is instantaneous collisions with a constant restitution coefficient– this is often called hard-sphere kinetic theory [108, 109] . In order to make progress using hard-sphere kinetic theory, it is necessary to *start* by postulating that only binary collisions occur [108, 110]. This yields a collision rule that relates the initial velocities of two interacting grains $\{\mathbf{v}'^i, \mathbf{v}'^j\}$ to their final velocities $\{\mathbf{v}^i, \mathbf{v}^j\}$:

$$(\mathbf{v}^j - \mathbf{v}^i) \cdot \hat{\boldsymbol{\sigma}}^{ij} = -e(\mathbf{v}'^j - \mathbf{v}'^i) \cdot \hat{\boldsymbol{\sigma}}^{ij}. \tag{6.1}$$

The normal coefficient of restitution e that appears in this equation regulates the amount of energy dissipation: for $e = 1$ the system is elastic and no energy is dissipated; as e is reduced to zero the energy dissipation scales like $1 - e^2$.

Although there are notable exceptions [107], most hard-sphere kinetic theories of granular media focus on frictionless grains and therefore Equation (6.1) encodes the only possible interaction between grains. Here we will focus on the frictionless kinetic theories, which have received the most formal derivations. Our results, especially regarding the range of applicability of kinetic theories, will not depend sensitively on the frictional properties of the grains.

Kinetic theory relies on the binary collision assumption and is therefore expected to break down as the density of the flow increases and long-lasting contacts arise [30, 31, 32, 33]. Quantitative bounds over which the binary collision assumption holds for systems of perfectly rigid grains have only begun to materialize [78, 83, 79]. The CD algorithm that we use to simulate granular flows is well-suited for testing the relevance of the binary collision assumption and bounding the dilute regime. Like hard-sphere kinetic theory, the CD algorithm for frictionless grains employs a normal coefficient of restitution. However, the CD algorithm does not assume that only binary collisions occur.

On the contrary, we observe that multi-grain correlated contacts do occur. This is evident in the force correlation measurements of Chapter 5 where we identified a growing correlation length ξ. This length-scale should be related to the breakdown of the binary collision assumption since it implies that grain forces are correlated over large distances and do not just depend on nearest neighbors. To see how this comes about, it is useful to make measurements of the static stress tensor.

The static stress tensor in Equation (2.8) encodes contributions to the stress arising from contact forces between grains. In the case that only binary collisions are considered, the value of the static stress tensor is determined by Equation (2.8) using the binary force from Equation (5.4).

This yields the "collisional" stress tensor

$$\Sigma_{\alpha\beta}^{\mathrm{bc}} = \frac{1}{2} \sum_{\{i,j\}=0}^{c} \hat{\sigma}_{\alpha}^{ij} \hat{\sigma}_{\beta}^{ij} \sigma^{ij} F_{\mathrm{bc}}^{ij}, \tag{6.2}$$

which is the stress tensor that all hard-sphere kinetic theories attempt to model [83].

If all interactions occur through binary collisions between grains, the collisional stress and the static stress will be identical. However, in the case that networks of contacting grains form, the average contact force between any two grains will be greater than what is expected from considering only binary collisions– this is because the presence of additional contacts will require a larger force to prevent penetration. In this case, the static stress tensor will be larger than the collisional stress tensor and kinetic theory will not be applicable.

Comparing the static and collisional stress tensors in Equations (2.8) and (6.2) provides an opportunity to test the basic assumption of binary collisions and thereby determine when kinetic theory can be applied to hard-sphere granular flows. In Figures 6.1, 6.2 and 6.3 we present measurements of the static and collisional stress tensor for a wide range of restitution and packing. The stress tensors are reported in terms of the pressure p and shear stress s, related to the

stress tensors by

$$\{p^{\mathrm{s}}, p^{\mathrm{bc}}\} = \{\frac{1}{2}(\Sigma^{\mathrm{s}}_{11} + \Sigma^{\mathrm{s}}_{22}), \frac{1}{2}(\Sigma^{\mathrm{bc}}_{11} + \Sigma^{\mathrm{bc}}_{22})\}, \tag{6.3}$$

$$\{s^{\mathrm{s}}, s^{\mathrm{bc}}\} = \{\Sigma^{\mathrm{s}}_{12}, \Sigma^{\mathrm{bc}}_{12}\} = \{\Sigma^{\mathrm{s}}_{21}, \Sigma^{\mathrm{bc}}_{21}\}. \tag{6.4}$$

In the data of Figures 6.1, 6.2 and 6.3 both the collisional and static values of the pressure and shear stress are normalized by common factors that are explained later. For now, it is only important to notice that there is a regime where the binary collision assumption holds and the normalized stress tensors are equal. The bounds of this regime depend on the value of both the restitution coefficient and the packing fraction. The data supports a conclusion that the dilute regime is approached as density is reduced or restitution is increased.

Instead of characterizing the dilute regime in terms of restitution and packing, it is advantageous to connect it to the length-scale ξ. In Figures 6.1, 6.2 and 6.3 we have colored in the data points where the length scale from Figure 5.3 satisfies the condition $\xi/\xi_{\mathrm{el}} > 1.25$. For all of our data, this simple condition on ξ nicely characterizes the dilute regime– if $\xi/\xi_{\mathrm{el}} < 1.25$ then the static stress tensor is approximately equal to the collisional stress tensor and the predictions of kinetic theory are relevant; if $\xi/\xi_{\mathrm{el}} > 1.25$ then interactions between networks of grains begin to become important and kinetic theory modeling is not useful.

The critical value of $\xi/\xi_{\rm el} = 1.25$ is also where we measured that the contact force distribution $P(f)$ loses its peak (see Figure 5.8) and provides a quantitative bound for the dilute regime as shown in Figure 5.10. Studying the discrepancy between the collisional and static values of the stress tensor reveals the breakdown of the binary collision assumption and shows that it is related to the growth of ξ, as expected.

In addition to the discrepancy between the collisional and static stress tensors in the dense regime, another interesting features of the data in Figures 6.1, 6.2 and 6.3 is the large density behavior of the collisional stress. For large packing, $s^{\rm bc}$ actually begins to decrease. This is expected since, as the density is increased towards the jamming threshold where all velocities become zero, the collisional stress tensor will reduce to zero because it is proportional to the average relative velocity of contacting grains. It is also interesting to note that the collisional shear stress begins to decrease before the collisional pressure. This is related to the anisotropy of sheared granular materials and the fact that the correlation length depends on the orientation of pairs of grains.

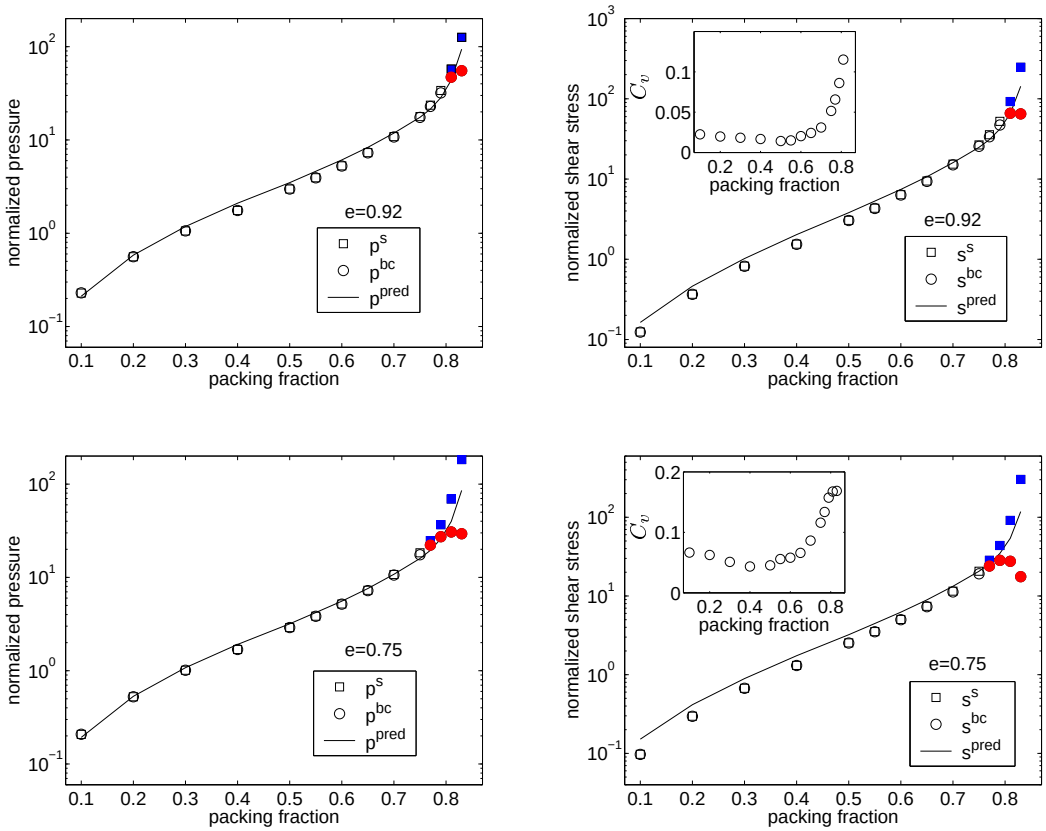

Figure 6.1: Main Figures: Normalized values of the pressure (left) and shear stress (right) for various restitution coefficients $e - 0.92$ and $e = 0.75$. The pressures are normalized by p^0 from Equation (6.9) and the shear stresses are normalized by $\dot{\gamma}\eta^0$ from Equation (6.10) . The dilute regime is characterized by the range of restitution and packing where the static and collisional values are equal. Filled data points correspond to values of restitution and packing where $\xi/\xi_{\rm el} > 1.25$– this provides a simple quantitative condition for the boundary of the dilute regime. Kinetic theory is expected to apply in the dilute regime and the prediction for the pressure is good for all e. The prediction for the shear stress overestimates the actual value, due to positive velocity correlations. **Insets:** Pre-collisional velocity correlations as a function of packing fraction (defined in Equation (6.11).

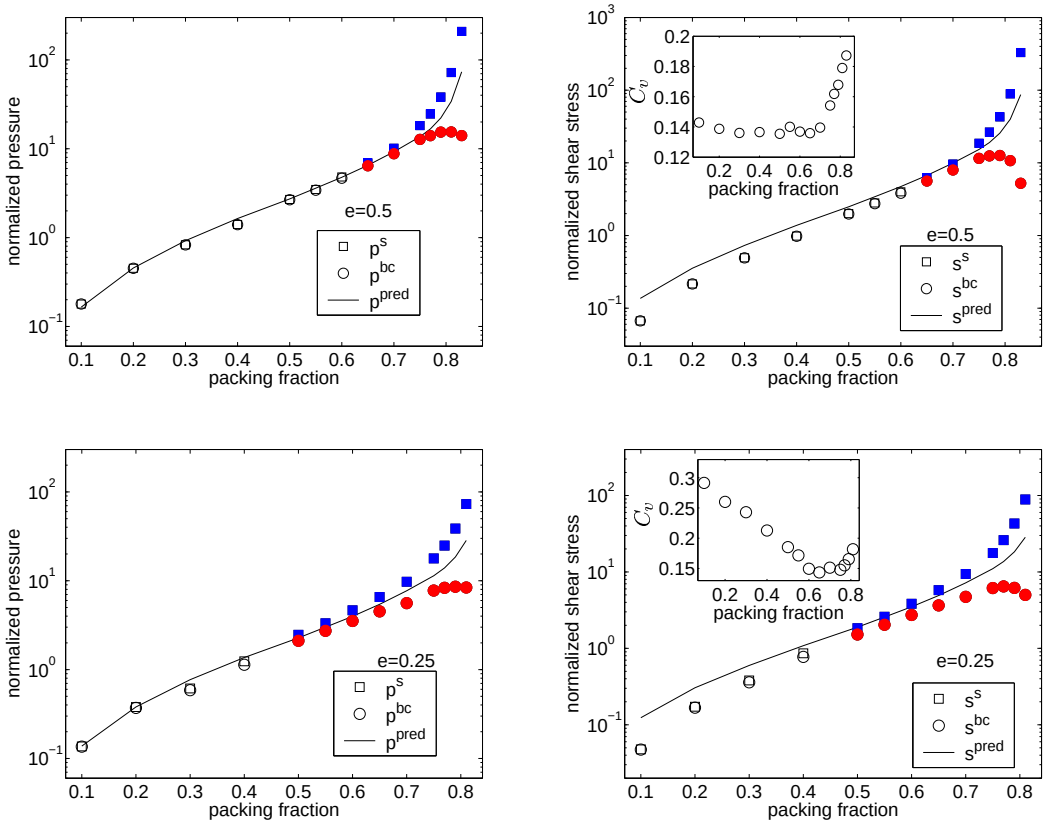

Figure 6.2: Same as Figure 6.1, but for $e = 0.5$ and $e = 0.25$.

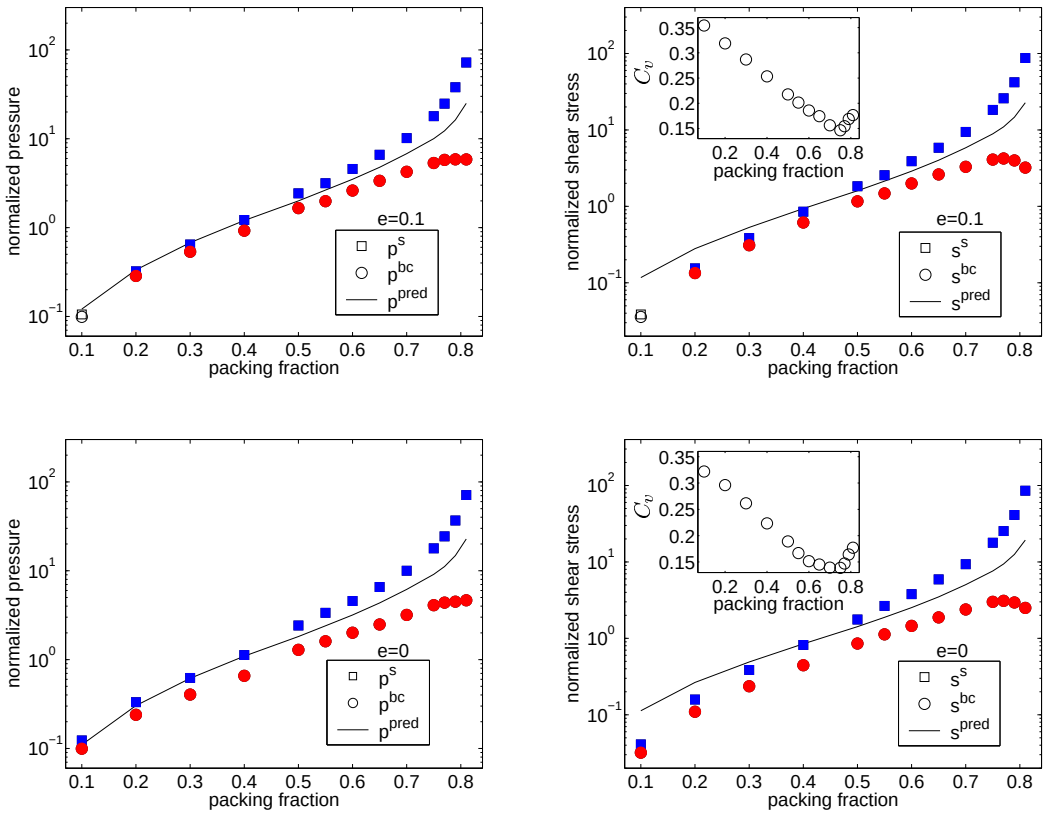

Figure 6.3: Same as Figures 6.1 and 6.2, but for $e = 0.1$ and $e = 0$.

6.1.2 Predictions of Kinetic Theory and the Molecular Chaos Assumption

We will now focus on the predictions of kinetic theory in the dilute regime where $\xi/\xi_{\rm el} < 1.25$ and the binary collision assumption holds. In this regime we will test the predictions of hard-sphere kinetic theory for both the pressure and shear stress. These predictions have been recently obtained [103, 104, 105] using the Chapman-Enskog expansion to solve the Enskog equation. The Enskog equation determines the time dependence of the one-particle probability distribution function (pdf) in terms of collision events between grains. In the hard-sphere approximation the collision events only consist of binary interactions and the time dependence of the one-particle pdf can therefore be expressed in terms of just the two-particle pdf. For hard-sphere granular materials, Enskog's equation reads

$$(\partial_t + \mathbf{v_1}\cdot\nabla_{\mathbf{1}})f^{(1)}(\mathbf{r_1},\mathbf{v_1},t) = J_E[\mathbf{r_1},\mathbf{v_1}], \tag{6.5}$$

with J_E given by

$$\begin{aligned} J_E[\mathbf{r_1},\mathbf{v_1}] &= \sigma\int d\mathbf{v_2}\int d\hat{\boldsymbol{\sigma}}\,\Theta(\hat{\boldsymbol{\sigma}}\cdot\mathbf{g})(\hat{\boldsymbol{\sigma}}\cdot\mathbf{g}) \\ &\times [e^{-2}f^{(2)}(\mathbf{r_1},\mathbf{r_1}-\boldsymbol{\sigma},\mathbf{v_1'},\mathbf{v_2'},t) - f^{(2)}(\mathbf{r_1},\mathbf{r_1}+\boldsymbol{\sigma},\mathbf{v_1},\mathbf{v_2},t)]. \end{aligned} \tag{6.6}$$

In these equations, the time dependence of the one-particle pdf $f^{(1)}$ is related to a collisional term that quantifies the probability to gain and lose contributions, at a certain velocity $\mathbf{v_1}$, due to binary collisions. Binary collisions occur according to Equation (6.1) and primed velocities represent pre-collisional values. Θ is the step function and $\mathbf{g} = \mathbf{v_1} - \mathbf{v_2}$. For hard sphere granular flows, this form for the Enskog equation can be formally derived, beginning with the binary collision assumption and a derivation of the pseudo-Liouville equation [108, 110].

A prediction for the collisional stress tensor is obtained by multiplying both sides of Equation (6.5) by $m\mathbf{v_1}$, where m is the particle mass, and integrating over $\mathbf{v_1}$. This yields the transport equation for momentum density [103], from which the stress tensor can be read off as

$$\begin{aligned} \Sigma_{\alpha\beta}^{\text{pred}} &= \frac{1+e}{4} m\sigma \int d\mathbf{v_1} \int d\mathbf{v_2} \int d\hat{\boldsymbol{\sigma}} \Theta(\hat{\boldsymbol{\sigma}} \cdot \mathbf{g})(\hat{\boldsymbol{\sigma}} \cdot \mathbf{g})^2 \sigma_\alpha \sigma_\beta \\ &\times \int_0^1 d\lambda f^{(2)} \left[\mathbf{r} - (1-\lambda)\boldsymbol{\sigma}, \mathbf{r} + \lambda\boldsymbol{\sigma}, \mathbf{v_1}, \mathbf{v_2}, t\right]. \end{aligned} \tag{6.7}$$

This is the hard-sphere kinetic theory prediction for the collisional stress and it depends on the two-particle pdf $f^{(2)}$, since it is related to the force that arises from binary collisions between grains.

In order to determine the stress tensor and solve the Enskog equation, it is necessary to express $f^{(2)}$ in terms of $f^{(1)}$. This is done by assuming that there are

no velocity correlations between grains that are about to collide, which yields

$$f^{[2]}(\mathbf{r_1}, \mathbf{r_2}, \mathbf{v_1}, \mathbf{v_2}, t) = \chi(\mathbf{r_1}, \mathbf{r_2}) f(\mathbf{r_1}, \mathbf{v_1}, t) f(\mathbf{r_2}, \mathbf{v_2}, t) \tag{6.8}$$

and reduces the Enskog Equation (6.5) to a non-linear differential equation for the one-particle pdf. The function χ is interpreted as the equilibrium correlation function at contact and depends on the local value of the density.

Once the Enskog equation has been expressed in terms of only the one-particle pdf, it can be solved using the Chapman-Enskog expansion [101, 102], which expands $f^{(1)}$ and J_E in gradients of the mass density, momentum density, and energy density. This process has been carried out for granular shear flows to first order in the gradients in Refs. [103, 104, 105]. When $f^{(1)}$ is determined through this expansion a prediction for the collisional stress tensor, correct through first order in the gradients, can be made by combining Equations (6.8) and (6.7). The results of this calculation for two-dimensional shear flows is [105]

$$\frac{p^{\text{pred}}}{p^0} = (1+e)\chi\nu, \tag{6.9}$$

$$\frac{s^{\text{pred}}}{\dot{\gamma}\eta^0} = \frac{4\nu}{\pi}\left(\frac{4}{5-e} + \nu\chi(1+e)f(e)\right), \tag{6.10}$$

$$f(e) = \frac{3e-1}{5-e} + \left(1 - \frac{(1-e)(1-2e^2)}{81-17e+30e^2(1-e)}\right).$$

These predictions for the normalized shear stress and pressure depend only on the restitution e, the packing fraction ν, and the pair correlation function at contact χ. The normalizing factors are given by $p^0 = nmT/2$ and $\eta^0 = m/\sigma\sqrt{T/2\pi}$, where m is the grain mass, σ the grain diameter, T the granular temperature, and n the number density. All of these variables can be measured directly from simulations and we can thereby test the predictions of hard-sphere kinetic theory without using any fitting parameters. We use the average value of grain mass and diameter for m and σ, and determine χ by tracking the number of collisions that occur per second (which we denote by ω) in equilibrium simulations where $e = 1$ and $\dot{\gamma} = 0$. Enskog theory relates χ to ω through the equation $\omega = \sqrt{2\pi\delta T}\chi n\sigma$. This method for measuring χ has been used in other recent studies [111].

We plot the normalized predictions from Equations (6.9) and (6.10) in Figures 6.1, 6.2 and 6.3, where they are compared to data for the stress tensor. Since hard-sphere kinetic theory makes the binary collision assumption, these predictions are only applicable to the dilute regime, which corresponds to the open symbols where $\xi/\xi_{\rm el} < 1.25$. We immediately notice that the prediction for the pressure matches the measured pressure in all of the dilute systems we have investigated. Considering that there are no adjustable parameters, this is a tremendous success for kinetic theory.

The prediction for the shear stress also matches the data in the dilute regime quite well for large restitution. However, as the restitution becomes smaller, the prediction for the shear stress begins to overestimate the measured value. This overestimation is due to pre-collisional velocity correlations, a mechanism that has been investigated in previous studies [112]. Because Equation (6.8) assumes that there are no pre-collisional velocity correlations, if these correlations exist then the average momentum transfered in each equation will change. If the pre-collisional normal velocities of two grains tend to be aligned (anti-aligned) then the average momentum transfered will decrease (increase), causing the kinetic theory prediction to overestimate (underestimate) the measured values.

In the insets of Figures 6.1, 6.2 and 6.3, we display measurements of the pre-collisional velocity correlations C_v defined as

$$C_v = \langle \left(\mathbf{v}'^i \cdot \hat{\boldsymbol{\sigma}}^{ij} \right) \left(\mathbf{v}'^j \cdot \hat{\boldsymbol{\sigma}}^{ij} \right) \rangle / T, \tag{6.11}$$

which are normalized by the granular temperature. This definition yields a positive value when pre-collisional grain velocities tend to be aligned, and for all restitution coefficients we observe that the correlations are positive. In addition, the magnitude of the discrepancy between measured and predicted shear stress is roughly proportional to the size of the velocity correlations. These observations

further supports the conclusion that the errors in the kinetic theory prediction are due to the pre-collisional velocity correlations. It is, however, surprising that the correlations affect the predicted value of the shear stress, but not the predicted value of the pressure.

In summary, kinetic theory makes predictions based on the binary collision assumption and the molecular chaos assumption. The stress tensor predicted by hard-sphere kinetic theory is extremely accurate in the dilute regime and at high restitution coefficients. As the restitution coefficient is reduced, the predictions for the shear stress begin to fail due to the molecular chaos assumption in Equation (6.8). Additionally, as ξ/ξ_{el} becomes larger than 1.25 and the granular flow approaches the dense regime, hard-sphere kinetic theory is unable to make predictions since the binary collision assumption is no longer valid. These observations demonstrate that the calculations that have been made [103, 104, 105] using the present assumptions of hard-sphere kinetic theory are accurate, and that it is the nature of the fundamental assumptions that are causing kinetic theory to fail and need to be addressed.

Recent research [108, 113] has concentrated on refining the molecular chaos assumption of Equation (6.8) within the constructs of kinetic theory to account for velocity correlations, which have been measured extensively [112, 114, 115, 116, 117]. These studies are aimed at making better predictions in the dilute regime

and our research shows that this is the correct approach to take. However, in the dense regime, where ξ becomes large and networks of interacting grains become important, a kinetic theory approach is no longer relevant due to the breakdown of its most fundamental assumption. In this case, new theories must be developed that take force correlation and collective motion into account.

6.2 Force-Network Model

We have observed that the correlations which exist for $\xi/\xi_{\text{el}} > 1.25$ invalidate the use of the binary collision assumption and thereby seriously reduce the regime of applicability of kinetic theory. The mechanism that effects the predictions for the stress tensor is forces being propagated through networks that are larger than two grains. This mechanism has been theoretically investigated previously [118, 119, 120, 121, 122, 123, 124], but the analysis has always assumed an infinite force-network. In this section we will introduce a way to incorporate force propagation through finite sized networks into constitutive models for the stress tensor.

Dense inertial flows, which are not quasi-static and can not be modeled by assuming binary collisions between grains, have recently become an active field of research [25, 26, 27]. Networks of force chains become prevalent in this regime and their effects must be included in any successful model of quantities related

to contact forces. In the hard-sphere limit, forces are propagated instantaneously through contact networks and the value of the contact force between any pair of grains depends on both the relative velocity of the pair and the values of the other contact forces in the network, even those a long distance away. This force transfer becomes the dominant contribution to the contact forces in the dense inertial regime and is modeled below.

Due to the presence of force chain networks, the value of the static stress tensor becomes larger than what is calculated based on binary collisions between grains. By considering simple properties of the force networks, it is possible to derive mean-field constitutive relations for the static stress tensor that hold for all ξ, but are most relevant in the dense regime where $\xi/\xi_{\text{el}} > 1$.

Equation (2.8) for the static stress tensor and Equation (6.2) for the collisional stress are identical in form, but use different values for the contact force. The static stress tensor is proportional to the total contact force F experienced by a pair of contacting grains while the collisional stress tensor is proportional to the collisional force F_{bc}. The difference in the values of the stress tensors is therefore related to these forces and the fact that $F \geq F_{\text{bc}}$ in the dense inertial regime. To derive a constitutive relation for the static stress tensor we will determine, on average, how the contact forces depend on properties of the force network.

When force networks have formed, the contact force between a pair of grains is larger than what is expected from considering only binary collisions. This is because other grains in the network provide an effective pressure that forces the pair together and increases the contact force. Mathematically, the contact force F^{IJ} between grains I and J is equal to the sum of a collisional term, plus effects from the network:

$$F^{IJ} = F^{IJ}_{\rm bc} + \sum_{\ell=1}^{\ell_{\rm max}} \mathcal{F}^{IJ}_{\ell}. \tag{6.12}$$

In this equation, the first term is the collisional force, defined in Equation (5.4), which is determined locally from the relative normal velocities of the contacting grains I and J. It is the force necessary to prevent penetration between a pair of binary colliding grains in the absence of force networks. Once networks form this non-penetration force will be larger, due to the influence of the other grains in the network. This is encoded in the second term and arises from forces propagating through paths in the force chain network, as pictured in Figure 6.4. We find it convenient to split this effect into terms $\mathcal{F}^{IJ}_{\ell}$ that represent contributions from different path-lengths ℓ. The total additional force needed to prevent penetration between grains I and J is equal to the sum of the contributions $\mathcal{F}^{IJ}_{\ell}$ over all possible path-lengths $\ell < \ell_{\rm max}$ in the force network.

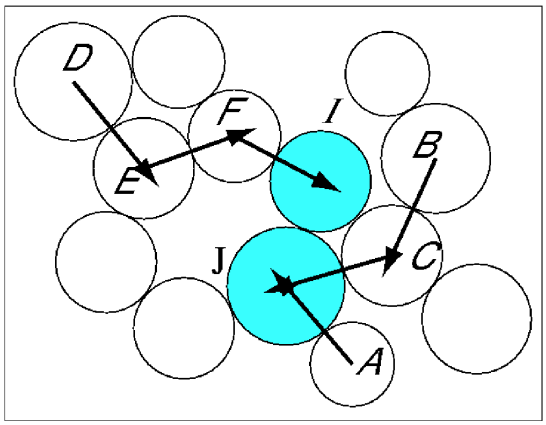

Figure 6.4: A network of contacting grains. The contact force between the shaded grains I and J is determined by the local collisional force $F_{\rm bc}^{IJ}$, plus non-local contributions from forces propagating through the network. It is convenient to organize these non-local effects into contributions from different path-lengths. On the top left is a path of size three where the local contact force between grains D and E is transferred through the network to grain I. On the top right is a path of size two, and on the bottom right is a path of size one.

Figure 6.4 illustrates how forces propagate and defines the notion of path-length. For example, because grain D is in contact with grain E, this increases the force between grains E and F, which increases the force between grains F and I, which has the net effect of increasing the contact force between grains I and J. We will call this a path of length three ($\ell = 3$) since the local force $F_{\rm bc}^{DE}$ must propagate through three grains to influence the contact between I and J.

The net effect of forces propagating through different path-lengths can be calculated explicitly. We assume that the speed of wave propagation through the network is infinitely fast, which is natural in the perfectly rigid grain limit. Physically, for grains with a large but finite stiffness, this corresponds to disturbances propagating through the network much faster than contacts are created or destroyed. We will begin by considering a path of length $\ell = 1$, as illustrated in Figure 6.4: because grain A is in contact with grain J, the local contact force $F_{\rm bc}^{AJ}$ increases the value of F^{IJ} by an amount equal to $F_{\rm bc}^{AJ}$ multiplied by the cosine of the angle between the unit vectors connecting grains $\{A, J\}$ and $\{I, J\}$. If we assume that grain I has z_I contacts labeled by m and grain J has z_J contacts labeled by n, then the effect of all paths of length one is to increase F^{IJ} in Equation (6.12) by an amount

$$\mathcal{F}_1^{IJ} = \sum_{m=1;m\neq J}^{z_I} \hat{\boldsymbol{\sigma}}^{mI} \cdot \hat{\boldsymbol{\sigma}}^{IJ} F_{\rm bc}^{mI} + \sum_{n=1;n\neq I}^{z_J} \hat{\boldsymbol{\sigma}}^{nJ} \cdot \hat{\boldsymbol{\sigma}}^{IJ} F_{\rm bc}^{nJ}, \tag{6.13}$$

where $\hat{\boldsymbol{\sigma}}^{\boldsymbol{ab}}$ is the unit vector connecting the center of grains a and b. This expression includes all of the effects from paths of length one on each of the contacting grains I and J.

In an analogous manner, the path from grain B to C to J in Figure 6.4 comprises a path of length two ($p = 2$), which increases the value of F^{IJ} due to the local force between B and C. The total additional force between grains I and J arising from paths of length two is given by

$$\begin{aligned} \mathcal{F}_2^{IJ} &= \sum_{m=1;m\neq J}^{z_I} \hat{\boldsymbol{\sigma}}^{mI} \cdot \hat{\boldsymbol{\sigma}}^{IJ} \sum_{m_2=1;m_2\neq m}^{z_m} \hat{\boldsymbol{\sigma}}^{m_2 m} \cdot \hat{\boldsymbol{\sigma}}^{mI} F_{\mathrm{bc}}^{m_2 m} \\ &+ \sum_{n=1;n\neq I}^{z_J} \hat{\boldsymbol{\sigma}}^{nJ} \cdot \hat{\boldsymbol{\sigma}}^{IJ} \sum_{n_2=1;n_2\neq n}^{z_n} \hat{\boldsymbol{\sigma}}^{n_2 n} \cdot \hat{\boldsymbol{\sigma}}^{nJ} F_{\mathrm{bc}}^{n_2 n}, \end{aligned} \tag{6.14}$$

where once again grain I has z_I contacts labeled by m and grain J has z_J contacts labeled by n. To calculate the effect of paths of length two, we also take into account the z_m contacts of grain m, labeled by m_2, and the z_n contacts of grain n, labeled by n_2.

The contribution to F^{IJ} from an arbitrary path-length ℓ can be determined by continuing the above arguments, and the expressions become increasingly complex. They depend on the coordination number z and are also sensitive to the geometric arrangement of the force networks. One important constraint arises as z becomes large. If we consider the total force T^{IJ} that an arbitrary pair of con-

tacting grains I and J contribute to the network, this must always be less than the actual collisional force $F_{\rm bc}^{IJ}$. This is because a single contact can not push harder than the value of its collisional force allows. This leads to the constraint equation

$$\begin{aligned} T^{IJ} &\equiv F_{\rm bc}^{IJ}\left(\sum_{m=1;m\neq J}^{z_I}\hat{\boldsymbol{\sigma}}^{mI}\cdot\hat{\boldsymbol{\sigma}}^{IJ}+\sum_{n=1;n\neq I}^{z_J}\hat{\boldsymbol{\sigma}}^{nJ}\cdot\hat{\boldsymbol{\sigma}}^{IJ}\right) \\ &\leq F_{\rm bc}^{IJ}. \end{aligned} \tag{6.15}$$

The above considerations allow for a determination of $\mathcal{F}_\ell^{IJ}$. It only remains to estimate $\ell_{\rm max}$, which is the maximum path-length. In what follows we will assume that no loops arise in the force chain networks. This allows us to connect the maximum size of the force chains with the correlation length we have measured previously: $\ell_{\rm max}=\xi/\xi_{\rm el}-1$. Loops would complicate the analysis since a single contact force could propagate endlessly around a closed loop and there would be no maximum path-length in the force networks. For a realistic granular material, the assumption that no loops arise should be fairly accurate. Because the propagation of forces through links in a force chain is always proportional to the dot product of $\hat{\boldsymbol{\sigma}}$'s, a force propagating around a closed loop would quickly become much smaller than the other forces in the network and would not appreciably contribute to Equation (6.12).

Given the above analysis, it is possible to completely determine the stress tensor based on properties of the force network and the collisional stresses. This is carried out in the next subsection and the predictions are tested in the following subsection. The main approximation of the model is that loops in the force network are not relevant above a size $\xi/\xi_{\rm el} - 1$, which is the upper cut-off for force network propagation.

6.2.1 Calculating the stress tensor

To make calculations using the force network model, it is useful to rewrite the equations for $\mathcal{F}_\ell^{IJ}$ in terms of integrals instead of sums. We will only present the analysis for two-dimensional systems, although it can easily be generalized to higher dimension. If we consider the average contact force between two grains contacting at an angle θ, denoted $F(\theta)$, then Equation (6.12) can be generalized to

$$F(\theta) = F_{\rm bc}(\theta) + \sum_{\ell=1}^{\xi/\xi_{\rm el}-1} \mathcal{F}_\ell(\theta). \tag{6.16}$$

This equates the average force between grains contacting at angle θ to the average collisional force at that angle, plus effects from the network. Then, generalizing

Equations (6.13) and (6.14) to arbitrary path-length ℓ gives

$$\mathcal{F}_\ell(\theta_0) = \prod_{i=1}^{\ell}(z-1)\int_{\theta_{i-1}-2\pi/3}^{\theta_{i-1}+2\pi/3} d\theta_i \cos(\theta_i - \theta_{i-1}) P_C(\theta_i - \theta_{i-1}) C(\theta_i) F_{\rm bc}(\theta_\ell). \quad (6.17)$$

In this equation, each sum from the previous expressions has been replaced by an integral over θ_i, which is the angular orientation of each link in the chain, and each integral also contains a cosine that replaces the dot product. Note that the bounds of each integral are arranged so that the grain at link i is not permitted to overlap the grain at link $i-1$. In order to properly characterize the probability to have a contact at θ_i, we also introduce the probability functions C and P_C. The function $C(\theta_i)$ gives the probability to have a single contact at angle θ_i [84, 85, 86, 87, 88]. In the case that there are two (or more) contacts on a single grain, which is necessary to form a chain, this probability must be modified [89]. The function $C(\theta_i)P_C(\theta_i - \theta_{i-1})$ gives the conditional probability to have a contact at θ_i, provided that there already is a contact at θ_{i-1}, and it is present in each integral. Finally, the function $F_{\rm bc}(\theta_n)$ provides the collisional force at the end of the path and a factor of $(z-1)$, where z is the average coordination number, is included for each link.

A slightly more useful form of Equation (6.17) can be obtained by changing the integration variables to $x_i = \theta_i - \theta_{i-1}$. This results in the expression

$$\mathcal{F}_\ell(\theta) = \prod_{i=1}^{\ell}(z-1)\int_{-2\pi/3}^{2\pi/3} dx_i \cos(x_i)P(x_i)C(\theta + \sum_{j=1}^{i} x_j)F_{\mathrm{bc}}(\theta + \sum_{j=1}^{p} x_j), \quad (6.18)$$

which encodes the average effect of all forces that propagate through a path of length ℓ in the force-network on a contact with orientation θ. In addition to this propagation based on the cosine of the angle between subsequent contacts, we must also incorporate the constraint from Equation (6.15). This constraint can be generalized as

$$T(\theta) = F_{\mathrm{bc}}(\theta)(z-1)\int_{-2\pi/3}^{2\pi/3} dx P_C(x)\cos(x)C(\theta + x) \leq F_{\mathrm{bc}}(\theta), \quad (6.19)$$

and restricts a single contact at angle θ to contribute at most a force of $F_{\mathrm{bc}}(\theta)$ to the network.

Equations (6.18) and (6.19), combined with the basic force network Equation (6.16), comprise the integral form of the force network model. In order to carry out the integrations, it is necessary to know the functional form of $C(\theta)$ and $F_{\mathrm{bc}}(\theta)$. These functions are π-periodic and can be written as Fourier Series, keeping only terms that are also π-periodic. Previous research on the contact probability [84, 85, 86, 87, 88] has shown that $C(\theta)$ is well approximated by keep-

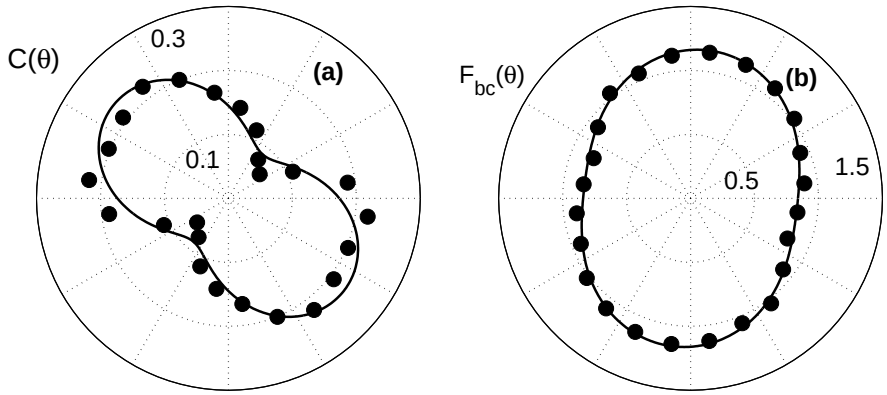

Figure 6.5: Polar plots of measurements (data points) and fits (lines) of **(a)** the contact probability distribution $C(\theta)$ and **(b)** the collisional force distribution $F_{\rm bc}(\theta)/\langle F_{\rm bc}\rangle$ for a granular material with $e = 0$ and $\nu = 0.79$. The lines are fit to Equations (6.21) and the values of the Fourier components are plotted in Figure 6.6.

ing only the lowest Fourier terms. We find that $F_{\rm bc}(\theta)$ has the same property. We will therefore approximate

$$C(\theta) = \frac{1}{2\pi}(1 + a_c \sin 2\theta + a_c' \cos 2\theta), \tag{6.20}$$

$$F_{\rm bc}(\theta) = \langle F_{\rm bc}\rangle(1 + a_f \sin 2\theta + a_f' \cos 2\theta). \tag{6.21}$$

In Figure 6.5 we plot data of these functions for a granular material with $e = 0$ and $\nu = 0.79$, along with a fit to the above equations. The fit is constructed by computing the fabric tensor $\phi_{\alpha\beta} = \langle \hat{\sigma}_\alpha \hat{\sigma}_\beta \rangle$ and force-fabric tensor $\chi^{(n)}_{\alpha\beta} = 1/\langle F_{\rm bc}\rangle \langle F_{\rm bc} \hat{\sigma}_\alpha \hat{\sigma}_\beta \rangle$, as in Ref. [87]. We see from the plots that this first-order approximation for the contact probability and collisional force is quite good.

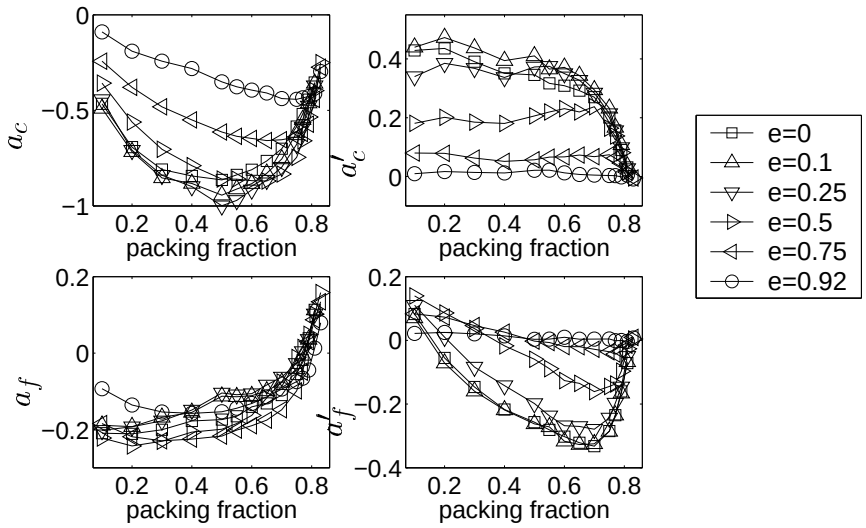

Figure 6.6: Values of the Fourier components from Equation (6.21).

We have measured $C(\theta)$ and $F_{\rm bc}(\theta)$ for a wide range of restitution coefficients and packing fractions. In Figure 6.6 we plot the value of the Fourier components from Equations (6.20) and (6.21), which characterize the functional form in all cases. These plots reveal that the anisotropy in both the contact probability and collisional force depend sensitively on the value of the packing fraction and restitution coefficient. The size of the components is always of order 10^{-1} whereas the magnitude of the next order coefficients in the Fourier Series is less than 10^{-2}. This is what allows us to truncate the series in Equations (6.20) and (6.21) at first order and still get good agreement to the actual data, as in Figure 6.5.

Now that we have a functional form for $C(\theta)$ and $F_{\rm bc}(\theta)$, we can solve for $\mathcal{F}_\ell(\theta)$ to first order in the Fourier components $\{a_c, a_c', a_f, a_f'\}$. This gives

$$\mathcal{F}_\ell(\theta) = \langle F_{\rm bc}\rangle (z-1)^\ell \Big(\Phi^\ell + \Psi^\ell (a_f \sin 2\theta + a_f' \cos 2\theta) + \sum_{i=1}^{\ell} \Psi^i \Phi^{\ell-i} (a_c \sin 2\theta + a_c' \cos 2\theta)\Big), \tag{6.22}$$

where Φ and Ψ are variables that depend on the geometry of the force networks and are expressible as

$$\{\Phi, \Psi\} = \int_{-2\pi/3}^{2\pi/3} dx P_C(x) \cos(x) \{1, \cos(2x)\}. \tag{6.23}$$

We can also solve for the constraint in Equation (6.19). To lowest order in the Fourier components, the constraint equation gives

$$\frac{T(\theta)}{\langle F_{\rm bc}\rangle} = \Phi(z-1) \leq 1. \tag{6.24}$$

This, combined with Equation (6.22), gives a closed formula for $\mathcal{F}_\ell$:

$$\begin{aligned} \mathcal{F}_\ell(\theta) = \langle F_{\rm bc}\rangle \quad \Big(& \min[\Phi(z-1), 1]^\ell + \Psi^\ell (z-1)^\ell (a_f \sin 2\theta + a_f' \cos 2\theta) \\ + & \sum_{i=1}^{\ell} \Psi^i (z-1)^i \min[\Phi(z-1), 1]^{\ell-i} (a_c \sin 2\theta + a_c' \cos 2\theta) \Big), \end{aligned} \tag{6.25}$$

which is the complete solution to first order in $\{a_c, a_c', a_f, a_f'\}$.

This solution can now be used to arrive at a constitutive relation for the stress tensor. The static stress tensor is given by Equation (2.8), which can be rewritten in two-dimensions as

$$\Sigma^{\rm s}_{\alpha\beta} = \frac{1}{V}\int d\theta C(\theta)\sigma(\theta)F(\theta) \times \begin{pmatrix} \cos^2\theta & \cos\theta\sin\theta \\ \cos\theta\sin\theta & \sin^2\theta \end{pmatrix}, \tag{6.26}$$

where $\sigma(\theta)$ is the average value of the distance between grains at contact for a given angle. In our simulations we observe that $\sigma(\theta)$ has very little dependence on θ (of order less than 10^{-3}) and we will therefore set $\sigma(\theta) = \langle\sigma\rangle$. We can also use this same integral form to determine the collisional stress tensor by replacing $F(\theta)$ with $F_{\rm bc}(\theta)$.

To this point, we have mainly concentrated on the pressure and shear stress to describe the stress tensor. The pressure is given by one-half the trace of Equation (6.26) and the shear stress by either off-diagonal element, but these two quantities do not fully describe the stress tensor. There is a third independent term and, without loss of generality, we will use Σ_{11}. Inserting the solution for $F(\theta)$ from Equations (6.16) and (6.25) into Equation (6.26), we arrive at the following constitutive relations that fully describe the stress tensor:

$$\frac{p^{\rm s} - p^{\rm bc}}{p^{\rm bc}} = \sum_{\ell=1}^{\xi/\xi_{\rm el}-1} \min[\Phi(z-1), 1]^{\ell}, \tag{6.27}$$

$$\frac{s^{\mathrm{s}} - s^{\mathrm{bc}}}{p^{\mathrm{bc}}} = \frac{1}{2}\sum_{\ell=1}^{\xi/\xi_{\mathrm{el}}-1}\Big(a_f\Psi^\ell(z-1)^\ell + a_c\sum_{i=0}^{\ell}\Psi^i(z-1)^i\min[\Phi(z-1),1]^{\ell-i}\Big), \tag{6.28}$$

$$\frac{\Sigma_{11}^{\mathrm{s}} - \Sigma_{11}^{\mathrm{bc}}}{p^{\mathrm{bc}}} = \sum_{\ell=1}^{\xi/\xi_{\mathrm{el}}-1}\Big(\min[\Phi(z-1),1]^\ell + \frac{a_f'}{2}\Psi^\ell(z-1)^\ell + \frac{a_c'}{2}\sum_{i=0}^{\ell}\Psi^i(z-1)^i\min[\Phi(z-1),1]^{\ell-i}\Big) \tag{6.29}$$

These equations relate the static pressure and static shear stress to the collisional values and properties of the force networks.

6.2.2 Testing the predictions

Equations (6.27), (6.28) and (6.29) make predictions for all independent components of the stress tensor. The left hand side of each equation gives the difference between the static and collisional values of stress and is related in each case to certain features of the force networks. These include the anisotropy in the contact probability and collisional force $\{a_c, a_c', a_f, a_f'\}$, the size of the force networks as quantified by the length scale ξ/ξ_{el}, the average coordination number z, and a pair of geometric variables Φ and Ψ that are defined in Equation (6.23) and are related to the distribution of contacts on a single grains. We have measured all of these variables previously except for z, Φ and Ψ.

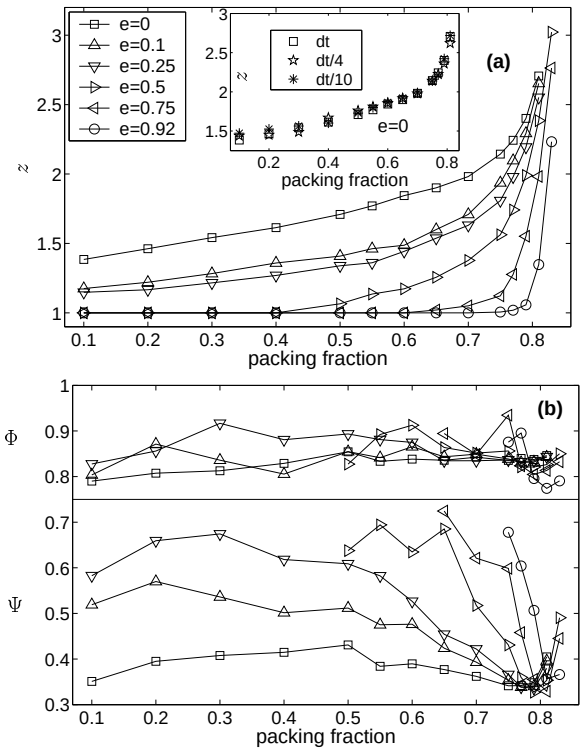

Figure 6.7: **(a)** The coordination number and **(b)** Φ and Ψ for a wide variety of packing fractions and restitution coefficients. The labels in **(b)** are the same as in **(a)**. Although z and Ψ depend sensitively on the value of ν and e, the value of Φ is always approximately 0.83.

In Figure 6.7 we plot the values of z, Φ and Ψ as measured in our simulations. We measure z by averaging over long-lived contacts, defined as pairs of contacting grains that were also contacting in the previous time step. This ensures that only the static backbone of the force network is considered and that transient contacts do not give a coordination number that is artificially high. This measurement of z does not depend on the time step, as is shown in the inset. We also measure Φ and Ψ, according to Equation (6.23), by averaging over the same set of contacts. We observe that $\Psi < \Phi$ for all granular materials we have considered.

We have now measured every variable in the constitutive relations of Equations (6.27), (6.28) and (6.29). We can therefore test the validity of the predictions without using any fitting parameters. Due to the complexity of the equations, it is convenient to plot the right-hand-side of each equation versus the left-hand-side. This is shown in Figure 6.8 using all of the data we have collected. Plotted in this way, the data for each component of the stress tensor collapses onto the line predicted by the force-network model over at least four decades. This collapse is especially striking since the variables in the predictions tend to have a wide variance as a function of restitution coefficient and packing fraction.

The collapse of all of our data onto the curves predicted by the Force-Network model gives assurance that the basic notion of forces propagating through force networks is valid. However, since the simulations presented here occur over a wide

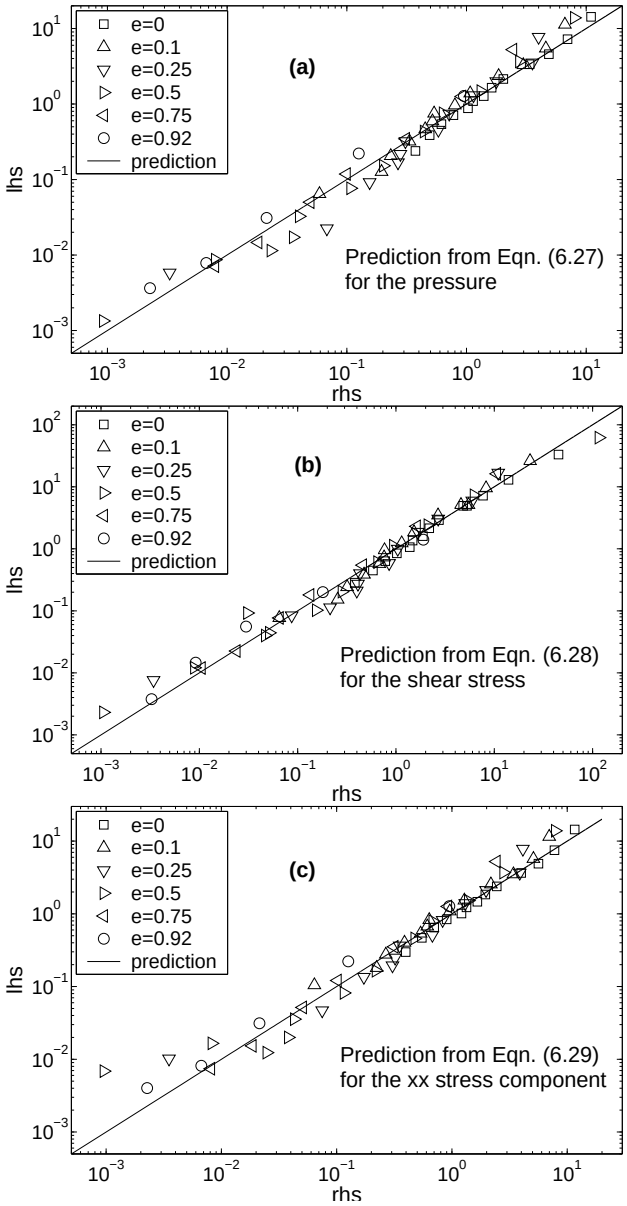

Figure 6.8: Tests of the constitutive relations from the force network model. **(a)** Test of Equation (6.27). The left hand side (lhs) of the equation, $\frac{p^{\mathrm{s}}-p^{\mathrm{bc}}}{p^{\mathrm{bc}}}$, is plotted as a function of the right hand side (rhs). This collapses the data to the line predicted by the model; **(b)** The left hand side of Equation (6.28), $\frac{s^{\mathrm{s}}-s^{\mathrm{bc}}}{p^{\mathrm{bc}}}$, plotted as a function of the right hand side, once again collapsing to the prediction; **(c)** The left hand side of Equation (6.29), $\frac{\Sigma^{\mathrm{s}}_{\mathrm{ij}}-\Sigma^{\mathrm{bc}}_{\mathrm{ij}}}{p^{\mathrm{bc}}}$, plotted as a function of the right hand side. All of the plots have been constructed using simulation data for each variable and no fitting parameters have been utilized.

range of packing fractions and restitution coefficients, and because the dynamics of granular materials are inherently disordered, it is necessary to measure many features of the spontaneously forming force networks in order to fully determine the stress tensor. This makes the constitutive relations look rather complex. Nevertheless, the agreement in Figure 6.8 establishes that it is the properties of the network, and not properties of the grains (such as density or restitution coefficient), that set the value of the stress tensor and collapse the data, taken over such a wide range of parameter space. Moreover the predictions of the Force-Network model do not just predict the scaling of the stress tensor, but actually predict its exact value.

Using the constitutive relations in Equations (6.27), (6.28) and (6.29), it is also possible to obtain simple scalings near critical points. For example, if we concentrate on the value of the stress tensor near the network transition at $\nu_{\rm bc}$, we see that $\Sigma^{\rm s}_{\alpha\beta} \propto z$. This is because, when $\xi/\xi_{\rm el} \approx 1$ near $\nu_{\rm bc}$, the deviation from the collisional stress is dominated by effects that only propagate over nearest neighbors. Therefore the number of contacts serves as the scaling variable. In contrast, near the jamming transition at $\nu_{\rm c}$, the networks are saturated and all of the collisional force from each contact is transferred to the network. In this case the stress tensor should depend on the size of the networks, and the constitutive relations indeed predict that $\Sigma^{\rm s}_{\alpha\beta} \propto \xi$. This scaling is especially interesting since

it suggests that the size of the networks is the important scaling variable, which might also control other features of the jamming transition. Indeed, once ξ becomes large, it is the clusters of grains, and not individual grains, that serve as the basic thermodynamic degrees of freedom.

It is important to remark here that the constitutive relations from the Force-Network model have been derived in the limit of perfectly rigid grains. In the case of a finite grain stiffness, there will be a finite contact time τ_c and a finite speed v_c. at which forces can propagate through the network. This will set a maximum correlation length $v_c\tau_c$, since information can only be transferred between a pair of grains if the network exists long enough to propagate it. This maximum correlation length will be a monotonically increasing function of the grain stiffness. If $v_c\tau_c > \xi$, then the stress tensor can be described by Equations (6.27), (6.28) and (6.29). However, if $v_c\tau_c < \xi$, it is necessary to replace the length-scale ξ with $v_c\tau_c$. Because ξ diverges as the material approaches the jamming limit and $v_c\tau_c$ is always finite we expect that, for a given grain stiffness, there will be a critical packing above which $v_c\tau_c < \xi$. This critical packing fraction will always be in the inertial regime, less than ν_c, and very close to jamming the elasticity of grains will begin to play an important role.

6.3 STZ Theory

The Shear Transformation Zone (STZ) Theory of amorphous solids was proposed in [127, 128, 129, 130, 131, 132] as a mean field model to account for the behavior of dense amorphous materials at low temperature. The theory is motivated by observations from simulations [133, 134, 135, 136] and experiments [137] which suggest that plastic deformation in amorphous materials results from non-affine rearrangements of small clusters of particles [138]. Additionally, Falk and Langer were able to show that there exist different types of zones which present a preferential response to different orientations of shear forces. They introduced the densities of these zones as state variables to characterize the internal structure of the molecular packing.

Central to the theory is the assumption that once an STZ undergoes an elementary rearrangement in a given direction it is unlikely that it can shear again in the same direction, although it can easily shear in the reverse direction. Zones are therefore two state systems, with the states corresponding to the zone orientation being aligned (denoted $-$) or anti-aligned (denoted $+$) with the shear stress. A rearrangement corresponds to a transition of a zone from a $\pm$-state into a $\mp$-state and vice-versa. The plastic shear rate is given by the rate at which STZs respond

to external stresses:

$$\dot{\gamma} \propto R_+ n_+ - R_- n_-, \tag{6.30}$$

where $R_\pm$ are the stress-dependent probabilities that zones of $\pm$ types are transformed into one another and $n_\pm$ is the total number of zones in either orientation.

In order to fully characterize the system, it is necessary postulate the dynamics of the state variables $n_\pm$. It has already been assumed that an STZ can change orientation, which is controlled by the rate factor $R_\pm$. However, it is also assumed that a zone can be created or destroyed by sufficiently "stirring" (or agitating) the system. These considerations set the dynamics of the state variables:

$$\frac{\partial n_\pm}{\partial t} = R_\mp n_\mp - R_\pm n_\pm + w(1 - \zeta n_\pm). \tag{6.31}$$

The first two terms correspond to the transformation of STZs between their two possible states. The last term accounts for the fact that STZs are renewed by the overall macroscopic deformation: it contains a creation and destruction rate, both proportional to the plastic work w of external forces per time unit.

6.3.1 Verification of the Microscopic Assumptions

Before applying STZ theory to granular materials, we check that the same qualitative observations as in [127] can be performed in these systems. Namely

that non-affine motion occurs in localized regions and that the positions of the localized regions depends sensitively on the orientation of the shear. The first observation motivates the choice of density of STZs as a state variable, and the second observation shows that each STZ has an orientation and therefore only responds to a certain orientation of shear stress.

These assumptions can be tested using a measure of the non-affinity of the deformation of a cluster of a few molecules or grains, first introduced by Falk and Langer in Ref. [127]. The grains undergoing non-affine rearrangement can be determined by first calculating, for each grain, the local strain rate at time $t - \Delta t$. Then, by measuring the difference D between the actual position at a later time t and the position predicted from the local strain rate at time $t - \Delta t$, we can determine which grains have moved non-affinely in the time period Δt. In practice, D is determined by minimizing

$$\tilde{D}^2(t, \Delta t) = \sum_i \sum_\alpha \Big(r_\alpha^i(t) - r_\alpha^0(t) - \sum_\beta (\delta_{\alpha\beta} + \dot{\gamma}_{\alpha\beta}) \times [r_\beta^i(t - \Delta t) - r_\beta^0(t - \Delta t)] \Big)^2 \tag{6.32}$$

with respect to the shear rate $\dot{\gamma}_{ij}$, where the subscripts α and β are spatial coordinates and the index i runs over all grains within two diameters of the reference grain, which labeled by the superscript $i = 0$. The minimum value of $\tilde{D}$, denoted

D, is an approximation of the local deviation from affine displacement for the reference grain in the time interval $[t - \Delta t, t]$. If there is no non-affine motion, then the motion of each individual grain should be completely determined by a local shear rate and $D = 0$. If there is non-affine motion then $D > 0$.

We have applied this test for non-affine motion to granular materials in simple shear to produce Figure 6.9. This figure is the counterpart of Figure 3 in [128] and Figure 7 in [127], which were created from simulations of an amorphous Lennard-Jones solid. Each picture has been created by shearing an identical initial arrangement of grains in a certain direction. D is the local measure of non-affinity obtained by comparison between the initial and final states. If D is larger than a reference value, the particle is said to have moved non-affinely and colored black.

In Figure 6.9 part (a) the system is sheared from strains of 0 to 0.05, and in (b) the system is sheared to from strains of 0.1 to 0.15. We notice that there is a tendency for the regions of non-affine displacement to form clusters, and the size of the resulting non-affine regions is about the same in both (a) and (b). In (c) the system is sheared from strains of 0 to 0.15 and now the size of the non-affine regions increases, suggesting many more fundamental rearrangements of STZs in the larger time period. In (d) the system is sheared from strains of 0 to -0.05 (in the *opposite* direction), starting from the same initial configuration as in (a). Once again we observe that the non-affine regions tend to form clusters. However, in

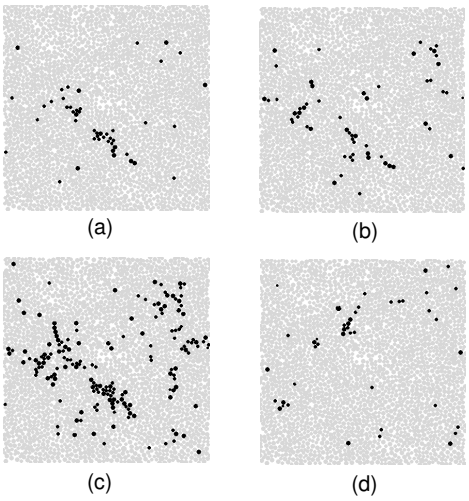

Figure 6.9: Screenshots of granular materials in steady state simple shear flow with grains undergoing non-affine displacement colored black. In (a) the system is sheared from 0 to 0.05, in (b) the system is sheared from .1 to .15, in (c) the system is sheared from 0 to .15, and in (d) the system is sheared in the opposite direction, from 0 to $-.05$.

comparing (a) and (d), we notice that the size of the non-affine regions is about the same in the two figures, but the locations are different. If the regions undergoing non-affine displacement did not have an orientation we would expect non-affine motion to occur in the same location, regardless of the orientation of the stress. However this is not the case and the data in Figure 6.9 suggests that the regions that move non-affinely have an orientation. This is qualitative evidence that the core assumptions of STZ theory are upheld in granular materials.

6.3.2 Quantitative Predictions

The STZ densities $n_\pm$ account for structural properties of a molecular or granular packing. They are thus expected to depend on the positions of grains, orientations and distribution of forces, orientations of velocities, but not on the overall amplitude of the forces or amplitude of velocities. For granular materials of perfectly rigid grains, the functions that determine $n_\pm$ are determined using the invariance in Newton's equations, as outlined in [57, 27].

Since w is equal to the plastic work done on the system per unit time it should be proportional to $s\dot{\gamma}$, where s is the shear stress and $\dot{\gamma}$ the shear rate. However, in order to make w invariant, we normalize by pressure so that $w = s\dot{\gamma}/p$. As for $R_\pm$, because of the invariance in Newton's equations we can separate the rate at which an STZ attempts to rearrange from the probability that an attempt leads to a successful rearrangement. The attempt rate must be proportional to $\sqrt{T}$ which sets the microscopic event rate and the probability to rearrange is written as an exponential activation factor of the invariant form $e^{\pm\kappa s/p}$. This yields $R_\pm \propto \sqrt{T}e^{\pm\kappa s/p}$.

Combining the expressions for $R_\pm$ and w with equations (6.30) and (6.31), while making a change of variables from $n_\pm$ to $\Delta \propto n_- - n_+$ and $\Lambda \propto n_- + n_+$,

yields the following STZ equations for granular materials:

$$\begin{aligned}
\dot{\gamma} &\propto \sqrt{T}\left(\Lambda \sinh\left(\kappa s/p\right) - \Delta \cosh\left(\kappa s/p\right)\right) \\
\dot{\Delta} &\propto \dot{\gamma}\left(1 - \zeta \frac{s}{p}\Delta\right) \\
\dot{\Lambda} &\propto \dot{\gamma}\frac{s}{p}(1-\Lambda).
\end{aligned} \tag{6.33}$$

Λ denotes the total density of zones and Δ measures the difference between the number of zones in each orientation and is therefore related to the anisotropy of the granular packing. κ and ζ are constants that do not depend on the macroscopic variables $\dot{\gamma}$, T, s, or p. However we would expect these constants to depend on properties of the grains such as shape, distributions of radii, restitution coefficients, friction coefficients, or other local static variables, including density.

The STZ equations determine the shear rate through the state variables Δ and Λ, which encode the microscopic structure of the material. They present two types of steady state solutions [127, 129, 57]: one branch of solutions represents a jammed state $\dot{\gamma} = 0$, and occurs when $\Delta/\Lambda = \tanh\left(\kappa s/p\right)$; the other branch of solution represents the steady flow and occurs when $\Lambda = 1$ and $\Delta = p/(\zeta s)$.

An elementary analysis of the phase diagram of this dynamical system indicates that the jammed state is stable if and only if

$$\zeta \frac{s}{p} \tanh\left(\kappa \frac{s}{p}\right) \leq 1 \tag{6.34}$$

and the flowing state is stable otherwise. The limit of stability occurs at a critical angle θ^*, which is the solution of

$$\zeta \tan\theta^* \tanh\left(\kappa \tan\theta^*\right) = 1. \tag{6.35}$$

θ^* is identified as the repose angle of the granular material, whose value is predicted by STZ theory.

In the steady flowing regime $\dot{\gamma} \geq 0$ and STZ theory yields the constitutive relation:

$$\frac{\dot{\gamma}\langle R\rangle}{\sqrt{T}} \propto \left(\sinh\left(\kappa s/p\right) - \frac{p}{s\zeta}\cosh\left(\kappa s/p\right)\right), \tag{6.36}$$

where we have inserted a factor of the average grain radius $\langle R\rangle$ to match units. In particular, in the limit when the ratio $\dot{\gamma}\langle R\rangle/\sqrt{T}$ vanishes, s/p converges towards $\tan\theta^*$. Therefore the STZ theory accommodates cases where the system jams and there is a residual pressure and shear stress at zero shear rate. In this case, STZ theory predicts that the shear stress will be proportional to the pressure.

6.3.3 Numerical Tests

Using the shear flows that we have simulated with the CD algorithm, we are able to test the flowing STZ constitutive relation in Equation (6.36). In Figure 6.10 we plot s/p as a function of $\langle R\rangle\dot{\gamma}/\sqrt{T}$ for large densities and many different restitution coefficients at zero friction in the simple shear flow geometry. The line is the STZ prediction, which fits the data very well.

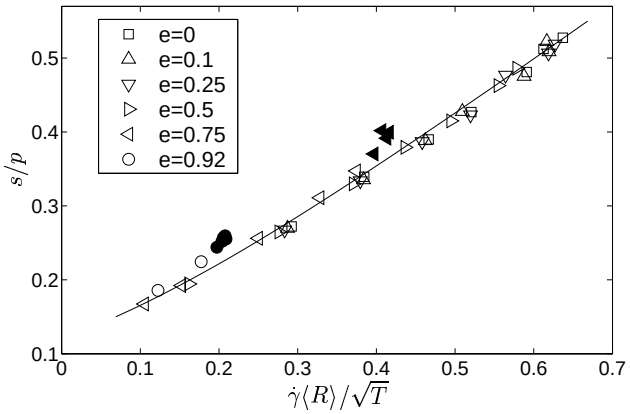

Figure 6.10: Data from simple shear simulations with different restitution, plotted along with the prediction from STZ theory, Equation (6.36). Filled data points correspond to granular flows in the dilute regime where $\xi/\xi_{\rm el} < 1.25$. The prediction matches the data for all values of restitution coefficient where the flow is in the dense regime, characterized by a large correlation length. STZ theory is not expected to hold in the dilute regime, since it assumes that the motion of nearby grains is correlated.

There are, however, many points (shaded) that do not match the STZ prediction– these are simply the points where $\xi/\xi_{\rm el} < 1.25$. Because these values of density and restitution coefficient produce flows that consist solely of binary collisions, we

would not expect STZ theory to hold since the correlated motion that it assumes is not present. The data in Figure 6.10 definitely supports the conclusion that STZ theory makes good predictions for granular flows in the dense regime where clusters of correlated grains exist.

In order to plot the STZ prediction, we determine the unknown coefficients in Equation (6.36) by fitting the simple shear data at $e = 0$. This is the first time in this manuscript that we have had to fit unknown coefficients, and it is important to show that the coefficients are related just to properties of the grains and are unrelated to the choice of shearing geometry. A simple test is to include the data from incline flow, which covers a different range of s/p and T to see if the results in Figure 6.10 can be extrapolated to different geometries.

In Figure 6.11 we plot data of s/p as a function of $\dot{\gamma}\langle R\rangle/\sqrt{T}$ for frictional ($\mu = 0.4$) and non-frictional ($\mu = 0$) granular materials with $e = 0$ in both simple shear flow and incline flow. In both cases, the line drawn through the data is a fit to Equation (6.36), with the unknown coefficients determined by fitting the simple shear data. We immediately notice that the coefficients depend on μ whereas Figure 6.10 shows that they do not depend on the restitution coefficient e.

From Figure 6.11 we conclude that the STZ constitutive equation is able to match the simple shear data by choosing appropriate fitting coefficients. We also

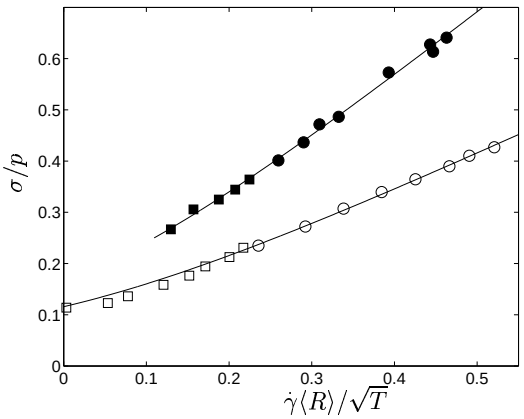

Figure 6.11: s/p plotted against $\dot{\gamma}\langle R\rangle/\sqrt{T}$ for frictional (filled symbols) and non-frictional (open symbols) granular materials. The circles correspond to data from simple shear flow and the squares to data from steady state incline flow. The line is a best fit to the steady state STZ prediction from Equation (6.36), where only the data from the simple shear flow geometry was used to construct the best fit. This shows that STZ theory properly predicts the outcome of incline flow experiments once the parameters (which depend only on grain properties) are determined from simple shear experiments.

find that the incline flow data is predicted using the exact same coefficients! This supports the conclusion that the unmeasurable parameters in Equation (6.36) do not depend on the shearing geometry and only depend on intrinsic properties of the material, such as polydispersity and roughness.

In summary, STZ theory predicts a constitutive relation for the shear stress based on assumptions about how non-affine motion occurs in the material. Using simulations of rigid granular materials we are able to validate the microscopic assumptions of the theory and show that the predicted constitutive relation makes accurate predictions and does not depend on the shearing geometry. Therefore, if the unknown coefficients are measured in one shearing geometry they can be used, along with Equation (6.36), to make predictions in different shearing geometries.

Chapter 7

Conclusions

In this dissertation we have explored properties of granular shear flows using molecular dynamics simulations. In addition to numerically obtaining constitutive relations of bulk granular dynamics, the simulations have been used as a tool to investigate how processes occurring on microscopic length-scales affect observables on macroscopic length-scales. The insight gained from these investigations has enabled an in-depth analysis of existing theories of granular flow and has inspired a new constitutive model based on force propagation through force chain networks.

From a physical point of view, the central result is the spontaneous emergence of long range correlations in granular shear flows as density is increased or restitution coefficient is decreased. The correlations arise due to the energy dissipation that occurs at contacts and imply that interactions between grains occur through force chain networks in dense regimes. In dilute regimes only binary collisions occur and correlations are not observed.

The observation of the network transition, which occurs at a well defined packing fraction $\nu_{\rm bc}$, raises a number of issues that deserve additional study. In particular, can the transition be viewed as a non-equilibrium phase transition? On the one hand, the transition is sharp, is associated with major changes in the nature of forces between grains, and is accompanied by a structural change in the material. On the other hand, the transition is different than typical phase transitions in that the structural change that occurs at $\nu_{\rm bc}$ is tied to dynamics and does not occur for zero shear rate. Nevertheless, a detailed study of how macroscopic properties scale with $(\nu - \nu_{\rm bc})$ close to $\nu_{\rm bc}$ would elucidate the properties of the transition, which could possibly be understood as the result of an exotic phase transition. The universality class of the transition might give further insight into the physics occurring close to $\nu_{\rm bc}$.

The network transition at $\nu_{\rm bc}$ is only one important transition as the packing fraction is increased. At $\nu_{\rm c} > \nu_{\rm bc}$ the system undergoes the jamming transition where the yield stress becomes non-zero. Although we have not carefully studied the properties of inertial flows close to $\nu_{\rm c}$, the models we have introduced in the dense regime make definite predictions about jamming. Both view jamming as a dynamic transition where either the size of correlated regions becomes too large for relaxation to take place or the shear transformation zones all become oriented in a fashion that does not allow motion.

An interesting property of the network and jamming transitions is that they are both linked to force chain networks in the material. While the network transition arises due to the emergence of force chains, the jamming transition occurs when the size of the force chains reaches the system size, or diverges in the thermodynamic limit. This suggests that studying the nature of force chains, which are one of the peculiarities of granular media, would lend insight to each of the important transitions that occur in granular flows.

This would be especially interesting in regards to the jamming transition. A great deal of research has been done on jamming, but it is always concentrated on granular systems with $\nu > \nu_c$. Studying the properties of the approach to jamming from the inertial side is advantageous because the system can always be forced into a steady state. Additionally, we have identified a diverging length scale that might provide insight to the transition.

From a more practical viewpoint, we have developed constitutive relations for granular flow that apply far from boundaries. However, we have concentrated on models of the stress tensor and many more constitutive relations remain to be discovered. There are still unknown parameters in the conservation equations, such as the heat flux and the energy dissipation, that need to be related to the hydrodynamic variables. Also, it is necessary to understand how boundary effects

can be incorporated in granular flows and what parameters set the boundary length-scales seen in incline flows.

Bibliography

[1] H. M. Jaeger and S. R. Nagel, "Physics of the granular state", Science **255**, 1523 (1992).

[2] A. Mehta and G. C. Barker, "The dynamics of sand", Rep. Prog. Phys. 383 (1994).

[3] H. M. Jaeger, S. R. Nagel, and R. P. Behringer, "Granular solids, liquids, and gases", Rev. Mod. Phys. **68**, 1259 (1996).

[4] P. G. de Gennes, "Granular matter: A tentative view", Physica A **261**, 267 (1998).

[5] E. Clement, "Rheology of granular media", Curr. Opin. Colloid Interface Sci. **4**, 294 (1999).

[6] L. P. Kadanoff, "Built upon sand: Theoretical ideas inspired by granular flows", Rev. Mod. Phys. **71**, 435 (1999).

[7] J. Rajchenbach, "Granular Flows", Adv. Phys. **49**, 229 (2000).

[8] V. V. Sokolovskii, *Statics of Granular Materials* (Pergamon, Oxford, 1965).

[9] A. N. Schofield and C. P. Roth, *Critical State Soil Mechanics* (McGraw Hill, 1968).

[10] J. Feda, *Mechanics of Particulate Materials: The Principles* (Elsevier, Amsterdam, 1982).

[11] R. M. Nedderman, *Statics and Kinematics of Granular Materials* (Cambridge University Press, Cambridge, 1992).

[12] A. Bose, *Advances in Particulate Materials* (Boston, Butterworth-Heinemann, 1995).

[13] *Granular Matter: An Interdisciplinary Approach*, ed. A. Mehta (Springer-Verlag, New York, 1993).

[14] *Disorder and Granular Media*, eds. D. Bideau and A. Hansen (Elsevier, Amsterdam, 1993).

[15] *Physics of Dry Granular Media* eds. H. J. Herrmann, J.-P. Hovi and S. Luding (Kluwer, Dordrecht, 1998).

[16] *Jamming and Rheology: Constrained Dynamics on Microscopic Scales*, eds. A. Liu and S. R. Nagel (Taylor and Francis, London, 2001).

[17] K. L. Johnson, *Contact Mechanics* (Cambridge University Press, Cambridge, 1987).

[18] P. Cundall and O. D. L. Strack, "A discrete numerical model for granular assemblies", Geotechnique **29**, 47 (1979).

[19] C. S. Campbell, "Granular shear flows at the elastic limit", J. Fluid. Mech. **465**, 261 (2002).

[20] E. Aharonov and D. Sparks, "Rigidity phase transition in granular packings", Phys. Rev. E **60**, 6890 (1999).

[21] C. O'Hern, L. E. Silbert, A. Liu, and S. R. Nagel, "Jamming at zero temperature and zero applied stress: The epitome of disorder", Phys. Rev. E **68**, 011306 (2003).

[22] H. P. Zhang and H. A. Makse, "Jamming transition in emulsions and granular materials", Phys. Rev. E **72**, 011301 (2005).

[23] R. P. Behringer, D. Howell, L. Kondic, S. Tennakoon, and C. Veje, "Predictability and granular materials", Physica D **133**, 1 (1999).

[24] D. M. Mueth, G. F. Debregeas, G. S. Karczmar, P. J. Eng, S. R. Nagel, and H. M. Jaeger, "Signatures of granular microstructure in dense shear flows", Nature **406**, 385 (2000).

[25] L. E. Silbert, D. Ertas, G. S. Grest, T. C. Halsey and D. Levine, "Granular flow down an inclined plane: Bagnold scaling and rheology", Phys. Rev. E **64**, 051302 (2001).

[26] F. da Cruz, S. Emam, M. Prochnow, J. -N. Roux, and F. Chevoir, "Rheophysics of dense granular materials: discrete simulation of plane shear flows", Phys. Rev. E **72**, 021309 (2005).

[27] G. Lois, A. Lemaître, and J. M. Carlson, "Numerical tests of constitutive laws for dense granular flows", Phys. Rev. E **72**, 051303 (2005).

[28] C. S. Campbell, "Rapid granular flows", Annu. Rev. Fluid Mech. **22**, 57 (1990).

[29] I. Goldhirsch, "Rapid granular flows", Annu. Rev. Fluid Mech. **35**, 267 (2003).

[30] E. Azanza, F. Chevoir and P. Moucheront, "Experimental study of collisional flows down an inclined plane", J. Fluid Mech. **400**, 199 (1999).

[31] D. Z. Zhang and R. M. Rauenzahn, "Stress relaxation in dense and slow granular flows", J. Rheol. **44**, 1019 (2000).

[32] H. H. Shen and B. Sankaran, "Internal length and time scales in a simple shear granular flow", Phys. Rev. E **70**, 051308 (2004).

[33] D. Z. Zhang, "Evolution of enduring contacts and stress relaxation in a dense granular medium", Phys. Rev. E **71**, 041303 (2005).

[34] A. Kudrolli, M. Wolpert, and J. P. Gollub, "Cluster formation due to collisions in granular materials", Phys. Rev. Lett. **78**, 1383 (1997).

[35] D. Bonamy, F. Daviaud, L. Laurent, M. Bonetti, and J. P. Bouchaud, "Multiscale clustering in granular surface flows", Phys. Rev. Lett. **89**, 034301 (2002).

[36] D. L. Blair and A. Kudrolli, "Clustering transitions in vibrofluidized magnetized granular materials", Phys. Rev. E **67**, 041301 (2003).

[37] P. Dantu, in *Proceedings of the 4th International Conference on Soil Mechanics and Foundations Engineering* (Butterworths Scientific Publications, London, 1957).

[38] F. Radjai, M. Jean, J. -J. Moreau, and S. Roux, "Force distributions in dense two-dimensional granular systems", Phys. Rev. Lett. **77**, 274 (1996).

[39] J. Geng, D. Howell, E. Loghi, R. P. Behringer, G. Reydellet, L. Vanel, E. Clemen t and S. Luding, "Footprints in sand: The response of a granular material to local perturbations", Phys. Rev. Lett. **87**, 035506 (2001).

[40] J. Geng, G. Reydellet, E. Clement and R. P. Behringer, "Green's function measurements of force transmission in 2D granuar materials", Physica D **182**, 274 (2003).

[41] T. S. Majmudar and R. P. Behringer, "Contact force measurements and stress-induced anisotropy in granular materials", Nature **435**, 1079 (2005)

[42] D. J. Evans and G. P. Morriss, *Statistical Mechanics of Nonequilibrium Liquids* (Academic Press, London, 1990).

[43] I. Goldhirsch and C. Goldenberg, "On the microscopic foundations of elasticity", Eur. Phys. J. E **9**, 245 (2002).

[44] I. Goldhirsch and C. Goldenberg, "Stress in dense granular materials", in *The Physics of Granular Media*, edited by H. Hinrichsen and D. E. Wolf (Wiley 2004)

[45] B. J. Glasser and I. Goldhirsch, "Scale dependence, correlations, and fluctuations of stresses in rapid granular flows", Phys. Fluid **13**, 407 (2001).

[46] K. M. Frye and C. Marone, "Effect of humidity on granular friction at room temperature", J. Geo. Res. **107**, B11 (2002).

[47] R. Brewster, G. S. Grest, J. W. Landry and A. J. Levine, "Plug flow and the breakdown of Bagnold scaling in cohesive granular flows", Phys. Rev. E **72**, 061301 (2005).

[48] H. Hertz, "On the contact of elastic bodies", J. Reine Angew. Math. **92**, 156 (1881).

[49] X. Jia, C. Caroli, and B. Velicky, "Ultrasound propagation in externally stressed granular media", Phys. Rev. Lett. **82**, 1863 (1999).

[50] C. S. Campbell and C. E. Brennen, "Computer Simulations of granular shear flows", J. Fluid. Mech. **151**, 167 (1985).

[51] H. J. Herrmann and S. Luding, "Modeling granular media on the computer", Cont. Mech. & Therm. **10**, 189 (1998).

[52] R. A. Bagnold, "Experiments on a gravity-free dispersion of large solid spheres in a Newtonian fluid under shear", Proc. Roy. Soc. London A **255**, 49 (1954).

[53] M. L. Hunt, R. Zenit, C. S. Campbell, and C. E. Brennen, "Revisiting the 1954 suspension experiments by R. A. Bagnold", J. Fluid. Mech. **452**, 1 (2002).

[54] F. Chevoir, M. Prochnow, J. T. Jenkins and P. Mills, "Dense granular flows down an inclined plane", in *Powders and grains 2001*, edited by Kishino (Swets and Zeitlinger, 2001).

[55] L. E. Silbert, J. W. Landry, and G. S. Grest, "Granular flow down a rough incline plane: Transition between thin and thick piles", Phys. Fluids **15**, 1.

[56] O. Pouliquen, "Scaling laws in granular flows down rough inclined planes", Phys. Fluids **11**, 542 (1999).

[57] A. Lemaître, "Origin of a repose angle: Kinetics of rearrangement for granular materials", Phys. Rev. Lett. **89**, 064303 (2002).

[58] GDR MIDI, "On dense granular flows", Eur. Phys. J. E **14**, 341 (2004).

[59] J. J. Moreau, "Unilateral contact and dry friction in finite freedom dynamics", in *Nonsmooth mechanics and application: courses and lectures*, edited by J. J. Moreau and P. D. Panagiotopoulos (Springer-Verlag, Vienna, 1988), pp. 1–82.

[60] M. Jean and J.-J. Moreau, "Unilaterity and dry friction in the dynamics of rigid body collections", in *Proceedings of Contact Mechanics International Symposium* (Presses Polytechniques et Universitaires Romandes, Switzerland, 1992), pp. 31–48.

[61] J. J. Moreau, "New computation methods in granular dynamics", in *Powders and Grains*, edited by C. Thornton (Brookfield, Rotterdam, Netherlands, 1993), pp. 227–232.

[62] J. J. Moreau, "Some numerical methods in multibody dynamics: application to granular materials", Eur. J. Mech. A-Solids **13**, 93 (1994);

[63] D. E. Wolf, "Modeling and Computer Simulation of Granular Media", in *Computational Physics*, edited by K. H. Hoffmann and M. Schreiber, Springer, Berlin, 1996

[64] M. Jean, "The non-smooth contact dynamics method", Comput. Methods Appl. Mech. Engrg. **177**, 235 (1999).

[65] S. F. Foerster, M. Y. Louge, H. Chang, and K. Allia, "Measurements of the collision properties of small spheres", Phys. Fluids **6** 1108 (1994).

[66] I. Goldhirsch and G. Zanetti, "Clustering instability in dissipative gases", Phys. Rev. Lett. **70**, 1619 (1993).

[67] S. McNamara and W. R. Young, "Dynamics of a freely evolving, two dimensional granular medium", Phys. Rev. E **53**, 5089 (1996).

[68] M. Alam and C. M. Hrenya, "Inelastic collapse in simple shear flow of a granular medium", Phys. Rev. E **63**, 061308 (2001).

[69] A. W. Lees and S. F. Edwards, "J. Phys. C: Solid State Phys. **5**, 1921 (1972).

[70] D. J. Evans and G. P. Morriss, "Nonlinear response theory for steady planar Couette flow", Phys. Rev. A **30**, 1528 (1984).

[71] M. Alam and S. Luding, "Rheology of bidisperse granular mixtures via event-driven simulations", J. Fluid. Mech. **476**, 69 (2003).

[72] P. -A. Lemieux and D. J. Durian, "From avalanches to fluid flow: A continuous picture of grain dynamics down a heap", Phys. Rev. Lett. **85**, 4273 (2000).

[73] O. Pouliquen and N. Renaut, "Onset of granular flows on an inclined rough surface: dilatancy effects", J. Phys. II **6**, 923 (1996).

[74] T. G. Drake, "Structural features in granular flows", J. Geophys. Res. **95**, 8681 (1990).

[75] D. M. Hanes and O. R. Walton, "Simulations and physical measurements of glass spheres flowing down a bumpy incline", Powder Tech. **109**, 133 (2000).

[76] P. Mills, D. Loggia, and M. Tixier, "Model for a stationary dense granular flow along an inclined wall", Europhysics Letters **45**, 733 (1999).

[77] P. Mills, M. Tixier, and D. Loggia, "Influence of roughness and dilatancy for dense granular flow along an inclined wall", Eur. Phys. J. E **1**, 5 (2000).

[78] G. Lois, A. Lemaître and J. M. Carlson, "The breakdown of kinetic theory in granular shear flows", preprint, cond-mat/0507286 (2005).

[79] G. Lois, A. Lemaître and J. M. Carlson, "Long range correlation in granular shear flow", in preparation.

[80] A. J. Liu and S. R. Nagel, "Jamming is not just cool anymore", Nature **396**, 21 (1998).

[81] C. Moukarzel, P. M. Duxbury, and P. L. Leath, "Infinite-cluster geometry in centra-force networks", Phys. Rev. Lett. **78**, 1480 (1997).

[82] C. Moukarzel and P. M. Duxbury, "Comparison of rigidity and connectivity percolation in two dimensions", Phys. Rev. E **59**, 2614 (1999).

[83] G. Lois, A. Lemaître and J. M. Carlson, "Momentum Transport in Granular Flows", preprint, cond-mat/0602277 (2006).

[84] C. Thornton and D. J. Barnes, "Computer simulated deformation of compact granular assemblies", Acta Mechanica **64**, 45 (1986).

[85] J. R. F. Arthur, J. A. Koenders, and R. K. S. Wong, "Anisotropy in particle contacts associated with shearing in granular media", Acta Mechanica **64**, 19 (1986).

[86] L. Rothenburg and R. J. Bathurst, "Analytical study of induced anisotropy in idealized granular materials", Geotechnique **39**, 601 (1989).

[87] F. Radjai, D. E. Wolf, M. Jean, and J.-J. Moreau, "Bimodal character of stress transmission in granular packings", Phys. Rev. Lett. **80**, 61 (1998).

[88] N. P. Kruyt, "Contact forces in anisotropic frictional granular materials", Int. J. of Sol. and Struct., **40**, 3537 (2003).

[89] H. Troadec, F. Radjai, S. Roux and J. C. Charmet, "Model for granular texture with steric exclusion", Phys. Rev. E **66**, 041305 (2002).

[90] C. Denniston and H. Li, "Dynamics and stress in gravity-driven granular flow", Phys. Rev. E **59**, 3289 (1999).

[91] A. Ferguson, B. Fisher, and B. Chakraborty, "Impulse distributions in dense granular flows: Signatures of large-scale spatial structures", Europhys. Lett. **66**, 277 (2004).

[92] J. W. Landry and G. S. Grest, "Jamming in granular hopper flow", preprint, cond-mat/0506110 (2005).

[93] E. Longhi, N. Easwar, and N. Menon, "Large force fluctuations in flowing granular medium", Phys. Rev. Lett. bf 89, 045501 (2002).

[94] C. S. O'Hern, S. A. Langer, A. J. Liu, and S. R. Nagel, "Force distributions near jamming and glass transitions", Phys. Rev. Lett. **86**, 111 (2001).

[95] L. E. Silbert, D. Ertas, G. S Grest, T. C. Halsey, and D. Levine, "Analogies between granular jamming and the liquid-glass transition", Phys. Rev. E **65**, 051307 (2002).

[96] F. Radjai, S. Roux, and J. -J. Moreau, "Contact forces in a granular packing", Chaos **9**, 544 (1999).

[97] D. M. Mueth, H. M. Jaeger and S. R. Nagel, "Force distribution in a granular medium", Phys. Rev. E **57**, 3164 (1998).

[98] G. Lovoll, K. J. Maloy, and E. G. Flekkoy, "Force measurements on static granular materials", Phys. Rev. E **60**, 5872 (1999).

[99] L. E. Silbert, G. S. Grest, and J. W. Landry, "Statistics of the contact network in frictional and frictionless granular packings", Phys. Rev. E **66**, 061303 (2002).

[100] J. W. Landry, G. S. Grest, L. E. Silbert, and S. J. Plimpton, "Confined granular packings: Structure, stress and forces", Phys. Rev. E **67**, 041303 (2003).

[101] S. Chapman and T. G. Cowling, *The Mathematical theory of non-uniform gases* (Cambridge, 1970).

[102] J. H. Ferziger and H. G. Kaper, *Mathematical theory of transport processes in gases* (Elsevier, New York 1972).

[103] V. Garzo and J. W. Dufty, "Dense fluid transport for inelastic hard spheres", Phys. Rev. E **59**, 5895 (1999).

[104] J. F. Lutsko, "Rheology of dense polydisperse granular fluids under shear", Phys. Rev. E **70**, 061101 (2004).

[105] J. F. Lutsko, "Transport properties of dense dissipative hard-sphere fluids for arbitrary energy loss models", Phys. Rev. E **72**, 021306 (2005).

[106] C. K. K. Lun, S. B. Savage, D. J. Jeffrey and N. Chepurniy, J. Fluid Mech. **140**, 223 (1984).

[107] J. T. Jenkins and M. W. Richman, "Kinetic theory for plane flows of a dense gas of identical, rough, inelastic, circular disks", Phys. Fluids **28**, 3485 (1985).

[108] T. P. C. van Noije and M. H. Ernst, "Kinetic theory of granular gases", in *Lecture Notes in Physics* **564**, edited by T. Poschel and S. Luding (Springer-Verlag 2001).

[109] N. V. Brilliantov and T. Poschel, *Kinetic Theory of Granular Gases* (Oxford University Press, 2004).

[110] J. J. Brey, J. W. Dufty, and A. Santos, "Dissipative dynamics for hard spheres", J. Stat. Phys. **87**, 1051 (1997).

[111] S. Luding and A. Santos, "Molecular dynamics and theory for the contact values of the radial distribution functions of hard-disk fluid mixtures", J. Chem. Phys. **121**, 8458 (2004).

[112] S. J. Moon, M. D. Shattuck, J. B. Swift, "Velocity distributions and correlations in homogeneously heated granular media", Phys. Rev. E **64**, 031303 (2001).

[113] T. P. C. van Noije and M. H. Ernst, "Ring kinetic theory for an idealized granular gas", cond-mat/9706020 (1997).

[114] T. P. C. van Noije, M. H. Ernst, R. Brito, and J. A. G. Orza, "Mesoscopic theory of granular fluids", Phys. Rev. Lett. **79**, 411 (1997).

[115] D. L. Blair and A. Kudrolli, "Velocity correlations in dense granular gases", Phys. Rev. E **64**, 050301(R) (2001).

[116] A. Prevost, D. A. Egolf, and J. S. Urbach, "Forcing and velocity correlations in a vibrated granular monolayer", Phys. Rev. Lett. **89**, 084301 (2002).

[117] O. Pouliquen, "Velocity correlations in dense granular flows", Phys. Rev. Lett. **93**, 248001 (2004).

[118] S. N. Coppersmith, C. -h. Liu, S. Majumdar, O. Narayan, and T. A. Witten, "Model for force fluctuations in bead packs", Phys. Rev. E **53**, 4673 (1996).

[119] J. E. S. Socolar, "Average stresses and force fluctuations in noncohesive granular materials", Phys. Rev. E **57**, 3204 (1998).

[120] P. Claudin, J.-P. Bouchaud, M. E. Cates, and J. P. Wittmer, "Models of stress fluctuations in granular media", Phys. Rev. E **57**, 4441 (1998).

[121] M. Nicodemi, "Force correlations and arch formation in granular assemblies", Phys. Rev. Lett. **80**, 1340 (1998).

[122] J. E. S. Socolar, D. G. Schaeffer, and P. Claudin, "Directed force chain networks and stress response in static granular materials", Eur. Phys. J. E **7**, 353 (2002).

[123] M. Otto, J.-P. Bouchaud, P. Claudin, and J. E. S. Socolar, "Anisotropy in granular media: Classical elasticity and directed-force chain network", Phys. Rev. E **67**, 031302 (2003).

[124] J.-P. Bouchaud, P. Claudin, D. Levine and M. Otto, "Force chain splitting in granular materials: A mechanism for large-scale pseudo-elastic behavior", Eur. Phys. J. E **4**, 451 (2001).

[125] C. F. Moukarzel, "Isostatic phase transition and instability in stiff granular materials", Phys. Rev. Lett. **81**, 1634 (1998).

[126] J.-N. Roux, "Geometric origin of mechanical properties of granular materials", Phys. Rev. E **61**, 6802 (2000).

[127] M. L. Falk and J. S. Langer, "Dynamics of viscoplastic deformation in amorphous solids", Phys. Rev. E **57**, 7192 (1998).

[128] M. L. Falk, "Molecular-dynamics study of ductile and brittle fracture in model noncrystalline solids", Phys. Rev. B **60**, 7062 (1999).

[129] M. L. Falk and J. S. Langer, "From simulation to theory in the physics of deformation and fracture", M.R.S. Bulletin **25**, 40 (2000).

[130] J. S. Langer, "Microstructural shear localization in plastic deformation of amorphous solids", Phys. Rev. E **64**, 011504 (2001).

[131] J. S. Langer and L. Pechenik, "Dynamics of shear-transformation zones in amorphous plasticity: Energetic constraints in a minimal theory", Phys. Rev. E **68**, 061507 (2003).

[132] M. L. Falk, J. S. Langer, and L. Pechenik, "Thermal effects in the shear-transformation zone theory of amorphous plasticity: Comparisons to metallic glass data", Phys. Rev. E **70**, 011507 (2004).

[133] S. Kobayashi, K. Maeda and S. Takeuchi, "Computer simulation of deformation of Amorphous Cu 57 Zr 43", Acta Met **28**, 1641 (1980).

[134] D. Srolovitz, K. Maeda, V. Vitek and T. Egami, "Structural defects in amorphous solids: Statistical analysis of a computer model", Phil. Mag. A **44**, 847 (1981).

[135] S. Takeuchi and K. Maeda, "Microscopic mechanism of plastic deformation in metallic glasses", Key Eng. Mater. **13-15**, 749 (1987).

[136] D. Deng, A. S. Argon, and S. Yip, "Simulation of plastic deformation in a two-dimensional atomic glass by molecular dynamics" Philos. Trans. R. Soc. Lond. A **329**, 613 (1989).

[137] A. Argon and H. Kuo, "Plastic flow in a disordered bubble raft", Mater. Sci. Eng. **39**, 101 (1979).

[138] A. Argon and L. Shi, "Development of viscoplastic deformation in metallic glasses", Acta Metall. **31**, 499 (1983).

[139] M. P. Allen and D. J. Tildesley, *Computer Simulations of Liquids* (Oxford: Clarendon, 1987).

Appendix A

Details of the simulation method

In this appendix the algorithmic techniques underlying the Contact Dynamics simulations of granular flow are reviewed in detail. A concise overview of the algorithm is included in Chapter 4. Here we focus on technical issues.

A.1 Determining contact forces using Contact Dynamics

The challenge of simulating granular media is to numerically integrate Newton's equation of motion for a collection of N grains that only interact upon contact and dissipate energy. To carry out this integration, the algorithm must provide the values of the forces between all contacting pairs of grains. The Contact Dynamics algorithm determines contact forces based on constraints associated with perfectly rigid grains [59, 60, 61, 62, 64]. This is an idealization of realistic

granular media that always have a finite Young's modulus. However, as we have argued, many properties of granular flows can be explored in the limit of infinite stiffness.

The central constraint relevant to rigid grains is that they do not deform. Therefore, once a pair of grains comes into contact, a repulsive force must be immediately created to prevent deformation and alter the relative velocity of the contacting pair. It is also necessary that the relative velocity decrease so that energy is dissipated.

The Contact Dynamics algorithm determines the numerical value of the contact force by assuming that the relative velocities are updated using a constant coefficient of restitution e. A pair of grains is defined by the positions $\{\mathbf{r}^I, \mathbf{r}^J\}$ and velocities $\{\mathbf{v}^I, \mathbf{v}^J\}$ of each grain, which are functions of time. A contact is formed when the distance between grains $|\mathbf{r}^I - \mathbf{r}^J|$ is less than or equal to the sum of the grain radii. Given a pair of contacting grains, we define the unit normal $\hat{\sigma}^{IJ} = (\mathbf{r}^I - \mathbf{r}^J)/|\mathbf{r}^I - \mathbf{r}^J|$ and the relative velocity $\mathbf{V}^{IJ} = \mathbf{v}^I - \mathbf{v}^J$. The constraint of constant restitution mandates that a contact at time t is updated to time $t + dt$ so that

$$\hat{\sigma}^{IJ}(t + dt) \cdot \mathbf{V}^{IJ}(t + dt) = -e\hat{\sigma}^{IJ}(t) \cdot \mathbf{V}^{IJ}(t) \tag{A.1}$$

and

$$\hat{\sigma}^{IJ}(t+dt) = \hat{\sigma}^{IJ}(t). \tag{A.2}$$

These equations guarantee that after the interaction, the pair of grains is no longer moving together and that energy is dissipated locally.

In addition to the constraint of restitution, it is necessary that the velocities of each grain are updated according to Newton's equations. This ensures that

$$\mathbf{v}^I(t+dt) = \mathbf{v}^I(t) + \frac{1}{m^I}\frac{\mathbf{F}^I J(t)}{dt} \tag{A.3}$$

and

$$\mathbf{v}^J(t+dt) = \mathbf{v}^J(t) - \frac{1}{m^J}\frac{\mathbf{F}^I J(t)}{dt}, \tag{A.4}$$

where m^I is the mass of grain I and $\mathbf{F}^{IJ}(t)$ is the contact force between grains I and J at time t. These are simply the equations inferred from momentum conservation.

Using the preceding equations, the normal component of the contact forces can be deduced. This "inverse problem" of solving for the forces, given the constraints on velocities, is the central characteristic of Contact Dynamics simulations. It is easy to appreciate how this is carried out by using the simple example of an isolated contact between two grains. In this case, Equations (A.1) through (A.4)

can be combined and the force at time t can be analytically solved as

$$\hat{\sigma}^{IJ}(t) \cdot \mathbf{F}^{IJ}(t) = (1+e)\frac{m^I m^J}{m^I + m^J}\hat{\sigma}^{IJ}(t) \cdot \mathbf{V}^{IJ}(t). \tag{A.5}$$

We see from this equation that the normal component of the force at time t is determined uniquely by properties of the grains (mass and restitution) and the relative velocities of the grains at time t. We arrived at this equation by combining one "constraint" equation (Equation A.1) with two "conservation" equations (Equations A.3 and A.4).

The inverse problem of contact dynamics is trivial for interactions between two grains, but becomes more difficult as a larger number of contacts are considered. In particular, because the Contact Dynamics algorithm uses a fixed time step, a grain can have more than one contact in each time step. Therefore, each grain may have multiple constraint equations. For a large cluster of contacting grains, the constraint equations will be highly coupled. The essential feature of the Contact Dynamics algorithm is an efficient method to solve the constraint equations, coupled with the conservation equations.

To solve the inverse problem efficiently, it is useful to define the "formal normal velocities"

$$U^{IJ}_{\text{norfor}}(t) = \hat{\sigma}^{IJ}(t+dt) \cdot \mathbf{V_F}^{IJ}(t+dt) + e\hat{\sigma}^{IJ} \cdot \mathbf{V}^{IJ}(t) \tag{A.6}$$

for each pair of contacting grains. In this equation there appears the relative velocity $\mathbf{V_F}$. This is the relative velocity that is expected in the next time step, given the current value of the contact force. The important realization is that, in order for restitution as in Equation (A.1) to hold, the formal velocities of each pair of grains must equal zero for the appropriately chosen contact force.

Contact Dynamics solves the inverse problem using an inductive process. Given a small positive number Υ, the series of steps is as follows:

1. Guess an initial set of "trial" forces on each contact. For example, set them all to zero.

2. For each contact, calculate U^{IJ}_{norfor} using these trial forces.

3. - If $-\Upsilon < U^{IJ}_{\text{norfor}} < \Upsilon$, do nothing.
   - If $U^{IJ}_{\text{norfor}} \geq \Upsilon$, then decrease $\hat{\sigma}^{IJ}(t) \cdot \mathbf{F}^{IJ}(t)$ by an amount proportional to $|U^{IJ}_{\text{norfor}}|$. If this results in $\hat{\sigma}^{IJ}(t) \cdot \mathbf{F}^{IJ}(t) < 0$, then set the force to zero.

- If $U^{IJ}_{\text{norfor}} \leq -\Upsilon$, then increase $\hat{\sigma}^{IJ}(t) \cdot \mathbf{F}^{IJ}(t)$ by an amount proportional to $|U^{IJ}_{\text{norfor}}|$.

This series of steps is carried on until $|U^{IJ}_{\text{norfor}}| < \Upsilon$ for all contacts that have formed. This ensures that the restitution constraint is upheld on all contacts, within an accuracy given by Υ. The value of Υ is an algorithmic parameter that, like the time step dt, must be taken small enough so that no macroscopic variables depend on its value.

There is an important relationship between the value of Υ and dt. Because the Contact Dynamics algorithm simulates perfectly rigid grains, there should be no independent time-scale introduced by the interactions between grains. However, if Υ is constant, then it sets a maximum *velocity* which introduces a non-trivial time scale into the dynamics. Therefore, in order for the algorithm to obey a strict time scaling, $\Upsilon \propto dt^{-1}$. This sets a maximum *penetration* between grains and the interaction remains time-invariant. In the simulations we have performed, it has proven adequate to use $\Upsilon = 10^{-10}/dt$.

The process outlined above solves the inverse problem of finding forces based on the behavior of velocities. However, only the normal coefficient of the contact forces has been discussed. For frictionless granular media, this is the only component that is non-zero. If friction is introduced between grains then there will also

be a tangential force so that $\hat{\sigma}^{IJ}(t) \times \mathbf{F}^{IJ}(t) \neq 0$. This tangential force will affect both the translational velocities and the rotations of the contacting grains.

To include tangential forces, a second inverse problem is solved. Once again there is a coefficient of restitution in the tangential direction e_t that relates the relative tangential velocities after the interaction with the relative tangential velocities before the interaction (see Equation 4.1). When considering the tangential relative velocities, both the translational and rotational parts must be included to obtain the true tangential velocity at the contact point. A tangential formal velocity is then constructed and the tangential forces are determined using the same process as the normal forces. There is one added constraint that upholds Coulomb friction between grains with coefficient μ:

$$|\hat{\sigma}^{IJ}(t) \times \mathbf{F}^{IJ}(t)| \leq \mu |\hat{\sigma}^{IJ}(t) \cdot \mathbf{F}^{IJ}(t)|. \tag{A.7}$$

This constrains the tangential force to be less than or equal to μ times the normal force. If the magnitude of the tangential force becomes larger than μ times the normal force at any stage in the iteration to determine contact forces, then the tangential force is reduced to equal exactly μ times the normal force. In this way, friction is accounted for and the tangential forces can be determined after the normal forces are known.

A.2 Time-stepping algorithm

In the previous section we discussed how the Contact Dynamics algorithm determines the contact forces between grains by solving an inverse problem based on the kinematic constraints of restitution, combined with Coulomb friction. In order to integrate Newton's equations, these forces are then incorporated into a time-stepping algorithm. We utilize the leap-frog Verlet algorithm [139]. The schematic of the algorithm is as follows:

1. Choose a time step dt.

2. Use the current velocities $\mathbf{v}^I(t)$ and angular velocities $\omega^I(t)$ to determine the updated positions $\mathbf{r}^I(t+dt)$ and angular orientations $\theta^I(t+dt)$ of every grain.

3. If there are external forces, update the velocities accordingly.

4. Given the new positions, find all pairs of contacting grains.

5. Use the Contact Dynamics algorithm introduced in the previous section to calculate contact forces $\mathbf{F}^{IJ}(t)$.

6. Use these contact forces to update the velocities $\mathbf{v}^I(t+dt)$ and angular velocities $\omega^I(t+dt)$.

7. Use the new velocities $\mathbf{v}^I(t+dt)$ and angular velocities $\omega^I(t+dt)$ to determine the updated positions $\mathbf{r}^I(t+2dt)$ and rotations $\theta^I(t+2dt)$ of every grain.

This list enumerates the necessary ingredients to make a single step of size $2dt$ in the Verlet algorithm. It has the common "leapfrog" characteristic of such algorithms, utilizing Contact Dynamics to solve for the contact forces at the intermediate step.

A.3 Forming initial configurations

In order to carry out the simulations, it is necessary to create an initial configuration of grains. In the case of flow down an incline, the grains start in a very dilute packing and are allowed to collapse under gravity onto a plane consisting of grains that are fixed. In this way, the packings create themselves.

For shear flows in the Lees-Edwards simple shearing geometry, however, it is more difficult to create initial configurations. The configurations must have a constant packing fraction with periodic boundary conditions. To create these packings, we begin with a dilute collection of grains and slowly increase each grain diameter by the same percentage until the desired packing fraction is reached. While the diameters are growing, we also update the positions using molecular dynamics simulations with repulsive forces proportional to the overlap between

pairs of grains. This eliminates overlaps and creates dense packings. Care must be taken when choosing the initial diameters of the grains and the growth rate so that the final diameters adhere to the proper distribution.